EMERGENT NONEQUILIBRIUM STATISTICAL MECHANICS FROM DEATH AND BIRTH IN BIOFILMS

A Dissertation
Presented to
The Academic Faculty

by

Arben L. Kalziqi

In Partial Fulfillment
of the Requirements for the Degree
of Doctor of Philosophy in the
School of Physics

Georgia Institute of Technology
December 2019

EMERGENT NONEQUILIBRIUM STATISTICAL MECHANICS FROM DEATH AND BIRTH IN BIOFILMS

Approved by:

Dr. Peter J. Yunker, Advisor
School of Physics
Georgia Institute of Technology

Dr. Simon Sponberg
School of Physics
Georgia Institute of Technology

Dr. Brian K. Hammer
School of Biological Sciences
Georgia Institute of Technology

Dr. Harold Kim
School of Physics
Georgia Institute of Technology

Dr. D. Zeb Rocklin
School of Physics
Georgia Institute of Technology

Date Approved: May 16, 2019

DEDICATION

To my family—blood and chosen.

ACKNOWLEDGEMENTS

We do not exist as individuals. While this thesis has taken me about six years to put together, the amount of time that has been invested into me by those who cared is nigh uncountable: it's all I can do to pay it forward.

I'll start with my parents, Donna and Agim, who worked so hard—harder than anyone should have to—to make sure that their children had access to the opportunities that they had lacked. I feel enormous and eternal gratitude for their love, support, and encouragement, and am glad that time and hardship have only brought us closer together. I could not be more privileged. I would be remiss not to thank my sister, as well: I'm happy that our relationship is loving and amicable now, as compared to our childhood (but I guess that's pretty typical!), and it brings me joy to know that you're doing work that is both important to you, and just important in general. May we all be so blessed.

My advisor, Peter Yunker, has been the kindest, most helpful advisor and mentor that I could have asked for. Especially given the circumstances of my initial joining of his nascent lab, I doubt I could have been more lucky. He's helped me to significantly hone my communication skills, to take jumps I was at first afraid to take, and has been an ideal model of what a scientist and mentor should be. It also must be noted: the specificity with which he can offer help to every student in the lab on their individual projects and presentations is *staggering*; it's genuinely inspiring to see how much care he puts into all of his students. I'm a better scientist and a better story-teller for the time I've spent in his lab.

Speaking of the lab: I can't begin to say enough about everybody, but it was a pleasure. I give my thanks in particular to Shane, who told me at the *Wrecking Bar* that he had just joined the lab of this new hire, one "Peter Yunker", and that it seemed like I might be a good fit if I were still looking for an advisor. As demonstrated by his graduating the lab first, Shane was a paragon of hard, efficient work, and always had an incisive take to boot. Jonathan has always been there to provide two sides of a dry coin: dry, rigorous physics with a depth and breadth of knowledge which would be hard to match across the School, and dry humor to cut through the tension of the grad student experience when it was least expected and most needed. It pains me to admit it, but I doubt that I'll ever meet a better punster. I wish David the best of luck with his upcoming internship, the rest of his degree, and with his family—though I'm sure that he won't need much luck at all. David was an excellent comrade to have at my back (literally—he sat right behind me), and a great collaborator/simulations wizard to boot. It was a pleasure to see you start a family, and to meet them. I haven't known Tom for quite as long, but he's such a good-natured and amicable person that the lab is definitely brighter for his joining it. I imagine that his indomitable work ethic and deep desire to explore his experimental systems will take him as far as he wants to go. Ali was another bright spot, I'll always enjoy the memory of his and Peter's "disagreements" about superflake interlocking, as well as my getting to frequently hear a word as ridiculous as "superflakes" at all. (Also, he makes a mean lunch.) Skanda has always asked unexpected questions, which have been great to get me to think outside of whatever box I was in at the moment. I wish him all the best with his family, as well—and he may actually need the luck, as Chao just had twins! I'd like to thank Gabi for being an unbelievably industrious worker and presenter, as well as a witch at the

microscope: she has very literally elucidated innumerable things for us and our collaborators. I hope that Atlanta continues to get more bike-friendly while she's here. Lastly, I'd like to thank Tanay for always having an interesting *Mathematica* problem for me to solve; it's great to feel useful, and occasionally necessary to feel distracted.

None of this thesis—and I mean *none*—would have been possible without the help of our collaborators in the Hammer lab. Brian, Michael, Cristian, Holly, Sophia, Eryn, and Thomas are heroes, and I will not hear otherwise. In particular, I'd like to thank Brian for explaining the entirety of biology to our group, and doing it with such a warm, avuncular tone. Michael has always been ready at a moment's notice to work on a new strain, or to grow one out of the ether (or, in this case, the -80 freezer), and I can't thank him enough. I'll miss our *vibrio* meetings more than most meetings have a right to be missed.

I'd like to give a brief thanks to the undergraduate students of SPS, who were always there to blow off steam with and have great political conversations with. Particularly, I'd like to thank Sam, Grace, Nathan, Mathilda, Charles, Viv, Hunter, Conner, Sumter, Thomas, Patrick, Doug, Sarah, C.J., Will, Martino, Lin, and Gwen. I'm sure I'm missing a few, but it speaks to the quality of the organization that there are so many great people that I'm worried I've forgotten some. This group single-handedly raises the average student quality of Georgia Tech by a significant level ($p < .001$).

I wouldn't be where I am without my friends in the Barbell Club or Citadel Nutrition, either. My infinite thanks lie with Dan for providing a space for all of us to improve ourselves, physically and more, and with Obi for reviving the club after a long slumber. Michael, Reyna, Noah, Stef, Thomas, Jose, Arthi, Fed, Sara, and Sree are all

incredible people that anybody would be lucky to know for a short time—and I, all the more, since I've had them in my life for so long. Here's to getting stronger still.

Finally, I need to thank my two closest confidantes. First, Natalie: a caring, brilliant, incredible person who deserves the world and has been there to listen to me for years and years, and who's never afraid to provide a reality check—whether critical or supportive, it's always helpful. Keep on bee-ing you! Last, I absolutely must thank my fluffy black old cat, Boo. She's always there to cuddle up or just keep company, and always seem to know which one is right (except for when she wants breakfast). A lot of nights would have been harder without her adorable little purrs.

SUMMARY

This thesis experimentally explores the statistical mechanics which emerge in the study of bacterial biofilms, highly nonequilibrium communities in which a vast number of bacteria make their homes, and which are of tremendous importance in ecology, medicine, and the economy.

In the first set of experiments, we found that local, contact-based killing between cells results. We inoculated multiple, well-mixed strains of *V. cholerae* on agar pads, then incubated them for 24 hours. When we chose a strain pairing where cells could not kill each other, we found that the strains remained well-mixed regardless of temperature. However, when we mixed together two strains which could kill each other on contact via the Type VI Secretion System ("T6SS"), we found that they underwent an order-disorder transition reminiscent to that seen in the Ising model of an electron spin lattice, with higher temperatures corresponding to later timepoints in this transition. Because spatial assortment is a common means by which bacteria solve public goods dilemmas, we hypothesized that bacteria which could kill non-kin might be more cooperate with their kin. Though a phylogenetic analysis, we found that the number of different T6SS toxins strongly correlated with the number of genes dedicated to the production of external goods, a proxy for cooperativity. Thus, intercellular killing leads to Model A coarsening and (possibly) to the evolution of cooperation.

In the next set of experiments, we used genetically modified strains of *V. cholerae* which secreted no exopolysaccharides ("EPSes"), and thus formed tissue-like ("Matrix-") biofilms resembling simple stacks of cells. We inoculated biofilms with "nonkiller" or

"mutual killer" pairings, and used a white-light interferometer to measure their surface topographies with ~nanometer precision. Surprisingly, we found that surface of biofilms with killing were significantly rougher than those without. A 2015 paper by *Risler, Peilloux, and Prost* suggested that in the homeostatic limit, the surface fluctuation spectra of a tissue surface may resemble those of a thermal permeable membrane, with an activity-mediated effective temperature. Our biofilm measurements served as experimental support for this theory, and provide further evidence of an effective fluctuation-response relationship driven by birth and death which may exist in cellular solids. Further, we performed minimal simulations which both recapitulated the aforementioned topographical difference and suggested the killing serves to fluidize biofilms.

The final set of experiments served as a theoretical and experimental expansion of the previous set. We grew biofilms that could produce EPSes ("Matrix+"), and were thus less tissue-like and more similar to the typical biofilms which are found in nature. We tested the mechanical properties of Matrix- and Matrix+ biofilms, and found that the latter had a higher viscosity by a factor of roughly three. Next, we measured surface topographies and found that while the topographies of Matrix- and Matrix+ biofilms looked similar, Matrix+ biofilms had an effective temperature that was roughly three times higher. To probe whether the effective temperature derived in the second set of experiments had a kinetic interpretation, we used the generalized Stokes-Einstein relation to convert extracted effective temperatures into effective diffusivities, and found that cellular diffusion inside Matrix- and Matrix+ biofilms occurred at the same (viscosity-independent) rate. Simulations, analytical results, and experimental PIV all agree with this result, lending yet more credence to the effective fluctuation-response relationship suggested by *Risler et al.*

TABLE OF CONTENTS

LIST OF FIGURES

CHAPTER 1. INTRODUCTION

Every physics student takes at least one statistical mechanics course, and afterward wonders why they had to learn classical thermodynamics at all. In the beginning of such courses, students are told that the relationships being derived and discussed hold true for *equilibrium* systems. As the course goes on, however, this warning is often left by the wayside; students are not necessarily encouraged to keep this rather strict condition on their minds. Importantly, this often stops them from asking why they're studying the subject in the first place—after all, how many systems in the real world actually fit this strict definition of equilibrium? The planet doesn't, or we wouldn't have different seasons, let alone be at all concerned about climate change. We as humans certainly don't, or we wouldn't need to eat or exercise. Even tiny bacteria that surround us in their innumerable trillions are not in equilibrium and ostensibly cannot be analyzed using the tools learned in these courses—so why learn them at all?

A physicist's favorite word saves us from having wasted our time learning the subject: "effective". Even though precious few real systems can be directly analyzed with the toolset of equilibrium statistical mechanics, many non-equilibrium systems *effectively* follow some modified form of the rules and relationships described thereby. Therefore, the world is rich with untapped opportunities to apply these tools to systems that we might have previously thought physically insoluble.

The nascent subfield of "physics of living systems" (under the more general umbrella of "quantitative biosciences") is currently exploding in interest and results. One such "living system" is the biofilm, a form of life in which a considerable fraction of the world's

bacterial population makes their home [1]. Biofilms are soft solids comprising collections of cells including (but not limited to) fungal, bacterial, and/or algal cells [2], [3]. These structures are three-dimensional and syntrophic, and can contain cells of different phenotypes, species, and even genera, as well as extracellular products secreted by the cells [4]–[6]. Because many cells live together in any given biofilm, eating from the same nutrient source, sharing secreted goods, and enjoying physical and chemical protection from predation, sanitation, and more, they are often called "cities of microbes" [1], [7]–[12]. Given these details, it goes without saying that biofilms are not only non-equilibrium systems, but exist far from equilibrium—thus, the aforementioned non-equilibrium statistical mechanics may be a novel tool for studying these microbial cities [13]–[19].

Biofilms are not as niche as they might first sound to the interested layperson or even interested physicist: nearly every microorganism can form biofilms, and biofilms can form on nearly every surface, from hospital bed railings [20] to crab shells [21] to water pipes [22], [23] to human lungs [20], [24]–[27]. While certainly a boon to microbes, they are responsible for many serious economic and health concerns, so using every tool available to understand their formation, activity, and persistence is of significant societal importance. From a more insular perspective, the ubiquity of biofilms implies a remarkable diversity of physical properties and processes: cells in biofilms may have different shapes and sizes, interact with each other via an assortment of biophysical and biochemical mechanisms, generate significant structural differences at various size scales, and secrete extracellular matrix-forming products. Mechanically, each of these cell-level differences can yield a range of elastic moduli, viscosities, membrane tensions, and more in the resultant biofilms [10], [28].

The sheer number of variables might be daunting to a physicist. However, as the genetic manipulation of many species is quite advanced, the creation of "model" biofilms designed to study a specific interaction is both possible and achievable on very reasonable timescales [29]–[31]. This, then, seems a rare confluence in the scientific world: there are many interesting systems to study, there exist novel methods for studying them via experiments which are newly achievable, *and* the study of these systems is of importance to society at large.

While at Georgia Tech, I have been lucky to be part of this rare confluence, and have worked on several fascinating studies of biofilm mechanics. Those works include a study of the physics of inter-strain coarsening in *V. cholerae* biofilms and its evolutionary consequences [32]; an investigation [33] of a predicted effective fluctuation-response relationship in tissues [13] using model biofilms as an experimental system, wherein activity is mediated by reproduction and death rather than thermal fluctuations; and prediction and measurement of viscosity-independent cellular diffusion inside biofilms driven by cellular division and death [34]. Underlying the latter two of these works is a novel measurement technique previously unused in the study of biofilms, which presents opportunities for more general phenotypic analysis. What follows is a short overview of each of these works, which are the subject of this thesis.

1.1 Model A coarsening of mutually-killing bacterial strains

If you were to ask almost any scientist, "What does a lattice of random-spin electrons have to do with two strains of *V. cholerae* fighting each other to the death?", some might

answer by asking what inspired such a ridiculous question. But, how could they explain this?

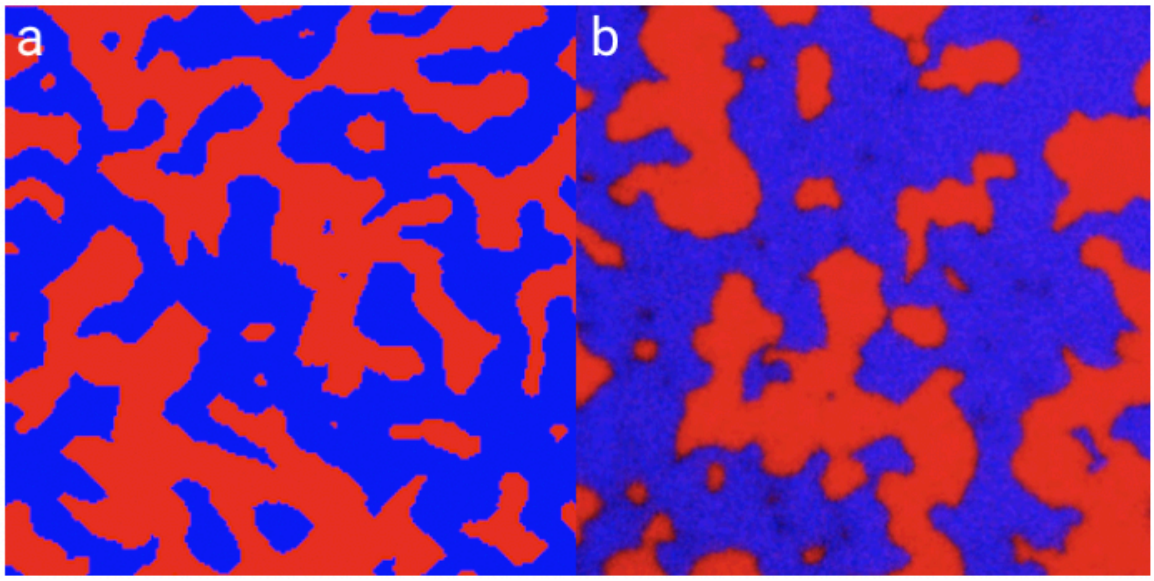

Figure 1.1 a. A still taken from a simulation of spin-coarsening in the Ising model. b. Confocal microscopy image demonstrating coarsening between two mutually-killing strains of cholera.

Two unrelated systems from ostensibly unrelated fields are somehow displaying strikingly similar behavior [35], [36], suggesting that a universal process may be at hand here.

In the Ising model, electrons are placed on a lattice with randomly-aligned spins [37]. Based on energetic interactions with neighboring electrons, each electron spin has some probability of flipping. Over time, energy is minimized by progressively greater local alignment of electron spins, causing "islands" of spin-up and spin-down electrons.

In our experimental system, two strains of *V. cholerae* which could kill each other on contact via the Type VI secretion system ("T6SS") were mixed together and inoculated onto an agar plate, forming a biofilm comprising two competitive strains [38]. We observed that over time, the initially well-mixed strains "coarsened", forming isolated "islands" of one strain or the other. Indeed, a partial differential equation model, multiple simulation models, and this experimental evidence all suggest that if two well-mixed strains can kill each other on contact, they will de-mix as a function of time via "Model A" coarsening—a close cousin of spinodal decomposition, known as "Model B"—the same universality class of coarsening present in the Ising model with "Glauber soon flips" [36]. Briefly, there is an effective "energetic" cost to a bacterial cell surrounded by competitors, who will likely kill the cell and reproduce into the space it once occupied, precisely analog to an electron spin being flipped by its neighbors (it is of note that neither system conserves individual "particle" number).

In microbial communities, constituents often face "public goods dilemmas" [39], [40]. In the world of microbes, many nutrients must be metabolized outside of the cell (*i.e.* "in public"), but this extracellular metabolization requires cells to secrete metabolites [41]. Once metabolites are secreted, the resultant metabolic goods are available to any cell from any strain or species, as long as it happens to be sufficiently close-by. Thus, "cheaters" in a biofilm can reap all the benefits of extracellular metabolization while paying none of the cost, leading to a competitive disadvantage for the cells which do the work of metabolite secretion. The only general solution to this problem is for microbes to become genetically assorted, *i.e.* surrounded by their kind (*e.g.* "producers") and isolated from other species (*e.g.* "cheats"). In densely populated biofilms, achieving this kind of genetic assortment

after the fact is nigh impossible; there's no space for any one species to grow into and claim as its own. T6SS plays a unique role in these environments: because it allows cells to kill non-kin neighbors via rapid lysis, it *creates* space into which new cells can reproduce, allowing genetic assortment even in the types of densely populated environments common in nature. Because T6SS allows cells to become genetically assorted (or, equivalently in this context, energetically de-mixed), cells are free to produce public goods without the risk of other species taking advantage of their work—thus, by enabling cells to kill, T6SS should allow them to cooperate.

Indeed, a phylogenetic analysis across hundreds of genomes shows that not only is the number of T6SS-related genes in a genome positively correlated with the size of the secretome (the portion of the genome associated with the secretion of extracellular products), but that it explains 90% of the variance in secretome size. Of course, while this is consistent with our predictions, it does not prove that the relationship between T6SS and cooperation is causative.

1.2 Activity from Death and Reproduction

Inside a biofilm, cells are immotile and largely athermal. They are usually suspended in some amount of extracellular matrix product, have shut off genes responsible for the production of flagella, and are too large (~micron-sized) to be susceptible to significant thermal fluctuations in this medium. Moreover, these cells are certainly not in equilibrium: they metabolize nutrients, grow, reproduce, kill, and die. What could such a system possibly have in common with an equilibrium atomic solid?

In the equilibrium systems usually considered in statistical mechanics, the fluctuation-dissipation theorem tells us that in energy-dissipating processes, there is a relationship between the fluctuations experienced by constituent particles and their response to applied perturbations [42], [43]. As a brief example, consider Brownian motion: particles are pushed around by thermal fluctuations of a fluid, converting heat to movement. This is conjugate to drag, wherein a moving particle slows down and loses energy to heat. The ambient temperature mediates the relationship between fluctuation and dissipation.

Presume that there exists an *effective* fluctuation-response relationship in a "cellular solid" like a biofilm. Here, instead of random thermal fluctuations providing kicks to constituents, forces from reproduction and death would perturb constituents. In the homeostatic limit—where birth and death are roughly balanced—Risler, Peilloux, and Prost derive a theoretical model of a cellular solid which obeys just such an effective relationship [13].

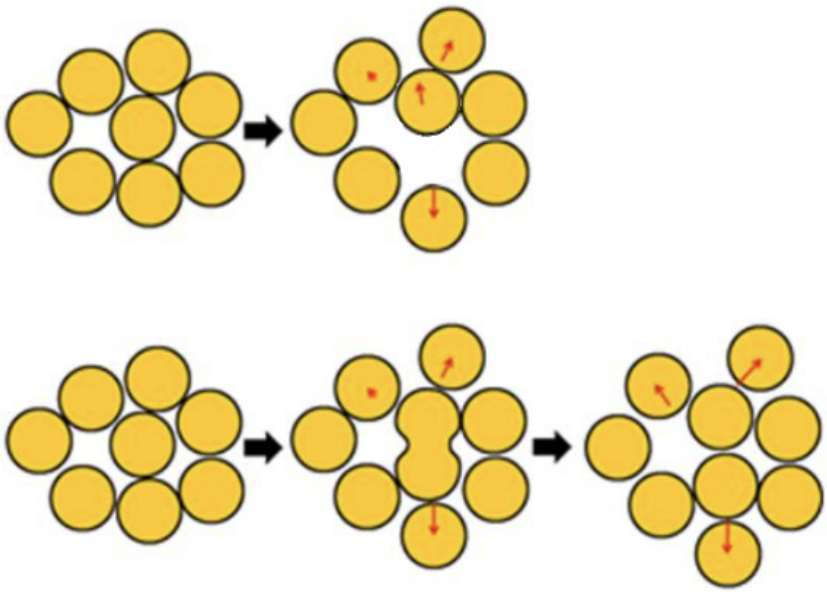

Figure 1.2 a. In thermal systems, random thermal fluctuations result in constituents being perturbed from their positions. b. In athermal cellular systems, forces from reproduction and death similarly perturb constituents.

In the study where this model is derived, the authors suggest that it might be experimentally checked by measuring the surface fluctuations of the solid, and comparing measured height-height correlation functions to predictions made from the solid's mechanical and cellular properties (viscosity, activity rate, numerical density, *et c.*). Using white light interferometry to measure biofilm surface topographies, we found that although biofilms are far from equilibrium systems, their surface-height fluctuation spectra resemble those of thermal permeable membranes, wherein the thermal temperature is replaced by an effective temperature that scales with the amount of birth and death present in the solid [33].

As in the previously described coarsening experiments, we used genetically engineered *V. cholerae* to create model biofilms for these experiments. However, because the ability to engineer strains had progressed since that work, this work contains new strains: two strains which are genetically identical to each other ("isogenic") aside from their T6SS weaponry, and which also produce no exopolysaccharides ("EPSes") [30], [31]. In addition, we used a set of control strains which are identical to those previously described, but which cannot kill on contact. The lack of EPSes gives us a good experimental model of the biological solids discussed in *Risler, et al.*, and the mutual killer/nonkiller strains allow us to discretely choose an activity level without unintentionally modifying other cellular processes.

With these strains in hand, we grew nonkiller biofilms and mutual killer biofilms and measured their surface topographies. Before any calculations were performed, there was a clear topographic difference between the two biofilm phenotypes:

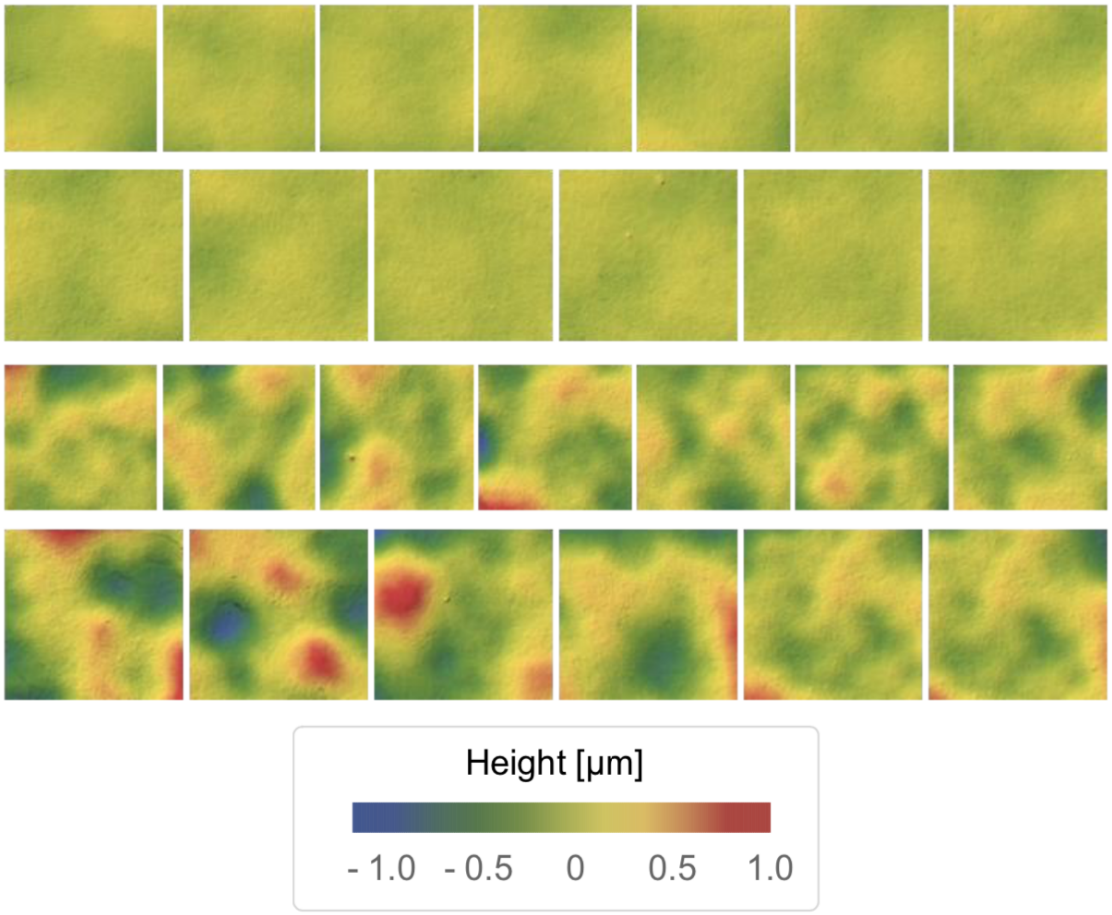

Figure 1.3 a. (top two rows) Nonkiller biofilms appear superficially smooth and flat. b. (bottom two rows) Mutual killer biofilms appear significantly rougher on all discernable length scales, exhibiting notably larger fluctuations.

From these topographies, we calculated height-height correlation functions and used the methods prescribed in *Risler, et al.* [13] to extract an effective temperature for each biofilm. We found that the mutual killer biofilms, on average, had effective

temperatures nearly 18 times higher than those of their nonkiller counterparts, suggesting significantly higher cellular activity rates.

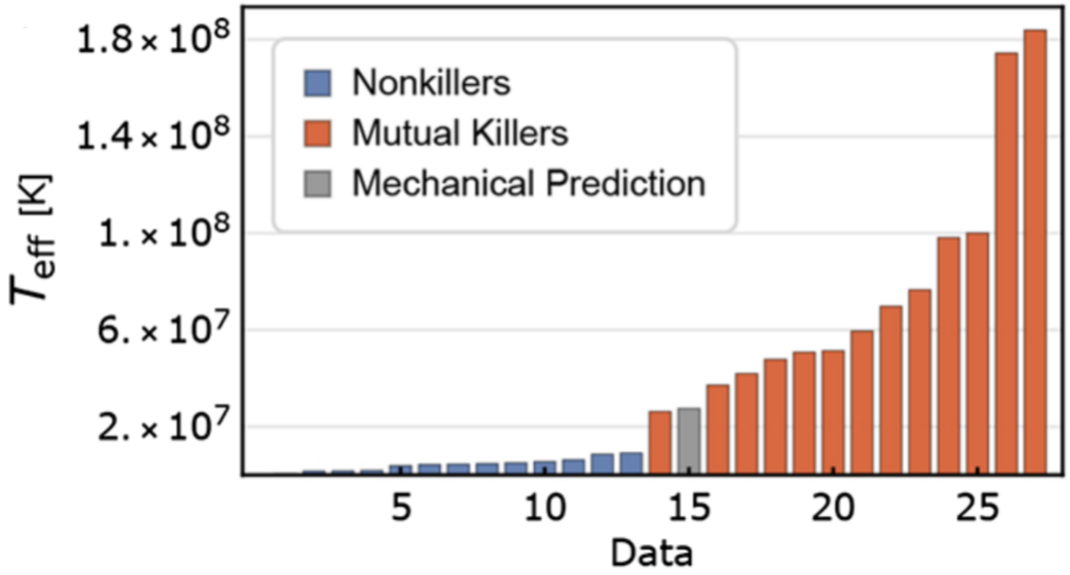

Figure 1.4 Effective temperatures calculated from the measured topographies show a discrete division between nonkiller and mutual killer biofilms. In grey, a back-of-the-envelope prediction of the effective temperature based only on mechanical and cellular properties—*i.e.*, no topographical data was used in its calculation.

While this distinction could only have come from the presence (or lack thereof) of killing, it is not sufficient on its own to validate *Risler, et al.*'s findings. Included in these findings is a prediction for the form of the aforementioned correlation functions, which takes only mechanical properties of the biofilm as its inputs. We measured these properties [17], and found that the mechanically-predicted correlation function lined up with the topographically-extracted ones in both form and magnitude, further suggesting the validity of the model.

Interferometric measurements, however, have a shortcoming: they can only really tell us about topographical features, and leave us—in principle—ignorant of the inner workings of the system we measure. To gain insight into the single-cell dynamics *inside* the biofilm, we wrote a minimal individual-based simulation with tunable killing. With this minimal model, we recapitulated the topographic difference between nonkiller and mutual killer biofilms, the form of the predicted height-height correlation function, and the effective temperature discrepancy.

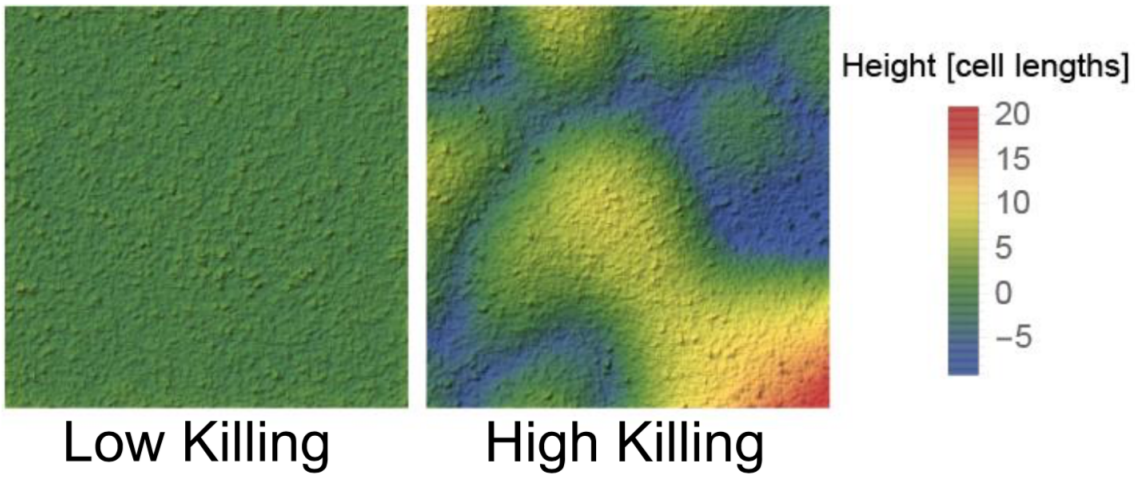

Figure 1.5 Simulations recapitulate the general trend seen in experiments, generated strictly through reproduction and death—no other cellular processes are considered in the model.

With regard to individual cellular dynamics, we found that killing significantly increased cellular movement—even far from individual killing and reproduction events, cells were pushed and pulled by the resultant forces. In line with predictions from *Risler, et al.* [13] (as well as *Ranft, et al.* [14] and *Basan, et al.* [44]), simulated

biofilms with killing were effectively fluidized, whereas biofilms without killing were effectively glassy.

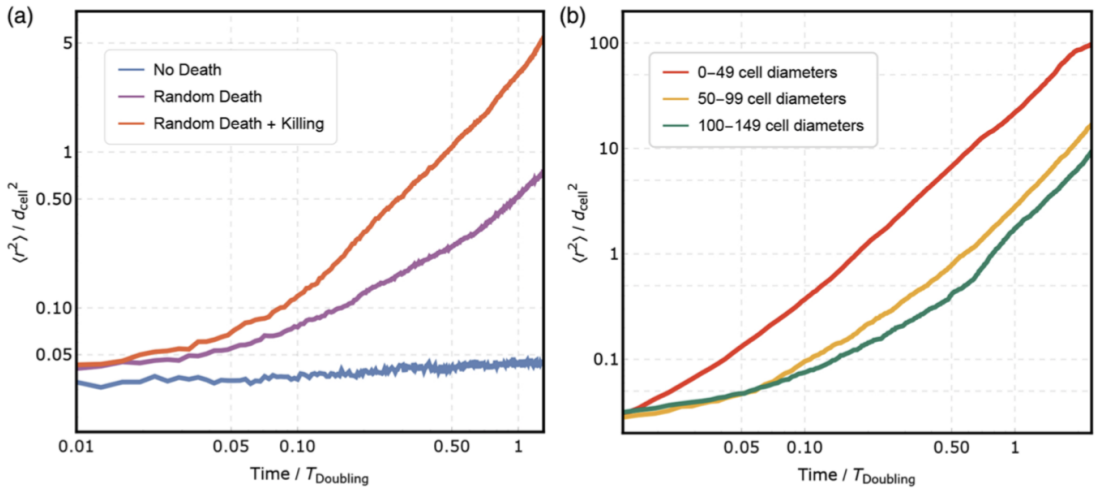

Figure 1.6 a. Average MSDs of cells in simulated biofilms with no death, with random death, and with random death and killing—nonkiller biofilms have little cell death, but they cannot be said to have precisely zero. b. Average MSDs of cells located within given distances of strain-interfaces, where killing occurs. While cells closer to killing interfaces are clearly more mobile, these forces are felt even many cell lengths from reproduction and death events.

Taken together, all of this suggests that reproduction and death in biofilms have unique *physical* consequences. Death and reproduction fluidize biofilms by generating long-distance force chains, as suggested by Refs. [14], [16], [18], [19], [44]. This fluidization is not random, but generates surface-height fluctuations which resemble those of a thermal permeable membrane. From these fluctuation spectra, we can back out cellular

activity rates, with which we can—*e.g.*—distinguish between nonkiller and mutual killer biofilms. The effective fluctuation-response relationship discussed above seems to hold in this far-from-equilibrium system, opening the way for new analyses.

1.3 Viscosity-Independent Cellular Diffusion Through Biofilms

Cellular solids share many similarities with atomic and colloidal solids [28], [45], [46]. We have seen that not only can they exhibit inter-strain coarsening analogous to the Model A coarsening found in the Ising model [32], but that they experience an effective, nonequilibrium form of fluctuation-response relationship driven by death and reproduction, yielding an effective temperature [13], [33]. It is natural to wonder how far these analogies can be pushed: if a bacterial biofilm can have an effective temperature, to what degree does this act like a real temperature? Can it tell us anything more than a simple activity rate?

In thermal, non-living systems, the Stokes-Einstein relation provides a way of understanding diffusion [47]. In these systems, there is a fluctuation-dissipation relationship between viscous drag forces and Brownian motion: explicitly, this implies that viscosity and diffusivity are inversely proportional. This relationship arises from the fact that fluctuations of a particle at rest have the same physical origin as the dissipation of energy experienced by a particle being dragged through the fluid [43]. In a biofilm, however, there is no shared physical origin for cellular diffusion and biofilm viscosity: the former comes from the reproduction and death of individual cells [13], [14], [33], [44], whereas the latter comes (largely) from an extracellular matrix formed by cellular

secretions [4], [10], [28], [48]–[50]. Nevertheless, does some relationship between cellular diffusion and viscosity exist by other means?

To probe the existence of such a relationship, we grew killer biofilms as we did in the previous section [33], but incorporated a new strain which did *not* have its genes for EPS secretion turned off. By performing creep tests, we found that these biofilms had a viscosity about three times higher than that measured in our Matrix- strain. Next, we approached the question of cellular diffusion from a few different angles: PIV on fluorescent tracer beads embedded within the biofilm, a novel interferometric approach based on the "effective temperature" work above, and a minimal simulation model.

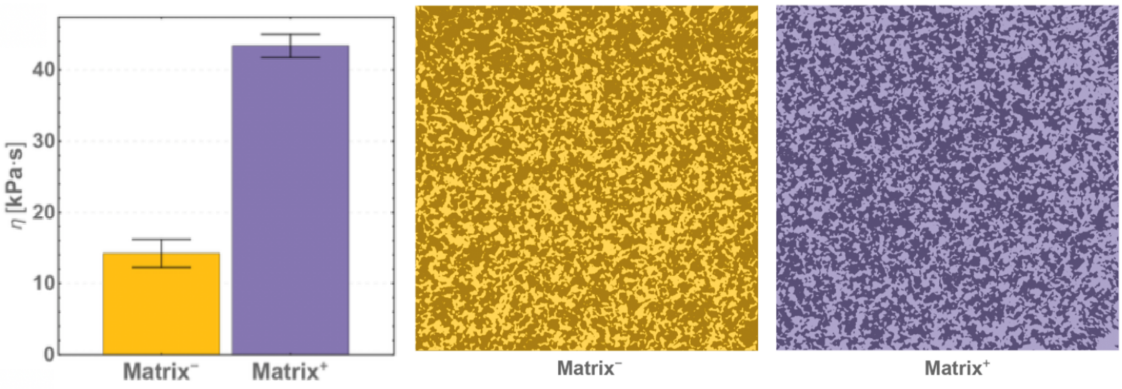

Figure 1.7 a. Measured viscosities of Matrix- and Matrix+ biofilms (shown with standard error) show that the addition of exopolysaccharides increases the viscosity by roughly a factor of three. b. Confocal measurements show that in spite of this increase in viscosity and addition of extracellular products, the amount of coarsening—and thus the amount of killing—is relatively unaffected.

Particularly given that we had previously observed cellular movement with fluorescent tracer beads, they were a natural choice for an experimental measurement of cellular diffusion here. Indeed, for Matrix- biofilms, we were able to measure MSD curves that showed caged-like behavior on short timescales and diffusive-like behavior on long timescales. When we attempted to extract diffusivities from Matrix+ biofilms with this technique, however, we found that the tracer bead motion did not track cellular motion accurately—this is probably due to interactions of the beads with extracellular matrix products. Moreover, it isn't clear that the inclusion of tracer beads has a negligible effect on the cellular dynamics, given that their size is comparable to that of the cells (1-micron spheres *vs.* ~1.2-micron by .3-micron "curved rods"). While we were not able to obtain sufficient data to compare cellular diffusion in Matrix- and Matrix+ biofilms, it was clear that cells *were* undergoing significant motion in both biofilm phenotypes. In an attempt to get more accurate measurements and alleviate the aforementioned tracking issues, we turned toward the interferometric approach developed in the previous section.

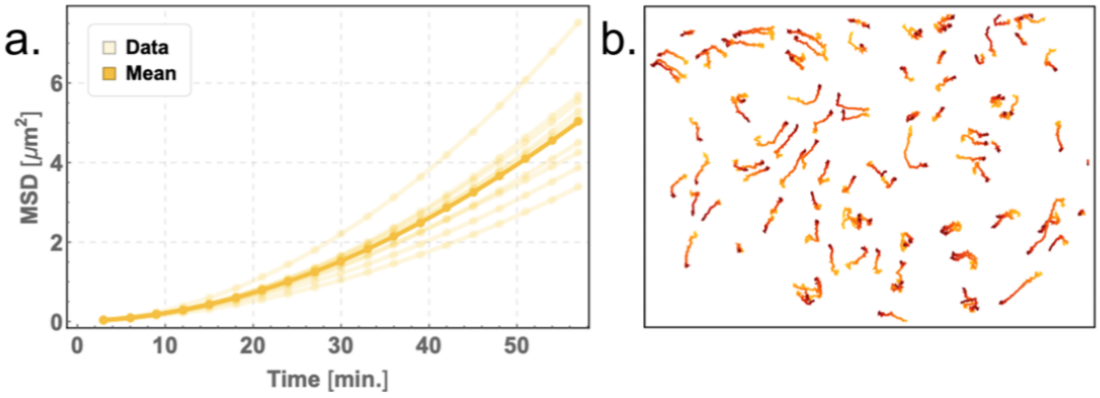

Figure 1.8 a. MSDs measured for tracer beads embedded within a biofilm showed diffusive behavior. b. A visualization of tracer bead paths implies that cells do

experience forces from reproduction and death on relatively short timescales, and thus are displaced within biofilms.

The success of the interferometric method for extracting cellular activity rates from biofilm topographies suggested that we might have more uses for it—to that end, we measured effective temperatures for our Matrix- and Matrix+ biofilms, and found that while they had superficially similar topographies, Matrix+ biofilms had an effective temperature about three times greater than those of their Matrix- counterparts ($p < .004$). Using the previously-measured [17] viscosities, we converted these effective temperatures into effective diffusivities using the generalized Stokes-Einstein relation, and found that unlike the effective temperatures, effective diffusivities were nearly identical ($p > .5$) between Matrix- and Matrix+ biofilms. Not only that, but the extracted diffusivity values ($\sim \mathbf{3 \times 10\ \mu m^2 s^{-1}}$) were reasonably close to those found in the Matrix- tracer bead experiments ($\sim \mathbf{.6 \times 10\ \mu m^2 s^{-1}}$), suggesting—again—that a biofilm's topography does relate directly to its internal cellular dynamics and mechanics.

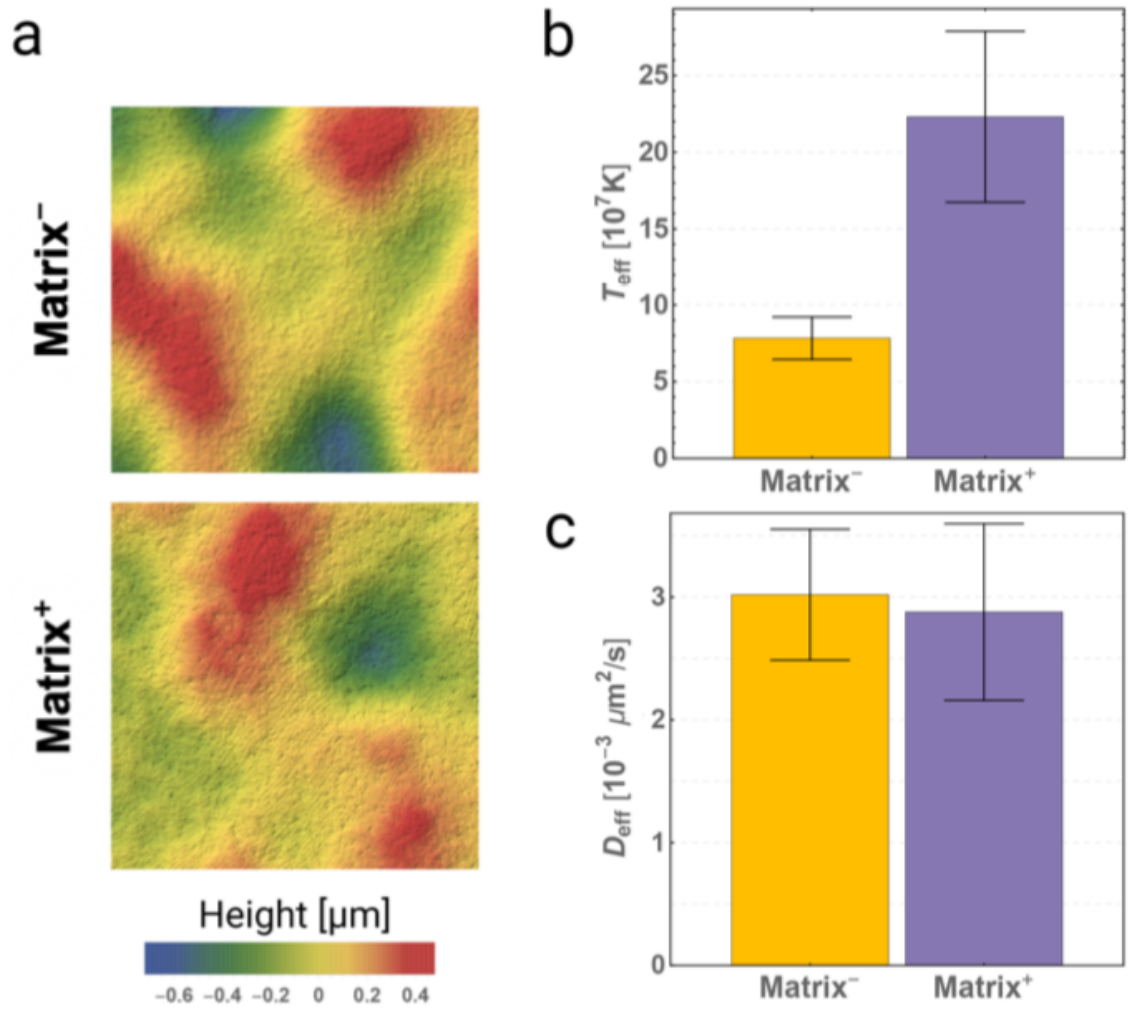

Figure 1.9 **a. Measured topographies for biofilms that do and do not secrete matrix products look superficially similar. b. However, this similarity belies the fact that the effective temperatures differ by a factor of roughly three. c. Once these effective temperatures are converted into effective diffusivities via the Stokes-Einstein relationship, the difference disappears—while Matrix+ biofilms are more viscous, it seems that this allows them transmit forces more effectively, yielding comparable effective diffusivities.**

1.4 Summary

Though biofilms have, to date, primarily been studied by biologists, we are entering an era in which—at least in some subfields—the lines between physicists and biologists are getting fuzzier; where we are sharing an increasing number of our tools. Particularly in light of biofilms' vast "real-world" importance—from teeth [51] to pipes to ships [52], [53] to lungs to hospital bed railings—it has never been more important to use every tool from every field available to understand them. The aim of this thesis is to explore novel instances of nonequilibrium statistical mechanics which arise in bacterial biofilms, with the hope of expanding our understanding of the physical processes which govern their behavior. To that end, we have studied a novel, universal means by which bacterial strains in biofilms carve out space for themselves and possibly evolve cooperativity [32]. We have investigated the equilibrium atomic solid-like behavior of cells within a biofilm, and developed a means by which to quickly and non-invasively test their activity levels [33]. Lastly, we extended the analogy between biofilms and equilibrium atomic solids further, by using an additional mechanical measurement to derive cellular diffusivity levels within biofilms [34].

1.5 Organization

This thesis is organized as follows. First, we explore how different bacterial strains compete and make space inside a biofilm (Chapter 2). We found that inter-strain contact killing generated coarsening that proceeded according to the Model A universality class, and likely helped to evolve bacterial cooperation. This work is published [32]. Next, we discuss our investigation of an effective fluctuation-response relationship in biofilms, generated from death and reproduction (Chapter 3). Here, we found that cellular fluctuations inside a biofilm yield an activity-mediated effective temperature. This work is

published [33], and was extended in (Chapter 4), where we generalized the idea of an effective temperature into an effective—yet kinetic—diffusivity, which turns out to be independent of biofilm viscosity. This work is under revision [34]. Lastly, in Chapter 5, we summarize the work presented in this dissertation, and provide likely future directions for the investigation of biofilms using the interferometry techniques developed herein, as well as new techniques developed in the interim.

CHAPTER 2. KILLING BY TYPE VI SECRETION DRIVES GENETIC PHASE SEPARATION AND CORRELATES WITH INCREASED COOPERATION

(This work is published in Nat. Commun [32].)

2.1 Introduction

By nature of their small size, dense growth and frequent need for extracellular metabolism, microbes face persistent public goods dilemmas. Genetic assortment is the only general solution stabilizing cooperation, but all known mechanisms structuring microbial populations depend on the availability of free space, an often-unrealistic constraint. Here we describe a class of self-organization that operates within densely packed bacterial populations. Through mathematical modeling and experiments with *Vibrio cholerae*, we show how killing adjacent competitors via the Type VI secretion system (T6SS) precipitates phase separation via the 'Model A' universality class of order-disorder transition mediated by killing. We mathematically demonstrate that T6SS-mediated killing should favor the evolution of public goods cooperation, and empirically support this prediction using a phylogenetic comparative analysis. This work illustrates the twin role played by the T6SS, dealing death to local competitors while simultaneously creating conditions potentially favoring the evolution of cooperation with kin.

Microbes are fundamentally social organisms[5], [24], [54]–[56]. They often live in dense, surface-attached communities, and participate in a range of social behaviors mediated through the production and consumption of extracellular proteins and

metabolites. Paradigmatic examples include the cooperative production of digestive enzymes[57], metal chelators[58], signaling molecules[57] and the structural components of biofilms[59]. Many of these extracellular compounds are susceptible to social exploitation, in which non-producing 'cheats' gain an evolutionary advantage. If unchecked, this social exploitation can lead to the extinction of cooperative genotypes[60], [61].

It is widely recognized that the spatial segregation of cooperative microbes away from cheats can solve this cooperative dilemma by ensuring that the investment of cooperators goes to other adjacent cooperative individuals[5], [56], [61]–[63]. Mechanisms creating assortment when organisms expand their ranges via growth into free space have recently received much attention[39], [64]–[68], where robust patterns of genetic segregation can occur via stochastic bottlenecking. However, this mechanism cannot generate genetic segregation within dense, well-mixed communities displaying no net growth, despite the clear ecological relevance of such communities.

2.2 Killing to Separate

One mechanism that has been proposed to potentially generate spatial structure in dense communities is antagonistic interactions among genotypes[5], [11], [59], [69]–[72]. If different genotypes interact antagonistically then wherever a genotype is in the minority they will be killed by competitors at a high rate, resulting in genetically homogenous patches. While mechanisms via which individuals can recognize and kill non-kin have been extensively studied, the consequences of such interactions for the spatial structure of communities have not been explored in detail.

The Type VI secretion system (T6SS) is a potent mechanism of bacterial aggression that can deliver effector proteins directly into eukaryotic cells to mediate virulence by cellular disruption, and into adjacent bacteria to mediate competition by killing non-kin while leaving kin with corresponding protective immunity proteins unscathed[73], [74]. In *Vibrio cholerae*, T6-proficient strains utilize the T6SS to intoxicate T6-deficient eukaryotic predators and diverse proteobacteria, as well as other more closely related *V. cholerae* isolates that lack identical effector immunity pairs[38], [75]–[80]. T6-mediated segregation occurs during co-culture of T6-proficient *V. cholerae* with T6-deficient *E. coli*. Segregation was also predicted to occur between two mutually antagonistic T6-proficient strains[81], and recently demonstrated at the single cell level in co-cultures of *V. cholerae* and *Aeromonas hydrophila*[69].

Here we examine the causes and consequences of neighbor killing via the T6SS on the physical structure of microbial communities. Using a *V. cholerae* experimental system and mathematical modeling, we show that T6SS-mediated killing causes an initially well-mixed population of mutually antagonistic bacteria to phase separate, forming clonal patches that grow larger through time. This phase separation belongs to the 'Model A' class of order-disorder transitions, which is described by the Allen-Cahn equation. We mathematically demonstrate that the spatial structure generated as a consequence of T6SS-mediated killing can favor the evolution of public-goods cooperation by limiting the potential for unrelated 'cheats' to access secreted products. Finally, we bioinformatically show that bacteria with more T6SS systems and effectors dedicate a larger fraction of their genomes to secreted products. While it is too early to rule out alternative hypotheses, this

correlation is consistent with general predictions from social evolutionary theory that spatially structured environments favor the evolution of cooperation.

2.3 Results

2.3.1 Mutual antagonism drives phase separation

Our system illustrates the profound effect of T6SS-mediated killing on emergent spatial patterning of a surface attached population. Mathematical modeling suggests that an initially well-mixed population of mutual killers should rapidly undergo phase separation due to 'selfish herd' dynamics[82], as the cells within genetically uniform groups no longer risk T6SS-mediated death. Indeed, we observe rapid phase separation in three distinct classes of models, all starting with a randomly seeded population on a two-dimensional lattice (Fig. 2.1a). We first developed an individual-based model (IBM; Fig. 2.1b) that simulates bacterial growth, the killing of adjacent competitors and reproduction into empty patches through time. IBMs are appealing, in that they offer an intuitive simulation of discretized, interacting individuals. However, IBMs often lack mathematical transparency, limiting generalization. We thus modeled our system using two distinct, mathematically defined approaches: an ecologically based partial differential equation model in order to gain analytical insight into the dynamics (Fig. 2.1c), and the ecologically-based Ising spin model in order to relate our results to classical modeling of phase separation in statistical mechanics[83] (Fig. 2.1d). In all three modeling frameworks, initially well mixed populations rapidly underwent phase separation. Similarly, initially-well mixed populations of two *Vibrio cholerae* strains (C6706 and 692–79) capable of mutual T6SS-mediated killing underwent phase separation (Fig. 2.1f,i,j). Non-killing

controls (Δ*vasK*, that is, T6SS-) and T6SS- mutual killers cultured at low temperatures which impede T6SS activity[84] remained well-mixed (Fig. 2.1e,g,h).

2.3.2 Spatial analysis

To determine whether our models and experiments undergo the same type of order-disorder transition, we quantitatively examined the dynamics of phase separation in each. We first computed the Fourier-transformed structure factor, $S(q)$. The characteristic wavenumber of clonal groups is $q_m = \frac{\int qS(q)dq}{\int S(q)dq}$, and the height of the peak is related to how often it occurs in the lattice (that is, the strength of patterning at that length scale). At early timesteps (Fig. 2.2a), or for non-killing controls (Fig. 2.2b), $S(q)$ is relatively flat, as expected for a well-mixed population lacking a characteristic length scale. T6SS-mediated killing causes $S(q)$ to increase at smaller values of q (longer length scales) as the population grows increasingly structured. This progression of $S(q)$ is a hallmark of phase separation[85]. For Model A, q_m scales as $q_m \propto t^{-\frac{1}{2}}$ while $S(q_m)$ scales as $S(q_m) \propto t$ [36]. It is ambiguous how to relate simulation time to experimental time; instead, we plot $S(q_m)$ versus q_m. All models (IBM, PDE and Ising) and experiments fall on the same line ($S(q_m) \propto q_m^{-2}$) (Fig. 2.2c), a relationship consistent with the 'Model A' order-disorder phase separation process[86], developed to explain the interaction of atomic spins in systems that lack conservation, and described by the Allen-Cahn equation $\frac{\partial \phi}{dt} = \eta - \mu$, which relates the change in local concentration, ϕ, over time to diffusion and the chemical potential, μ and stochastic fluctuations (see Methods)[87]. To demonstrate this equivalence across wavenumbers, we plot $q_m^2 S(q)$ *versus* q/q_m (Fig. 2.2d). This collapses all data onto one master curve. In fact, due to the universality of non-conserved domain growth, this

collapse could have been expected. Importantly, this universality, shown in Fig. 2.2c,d, demonstrates that while initial conditions—such as the initial number ratio of the two competing strains—may influence the timing of phase separation, they do not influence how phase separation occurs, or that the clonal group size always grows as $\sqrt{t}$. Cellular mobility has a surprising effect on phase separation: rather than impeding phase separation, it accelerates it by enhancing killing at the borders of clonal patches.

To provide biological context for this process of phase separation, we calculated clonal assortment (r), for the IBM (Fig. 2.2e) and the Vibrio experiments (Fig. 2.2f). Assortment, which can be thought of as analogous to Hamiltonian relatedness[67], [88], [89], describes the extent to which clone-mates spatially co-localize after accounting for their frequency in the population (see Methods for details). T6SS-mediated killing resulted in the creation of highly structured populations with high assortment over long length scales (Fig. 2.2e,f). Such assortment can protect diffusible public goods from consumption by competing strains[40], [90].

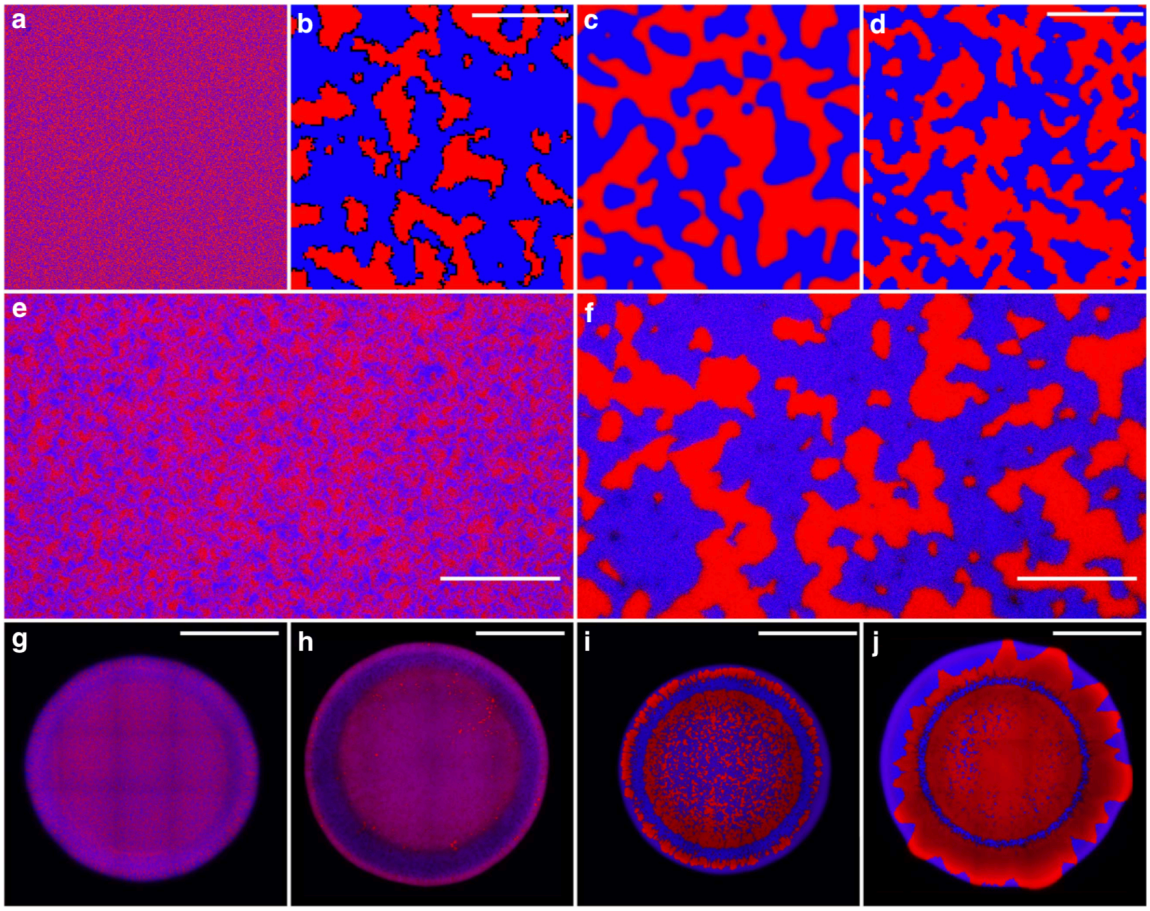

Figure 2.1 **T6SS-mediated killing drives phase separation in dense bacterial populations. We modeled the dynamics of phase separation in fully occupied, randomly seeded square lattices (a). Phase separation between red and blue bacteria capable of mutual killing occurred in an individual-based model (scale bar, 50 cells) (b), in a partial differential equation model (c), and in an Ising spin model (scale bar, 50 magnets) (d). No phase separation occurred between red (C6706) and blue (692–79) T6SS- mutants of *Vibrio cholerae* (Δ*vasK*; e), in contrast to T6SS+ strains (f). We varied the efficacy of T6SS while still allowing for growth by culturing V. cholerae at a range of temperatures: 17 °C (h), 25 °C (i), and 30 °C (j). T6SS- controls cultured**

at 25 °C did not phase separate (g). Scale bars denote 100 mm in e,f, and 1 mm in g–j. Images shown in g–j are representative of four replicate competitions.

2.3.3 Spatial assortment supports cooperation

To explore the effect of T6SS-mediated killing on the evolutionary stability of public goods cooperation, we introduced a diffusible cooperative good into our model. Because all three of our modelling frameworks displayed similar dynamics, we chose the PDE framework because it is the most amenable to analytical investigation. We considered two competing strains: a cooperator that secretes an exoproduct into its environment at an individual cost, and a non-producing cheat that, all else equal, grows faster than the cooperator as it does not pay the cost of production. In this model, cellular growth rates for both strains depend on the local concentration of the diffusible exoproduct. We find that T6SS-mediated killing protects cooperation in two different ways. In a non-spatial (that is, constantly mixed) environment, T6SS-mediated killing can allow cooperators to resist invasion by rare cheats owing to the cooperators' numerical dominance in antagonistic interactions (that is, it creates positive frequency-dependence (Fig. 2.3c), while without T6SS-mediated killing (either because strains lack T6SS, or because the cheat is of the same T6SS type as the cooperator) cheats outcompete cooperators at all starting frequencies (Fig. 2.3a). However, in a spatially defined environment, phase separation driven by T6SS-mediated killing physically separates producers from cheats, expanding the conditions favoring cooperation and allowing them to invade a population of cheats

from rarity (Fig. 2.3d,e; see proof in Supplementary Methods), while cheats ultimately win in the absence of T6SS-mediated killing (Fig. 2.3b).

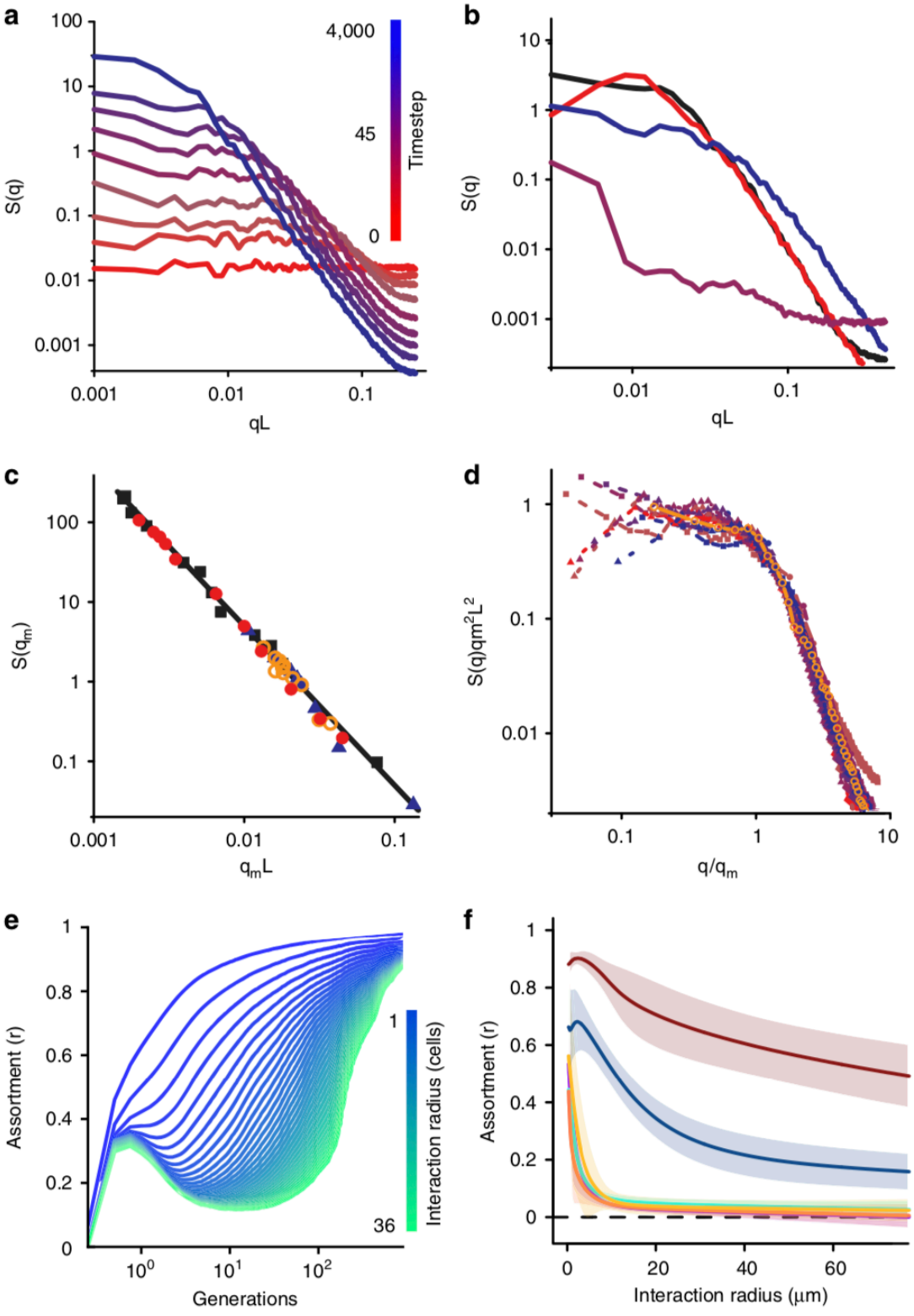
a
100
10
1
0.1
0.01
0.001
S(q)
0.001
0.01
0.1
qL
4,000
45
0
Timestep
b
10
1
0.1
0.01
0.001
S(q)
0.01
0.1
qL
c
100
10
1
0.1
S(q_m)
0.001
0.01
0.1
q_mL
d
1
0.1
0.01
S(q)qm²L²
0.1
1
10
q/q_m
e
1
0.8
0.6
0.4
0.2
0
Assortment (r)
10^0
10^1
10^2
Generations
1
36
Interaction radius (cells)
f
1
0.8
0.6
0.4
0.2
0
Assortment (r)
0
20
40
60
Interaction radius (μm)

Figure 2.2 **The static structure factor $S(q)$, plotted versus wavenumber q multiplied by cell size L for the individual based model (IBM; a) and for experiments (b). In the latter, the red and black lines depict two separate fields of view of *V. cholerae* strains C6706 and 692–79, started at an initial ratio of 1:6, while blue indicates a 1:8 inoculation ratio. The brown line depicts T6SS- mutants, and purple indicates mutual killers grown at 17 °C for 24 h (all others grown at 25 °C). (The brown line is obscured by the purple line, which is nearly identical.) Mutual killing drives phase separation, increasing S(q) at smaller values of q. The relationship between $S(q_m)$ and q_m is summarized in (c) with open orange circles representing experimental data (25°C and a 1:6 inoculation ratio, as in b), black closed squares representing IBM, red closed circles representing PDE model ($d = 0.01$), and blue closed triangles representing Ising model ($T = 1$); all three models and the experiments follow a universal q_m^{-2} trend. S(q) curves collapse when $S(q)q_m^2L^2$ is plotted versus $\frac{q}{q_m}$ (d), indicating that all models and experiments are undergoing the same coarsening process. Color denotes model timestep, as in (a), while symbols indicate type of model or experiment, as in (c). We also examine the creation of spatial structure by calculating a biological metric, assortment *r*, through time across 6,000 updates of the IBM (e) and after 24 h in experiments (f). Mutual killers were grown at 30°C (red), 25°C (blue) and 17°C (green). Defective killers were grown at 30°C (purple), 25°C (teal) and 17°C (orange). Plotted is the mean assortment of four replicate populations (mutual killers) and three replicate populations (defective killers) ± 95% confidence intervals.**

Our models and experiments demonstrate that T6SS-mediated killing can generate favorable conditions for the evolution of public-goods cooperation[5], [39], [63], [91]. This can occur in two ways. First, T6SS-mediated killing induces positive frequency-dependent selection, allowing cooperators to resist rare cheats. Second, T6SS-mediated killing precipitates self-organized structuring of microbial communities, reducing the diversity of cheats that can exploit cooperators. In addition to the predictions of our models previous experimental work has suggested that, via pleiotropic linkage to quorum sensing communication systems, the T6SS can also act as a policing mechanism protecting against the evolution of quorum sensing cheats[92]. Altogether, this suggests that there are three complementary paths via which T6SS-mediated killing could favor the evolution of cooperation.

2.3.4 Association between T6SS and secreted product evolution

Does T6SS-mediated killing have a similar effect in the real world, where ephemeral resources, physical disturbance and intense competition may impede these mechanisms? We approach this question phylogenetically, examining the relationship between the proportion of each genome coding for potentially exploitable secreted proteins and its T6SS complexity, with the rationale that microbes possessing a greater number of T6SSs may face less social exploitation by living in more structured communities. All else equal, genotypes that possess a greater number of T6SSs should form more highly structured patches (higher r), phase separating with a greater proportion of competitor genotypes (that is, those with non-complementary effector/immunity proteins). As a result, we hypothesize that genotypes with more T6SSs should experience less pressure from social cheating imposed by distantly related competitors. There is, of course, an important

caveat to this scenario: while T6SS-based phase separation should effectively exclude competitors, it does not address the *de novo* evolution of cheating from within the clone (for example, Fig. 2.3a,b).

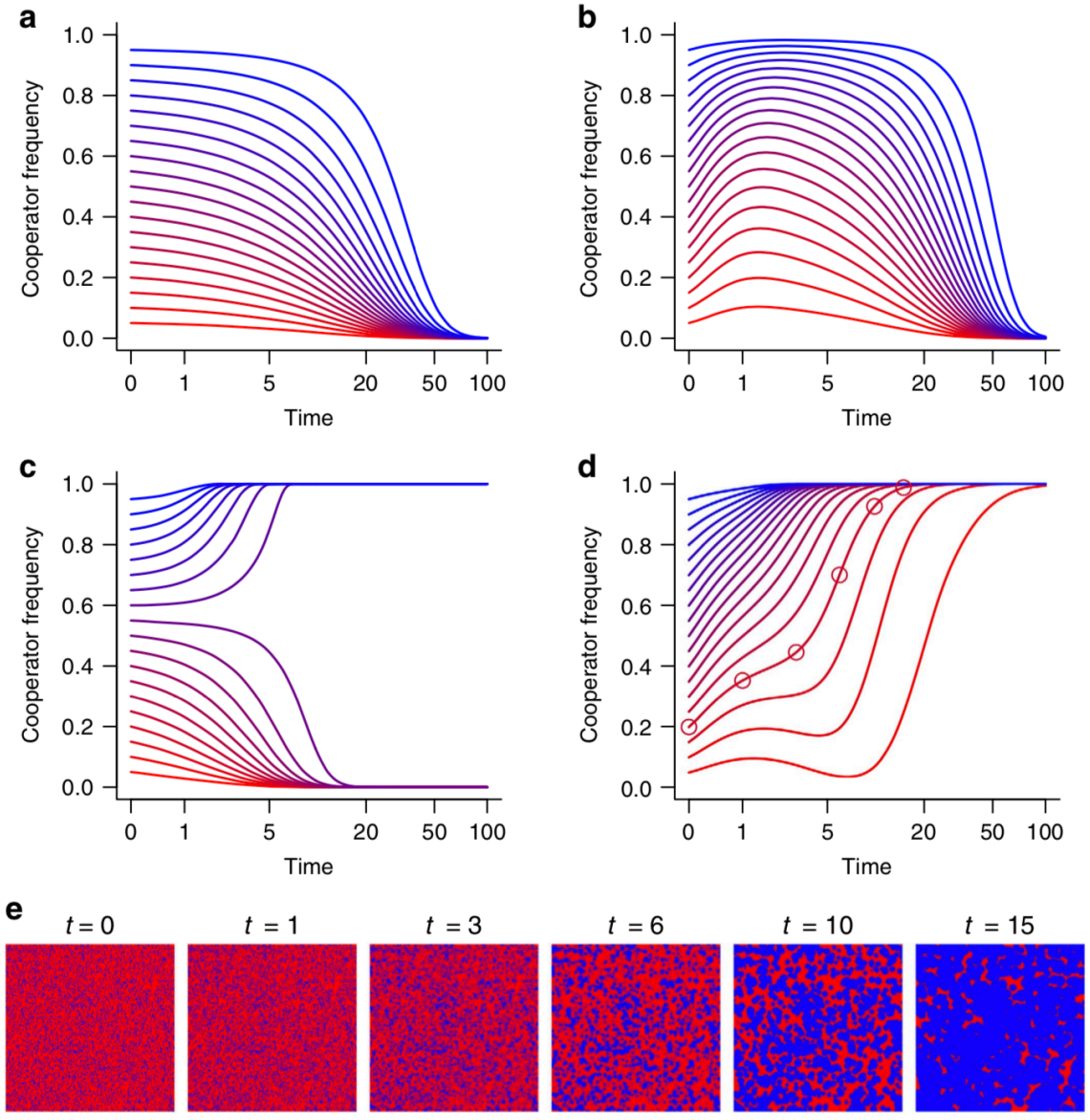

Figure 2.3 Phase separation favors the evolution of cooperation. The dynamics of competition between cooperators and cheats are shown through time for different starting frequencies. In the absence of T6SS-mediated killing, cooperation is not

favored in either a well-mixed environment (a) or a spatially defined environment (b). In a non-spatial environment with killing via T6SS, cooperators can be protected from cheats when common owing to their advantage in antagonistic interactions, but cannot invade from rarity (c). In contrast, the high assortment created by phase separation allows cooperators to invade from rarity and spread to fixation (d). In a–d, line color denotes initial cooperator frequency. The spatial organization of cooperators (blue) and cheats (red) during competition is shown in (e). Panels correspond to the time-points marked by circles in (d).

As a first-order proxy for cooperativity, we measured the proportion of a clone's genome dedicated to secreted proteins (henceforth referred to as 'secretome size'). While many of these secretions may have antagonistic effects on other microbes, they can still be seen as cooperative from the producing cell's perspective, as their kin can benefit from the reduced competition that they create[93], [94]. We constructed a Bayesian phylogenetic mixed model of T6SS-containing Proteobacteria and Bacteroidetes (Fig. 2.4a) using 439 genomes from 26 genera. Secretome size is positively correlated with both the number of T6SSs (Fig. 2.4b,d) and T6SS effector proteins (Fig. 2.4c,e) present, and the model shows an excellent overall fit to the data, explaining 99% of the variance in secretome size (Fig. 2.4f). These results are also robust in univariate analyses and to the inclusion of genome size as a predictor. As our analyses include many closely related strains (for example, many *Helicobacter pylori*, Fig. 2.4a), most (91%) of the variance in secretome size is explained by the phylogenetic relationships among strains. Nonetheless, the number of T6 secretion systems and T6SS effectors are important predictors of secretome size, explaining 8% of the total, and 90% of the non-phylogenetic variance in secretome size.

While the above analysis is consistent with the predictions of our mathematical model showing that phase separation should favor the evolution of cooperation (Fig. 2.3), it is not conclusive. As with any broad-scale phylogenetic analysis, alternative mechanisms explaining this correlation cannot be ruled out. For example, some unknown aspect of bacterial ecology may independently select for both investment in T6SS-mediated killing and exoproduct production. By controlling for phylogenetic variation, our analysis should capture some of this ecological variance, through it does not eliminate it entirely. Alternatively, increases in the presence of dead competitors owing to T6SS-mediated killing can create additional opportunities for horizontal gene transfer[95], which could allow for increased acquisition of genes coding for secretions. However, such an explanation relies on horizontal gene transfer being biased towards genes encoding extracellular secretions. While there is evidence that this bias towards secretions is the case for plasmids and other mobile genetic elements[96], whether this bias occurs when sampling the genes of dead competitors remains to be determined. Detailed analysis of the phylogenetic dynamics of T6SS genes and secretions in individual clades may allow the relative contributions of these hypotheses to our observed correlation to be disentangled.

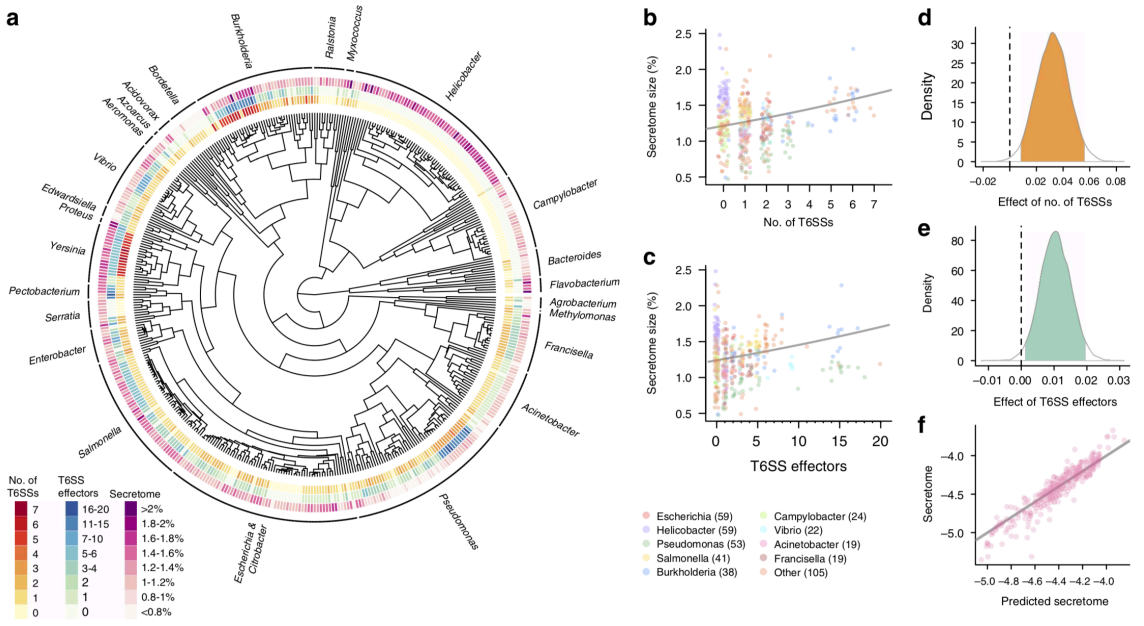

Figure 2.4 **T6SS is associated with investment in other secreted products. The phylogenetic distribution of T6SS, T6SS effectors and secretome size across 439 genomes from the Proteobacteria and Bacteroidetes (a). Secretome size of a strain (expressed as a percentage of genome size) increases with both its number of T6SSs (b) and T6SS effectors (c). Lines are the fits of univariate Bayesian phylogenetic mixed models (BPMMs). Posterior distributions of the effects of the numbers of T6SS (d) and T6SS effectors (e) on secretome size from the multivariate BPMM. Ninety-five per cent credible intervals of the estimates are shaded. Plot of observed against predicted secretome size from the multivariate BPMM (f), including effects of the number of T6SS, number of T6SS effectors and phylogeny. The line represents a 1:1 mapping.**

2.4 Discussion

Phase separation is well-known to drive pattern formation in biology[97], [98], but has mainly been investigated using either Turing activator-inhibitor feedbacks[99], [100], or positive density-dependent movement, described by the Cahn-Hilliard equation[35], [97], [101], [102]. In this paper, we describe a third general mechanism of self- organized pattern formation: targeted killing of non-kin competitors. This drives a 'Model A' phase separation; the kinetics of this coarsening process—described by the Allen-Cahn equation—only depend on a few cellular details. While we restrict our analysis in this paper to the T6SS, the role of antagonistic interactions in structuring biological communities it is probably far more general, applying to diffusible compounds that kill adjacent non-kin in both micro-organisms (for example, antibiotics) and macro-organisms (for example, allelopathy in plants[103] and animals[104]). However, while 'Model A' coarsening is universal, the realization of such dynamics in a densely packed, immobile, athermal system is likely unique to biology.

Physically, this system bears similarities to active matter[35], [68], [97], [102]; phase separation has also been observed in these far from equilibrium active systems, wherein constituents expend energy to move. Phase separation in these systems typically occurs due to differences in mobility as a function of density; constituents move slowly through crowded regions, and quickly through low density regions. Mobility-induced phase separation has been observed (or predicted) in systems as varied as swimming bacteria[105], self-propelled colloids[106], [107], mussels[97], granular rods[108], active filaments[109], [110], rotating particles[45], among other systems[98]. In the current system, activity is derived from reproduction and killing events at high density rather than constituent mobility[13], leading to a 'Model A' transition.

Model A coarsening captures the behavior of a broad array of phase transitions that lack conservation. This transition was originally developed to model magnetization in ferromagnetic materials via the Ising model. Ferromagnetic spins have minimum energy when they align; they do so via Glauber spin flips, leading to a change in the overall magnetization. The physical universality of this transition may be reflected in the strong correlation between secretome and T6SS effectors and apparatuses seen in Fig. 2.4. The microscopic details of the system do not strongly affect coarsening, so long as densely packed cells are equipped with T6SS.

In recent years, there has been a growing appreciation that many microbial behaviors requiring extracellular metabolism are susceptible to social exploitation. Here we show how simple cell-cell aggression can, as a consequence, create a structured population favorable to cooperation. Clearly, many factors contribute to the structure and function of microbial communities[5], [11], [39], [55], [66], [69]–[71], [89], [93]. However, because T6SSs are common (found in 25% of Gram-negative bacteria[111]), and microbes often live in dense communities, phase-separation driven by contact-mediated killing may have a fundamental role in defining the genetic composition and ecosystem-level functionality of microbial communities worldwide.

2.5 Methods

2.5.1 Bacterial Strains and Culture Conditions

Vibrio cholerae fluorescence reporter constructs were chromosomally integrated and gene deletions and promoter replacements were constructed by allelic exchange as described and verified by Sanger sequencing[112]–[114]. *Vibrio cholerae* was routinely

grown at 30°C in Luria-Bertani (LB) liquid medium supplemented with $50\ mg/mL$ of kanamycin or $150\ mg/ml$ spectinomycin when appropriate. For confocal microscopy experiments, overnight cultures were mixed and $0.5\ mL$ was inoculated onto Luria-Bertani agar (1.5%) pads on glass slides, and incubated at 17, 25 or 30°C for 24 h. C6706 and 692–79 were inoculated at a 1:6 initial ratio, as T6SS+ C6706 is more competitive than T6SS+ 692–79 under our assay conditions (it grew from an inoculation ratio of 16.6% to constitute an average of 40–62% of each colony at all three temperatures). To visualize less-advanced stages of phase separation, we used a 1:8 initial ratio of strain C6706 to 692–79. For all images, we show C6706 in red and 692–79 in blue. As expected[112], phase separation occurred similarly when the fluorescence reporters were swapped between strains.

2.5.2 Microscopy and Image Analysis

Laser fluorescence confocal microscopy was performed with a Nikon A1R. The filters used were fluorescein isothiocyanate (for detecting mTFP1, cyan) and tetramethylrhodamine (TRITC) (for detecting mKO, orange). Full colony images were captured in one z-plane using the $20\times$ Plan Apo objective lens and a $2\times$ internal multiplier was applied to capture close-up images. The Galvano scanner was used to scan $2{,}048\ \times\ 2{,}048$ pixels on all images in order to maximize resolution. For every sample, the top and bottom of the colony was located, and a plane in the middle was imaged. The images were stitched and channels were merged using NIS Elements software. To eliminate issues with red–green colorblindness, we present green fluorescence in images as blue.

To calculate the structure factor, $S(q)$, we start with an image from a simulation or experiment, $I(x,y)$. $S(q_x,q_y)$ is the square of the absolute value of the Fourier transform of $I(x,y)$. We then radially average $S(q_x,q_y)$ to get $S(q)=\int S\big(q_x,q_y\big)d\theta$.

To calculate the assortment (r) of the genotype over interaction radius h, we again start out with a binarized image from a simulation or experiment $I(x,y)$ in which we set values of the focal strain g to $+1$ and the competitor strain c to -1. We first convolved $I(x,y)$ with a kernel in which all positions other than the center were set to 1, and the center se to $-((2h+1)^2-1)$, generating the transformed matrix $C(x,y)$. For example, the kernel for distance $h=1$ would be $\begin{matrix}1 & 1 & 1\\ 1 & -8 & 1\\ 1 & 1 & 1\end{matrix}$. Edges within distance h were trimmed. For each interaction radius h (which range from 1-36), we calculated the assortment r of the focal strain g as $r_g=\frac{1-\frac{\overline{C(x,y)}}{2((2h+1)^2-1)}-\bar{g}}{1-\bar{g}}$. r is thus the mean frequency of g within interaction radius h, relative to frequency of g in the population as a whole. r, which ranges from -1 to $+1$, describes the spatial association of each genotype above or below what would be expected from random associations ($r=0$). This definition of assortment is commonly used in social evolution studies, and is conceptually analogous to Hamiltonian relatedness[67], [88], [89]. Similarly, we calculated the assortment of the competitor strain c as $r_c=\frac{1-\frac{\overline{C(x,y)}}{2((2h+1)^2-1)}-\bar{c}}{1-\bar{c}}$.

2.5.3 Phylogenetic Comparative Analysis

N.b.: The following phylogenetic analysis was performed by Luke McNally, and is included for completeness.

We gathered data on the presence of putative T6SSs and effectors across proteobacterial genomes from the SecReT6 database[115]. We restricted our analysis to genera in which there has been experimental verification of the presence of at least one T6SS in at least one strain in SecReT6[115]. This gave data for a total of 439 genomes from the *Proterobacteria* and *Bacteroidetes* of the genera *Acidovorax* ($N = 5$), *Acinetobacter* ($N = 19$), *Aeromonas* ($N = 4$), *Agrobacterium* ($N = 4$), *Azoarcus* ($N = 2$), *Bacteroides* ($N = 9$), *Bordetella* ($N = 10$), *Burkholderia* ($N = 38$), *Campylobacter* ($N = 24$), *Citrobacter* ($N = 2$), *Edwardsiella* ($N = 4$), *Enterobacter* ($N = 11$), *Escherichia* ($N = 59$), *Flavobacterium* ($N = 5$), *Francisella* ($N = 19$), *Helicobacter* ($N = 59$), *Methylomonas* ($N = 1$), *Myxococcus* ($N = 3$), *Pectobacterium* ($N = 5$), *Proteus* ($N = 2$), *Pseudomonas* ($N = 53$), *Ralstonia* ($N = 10$), *Salmonella* ($N = 41$), *Serratia* ($N = 9$), *Vibrio* ($N = 22$) and *Yersinia* ($N = 19$). For each genome we also recorded the genome size and secretome size (number of genes coding for secreted proteins) from PSORTdb[116]. Any T6SS effectors identified in SecReT6 were removed from secretome size counts from PSORTdb to avoid creating a spurious correlation owing to double counting of effectors. To control for the phylogenetic relationships among strains we used the SUPERFAMILY phylogeny[117], which we ultrametricised using the chronpl function in ape[118].

We used a Bayesian phylogenetic mixed model (BPMM) approach to test for an evolutionary association between T6SSs and secretome size. Analyses were implemented

in R using the package MCMCglmm[119]. We treated secretome size as a binomial response variable, expressing it as a proportion of genome size. In all models, we included phylogeny as a random effect to control for the shared evolutionary history of strains, and also included a residual random effect to account for overdispersion. For fixed effects we used an uninformative normally distributed prior with mean 0 and variance of 108. For the phylogenetic and residual variances, we used an uninformative inverse gamma prior with shape and scale both set to 0.001. We ran all models for 6,000,000 iterations with a burn-in of 1,000,000, and thinning interval of 1,000 iterations. We used visual inspection of traces, as well as the Gelman-Rubin test[120], [121] on three independent chains to assess model convergence. In all cases, the potential scale reduction factor was < 1.03. We first fit a model including both the number of T6SSs and number of T6SS effectors as fixed effects. To test the sensitivity of our results we also fit univariate models with number of T6SSs and number of T6SS effectors as fixed effects in isolation. Finally, to control for the potential of non-linear scaling of secretome size with genome size, we ran a model with number of T6SSs, number of T6SS effectors, and the log of genome size as fixed effects. In all cases, both the numbers of T6SSs and T6SS effectors show significant associations with secretome size. Statistics quoted are posterior modes, 95% credible intervals, and pMCMC a Bayesian equivalent to the frequentist p value, which is set as twice whichever is smaller of the proportion of posterior samples above or below zero. Values for proportion of variance explained (R-squared) were calculated following the approach of Nakagawa and Schielzeth[122] as the proportion of total variance attributable to the variable in question on the link (logit) scale, but removing the term for the intrinsic variance of the binomial distribution as we are interested in prediction at the level of proportion of the

genome dedicated to secretions, rather than prediction of whether individual genes code for secretions. Total variance was calculated as the posterior mode of the sum of the residual, phylogenetic and fixed effect variance, with the proportional contributions of each component then determined. In addition, we calculated the proportion of non-phylogenetic variance accounted for by the fixed effects by repeating the calculations while neglecting the phylogenetic variance estimates.

2.5.4 Individual-Based Simulation Model

We randomly seeded a 500×500 lattice with an equal number of red and blue cells. Every time step, 5% of the cells were randomly chosen to activate their T6SS systems, killing any adjacent (eight cells surrounding the focal cell) cells of the opposite color. Similarly, 5% of the cells in the landscape were randomly chosen to attempt to reproduce, filling up to one adjacent unoccupied patch with a cell of its color. Rates of killing and reproduction were chosen to provide sufficient temporal resolution of population dynamics while still being computationally efficient. Reproduction was aborted if all neighboring patches were occupied. Within each time step, model updates were propagated sequentially across rows, starting with the first position in the upper left corner. This model was coded in Python and is available upon request.

2.5.5 Ising Spin Model

We randomly seeded a 500×500 lattice with an equal number of '$+1$' and '-1' entries, representing 'up' and 'down' magnetic spins. The eight nearest neighbours of each point in the lattice are summed and multiplied by the entry they circumscribe—if an entry is surrounded by neighbors of its own type, the resultant quantity (the Hamiltonian 'H') is

8; if surrounded by neighbors opposite its own type, -8. We randomly choose a spin in the lattice and calculate H_{old} and H_{new}, where H_{new} is the Hamiltonian which would result if the chosen spin were to flip, and H_{old} the Hamiltonian if the spin were to remain unflipped.

Each spin flips independently, so flipping one spin does not change the sum of its eight nearest neighbors. Because the Hamiltonian for each entry, however, is the product of that sum with the entry itself, the net effect is simply to add a minus sign. Thus, the difference between the energy for the flipped spin and the unflipped spin is $\Delta H = H_{new} - H_{old} = (-H_{old}) - H_{old} = -2H_{old}$.

With this quantity calculated for our randomly chosen spin, we finally calculate $e^{-\Delta H} = e^{-2H_{old}}$, and compare it to a random number between 0 and 1—if and only if it is larger, the spin will flip [123]. This process is applied iteratively, and after 500^2 possible flips, one time-step is said to have passed. In the above discussion, the Hamiltonian is expressed in units of $k_B T$. This proportionality can be adjusted to modify the speed of convergence to the phase-separated state; our simulation used a ratio of unity. No external field was applied. This model was coded in Mathematica and is available upon request.

2.5.6 ODE Model, PDE Model, and Other Modeling Details

For details on these models, please consult the supplement for *McNally, et al.*—the details are beyond the scope of this manuscript.

CHAPTER 3. IMMOTILE ACTIVE MATTER: ACTIVITY FROM DEATH AND REPRODUCTION

(This work is published in Phys. Rev. Lett. [33])

3.1 Introduction

Unlike equilibrium atomic solids, biofilms—soft solids composed of bacterial cells—do not experience significant thermal fluctuations at the constituent level. However, living cells stochastically reproduce and die, provoking a mechanical response. We investigate the mechanical consequences of cellular death and reproduction by measuring surface-height fluctuations of biofilms containing two mutually antagonistic strains of *Vibrio cholerae* that kill one another on contact via the type VI secretion system. While studies of active matter typically focus on activity via constituent mobility, here, activity is mediated by reproduction and death events in otherwise immobilized cells. Biofilm surface topography is measured in the nearly homeostatic limit via white light interferometry. Although biofilms are far from equilibrium systems, measured surface-height fluctuation spectra resemble the spectra of thermal permeable membranes but with an activity-mediated effective temperature, as predicted by *Risler, Peilloux, and Prost* [13]. By comparing the activity of killer strains of *V. cholerae* with that of genetically modified strains that cannot kill each other and validating with individual-based simulations, we demonstrate that extracted effective temperatures increase with the amount of death and reproduction and that death and reproduction can fluidize biofilms. Together, these

observations demonstrate the unique physical consequences of activity mediated by death and reproduction events.

In contrast to nonliving matter, living cells are active: They consume energy and exist far from equilibrium. Densely packed cells form solids, much like nonliving matter, but activity at the constituent level gives rise to new phenomena. Although the study of active matter has primarily focused on activity via constituent mobility—in phenomena ranging from spontaneous flocking to a density-independent fluid-to-glass transition in tissues [18], [46], [109], [124]–[128]—activity can also arise in living systems due to fluctuations in the constituent number, *i.e.*, cellular reproduction and death. Theoretical investigations of apoptosis and reproduction in tissues [13], [14], [16], [44] suggest that fluctuations in the cell number may have a fluidizing effect. In fact, exact analytical relations calculated by *Risler, Peilloux, and Prost* [13] demonstrate that stochastic fluctuations in the constituent number may have observable consequences on the tissue's surface. Specifically, in the low-frequency, long-wavelength limit, they predict that surface-height fluctuations exhibit a spectral structure similar to that of a thermal permeable membrane, with an activity-mediated effective temperature [13]. The experimental observation of this phenomenon would help elucidate the role that nonequilibrium statistical physics can play in the behavior of biological solids, wherein constituent death is unavoidable. However, controlled experiments probing this phenomenon remain elusive, as it is difficult to tune cell reproduction and death rates without inadvertently changing other cellular processes. Furthermore, such effects can be obscured or mitigated by the presence of the extracellular matrix [129], and very high out-

of-plane resolution is required to compare experiments with theoretical predictions (see §3.7.10).

Bacterial biofilms represent a natural model system to experimentally investigate the effects of fluctuations in the constituent number. Because of their overwhelming prevalence, as well as ecological, medical, and environmental impact [1], [3], [7], [51], [130]–[135], these densely packed, surface-attached communities have been the subject of many experimental and theoretical works focusing on their mechanical properties [2], [28], [129], [136]. Here, biofilms function as soft solids wherein cells act as building blocks, much like atoms or colloidal particles. However, unlike nonliving matter, bacteria can reproduce and die; as a result, the constituent number is not strictly conserved. Furthermore, the genetic manipulation of many bacteria—*e.g.*, *Vibrio cholerae*—is quite advanced, permitting the construction of strains for carefully controlled experiments. Much as colloidal particles act as chemically modifiable model atoms, these bacteria can serve as genetically modifiable model "active atoms".

3.2 Methods

To elucidate the role that cell death and reproduction play in the structure and mechanics of biofilms, we use *Vibrio cholerae*; the amenability of *V. cholerae* to genetic manipulation makes it well suited for use as a model system. We utilize two newly-constructed isogenic "mutual killer" strains of *V. cholerae* (SN306 and SN316) which differ only in the toxic effector used to kill the other strain. We also study genetically modified "nonkiller" strains (SN311 and SN318) which cannot kill but are otherwise identical to the mutual killers [30], [31]. All four strains are genetically modified to produce

no extracellular polymeric substances [29], resulting in biofilms that lack internal voids, and have structures resembling stacks of cells sitting on an agar surface (see §3.7.6 for more details). The derivative strains are also engineered to express either the Kusabira Orange (mKO) orange fluorescent protein (SN306 and SN311) or the teal fluorescent protein (SN316 and SN318) for microscopy. The transverse size of the biofilm is measured with nanometer precision out of plane with white light interferometry (ZYGO NewView 8300). Height spatial correlation functions are calculated and found to be consistent with predictions by *Risler, Peilloux, and Prost* [13], permitting us to extract activity-mediated effective temperatures. We find that contact killing increases the average effective temperature by a factor of ~17.7. By experimentally measuring the motion of tracer beads and simulating the motion of cells in biofilms, we observe that biofilms without killing experience a long-lived jammed state, whereas with killing, biofilms are rapidly fluidized [14], [16], [44]. Individual-based simulations demonstrate that cell death significantly mobilizes cells, even at distances many cell lengths away from killing events. Thus, activity via changes in the constituent number significantly alters the properties of active solids in a way that would not be possible with nonliving solids or living solids whose activity is derived from constituent mobility.

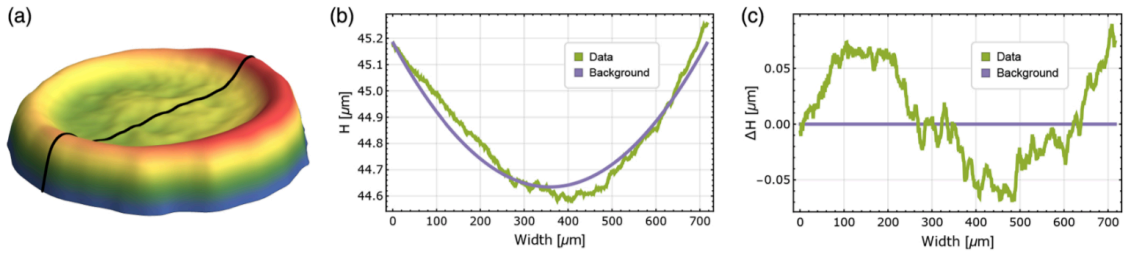

Figure 3.1 a. A 3D profile of a *V. cholerae* biofilm measured via white light interferometry. b. Profile of a 2D slice of the homeland of the biofilm from (a) (indicated by the green line) superimposed onto the best-fit ellipsoidal background. c. The biofilm profile with the ellipsoidal background subtracted.

To investigate the role of death- and reproduction-mediated activity, we prepare biofilms with varying levels of activity. We deposit 1μL of inoculum containing about 8×10^5 cells directly onto a nutrient-rich lysogeny broth agar gel; biofilms then grow at the solid-air interface. Inocula were prepared from overnight shaking cultures and contained the two mutually antagonistic *V. cholerae* strains in ratios of 1∶1.4; nonkillers were inoculated at a ratio of 1∶1.4 as well (see §3.7.1 for more details). The mutual killer strains kill each other on contact via the Type VI Secretion System (T6SS), a microbial warfare mechanism by which bacteria can selectively kill neighboring competitors by injecting them with toxic effectors delivered via a protein spike [76]. The nonkiller strains are identical to the mutual killer strains, except they lack an enzyme essential for the assembly of the T6SS spike. Each biofilm colony was then incubated at 37°C for 24 h. We incubated 18 samples each for mutual killer and nonkiller strains, on four separate agar plates. The resulting biofilms are shaped like spherical caps with a concave, slightly ellipsoidal dimple (Fig. 3.1a), which arises from the coffee-ring derived density profile at inoculation. After incubation, we measured the surface-height profiles within the center of each colony's "homeland"—*i.e.*, the disk whose boundary is defined by the initial inoculation ring—with a ZYGO NewView 8300 interferometer. To focus on local fluctuations in the height, rather than the macroscopic shape, an ellipsoidal background was fit to and subtracted from each of the measured surfaces (Fig. 3.1) (see §3.7.3).

For each sample, we calculated an unnormalized equal-time two-point height correlation function $C(\boldsymbol{r}-\boldsymbol{r}') = \langle \Delta H(\boldsymbol{r}, \mathrm{t}=0) \Delta H(\boldsymbol{r}', \mathrm{t}=0) \rangle$ with the median height set to 0 m. Our scans have a lateral resolution of ~$500\ nm$—about one-quarter of a cell length—and a vertical resolution of ~$1\ nm$. Nonkiller biofilms appear visibly smoother than mutual killer biofilms (Fig. 3.2c).

To directly compare to surface fluctuation predictions [13], we calculate the real part of the Fourier transform of the height correlation function. Specifically, the leading term of this Fourier transform is predicted, in the low-q limit, to be $C(q) = \frac{k_B T_{eff}}{\gamma q^2 + \kappa q^4}$, where k_B is Boltzmann's constant, γ is the surface tension, κ is the bending rigidity, and q is the wave number. Independent mechanical measurements performed as described in Ref. [32] show $\gamma = 0.023 \pm 0.004\ Nm^{-1}$ and $\kappa = 3.4 \pm 0.5\ \times\ 10^{-11} Pa\ m^3$ uniformly across samples (for more information, see §3.7.2). All examined samples exhibit a q^{-2} regime at small q. Note that this functional form of $C(q)$ is predicted to hold in the low-wave-number regime ($qH \ll 1$; for our biofilms, $H = 45.0 \pm 7.5\ \mu m$) [13]; interestingly, we find that it accurately describes the data up to larger q values than expected (see §§3.7.8-3.7.9).

3.3 Measured effective temperatures

Next, we extract an effective temperature for each of the profiled biofilms (Fig. 2b; see §§3.7.7-3.7.8 for details). Because the nonkiller strains cannot kill, those samples establish a baseline level of activity—and thus a baseline effective temperature—against which the mutual killer samples were compared. For mutual killer biofilms $T_{eff} = 7.83 \pm 4.99\ \times\ 10^7\ K$, while for nonkiller biofilms $T_{eff} = 4.43 \pm 2.64\ \times\ 10^6\ K$ (temperatures

reported with standard deviation; a one-tailed *t*-test shows that samples with killing are significantly different than those without [$p = 1.75 \times 10^{-4}$]).

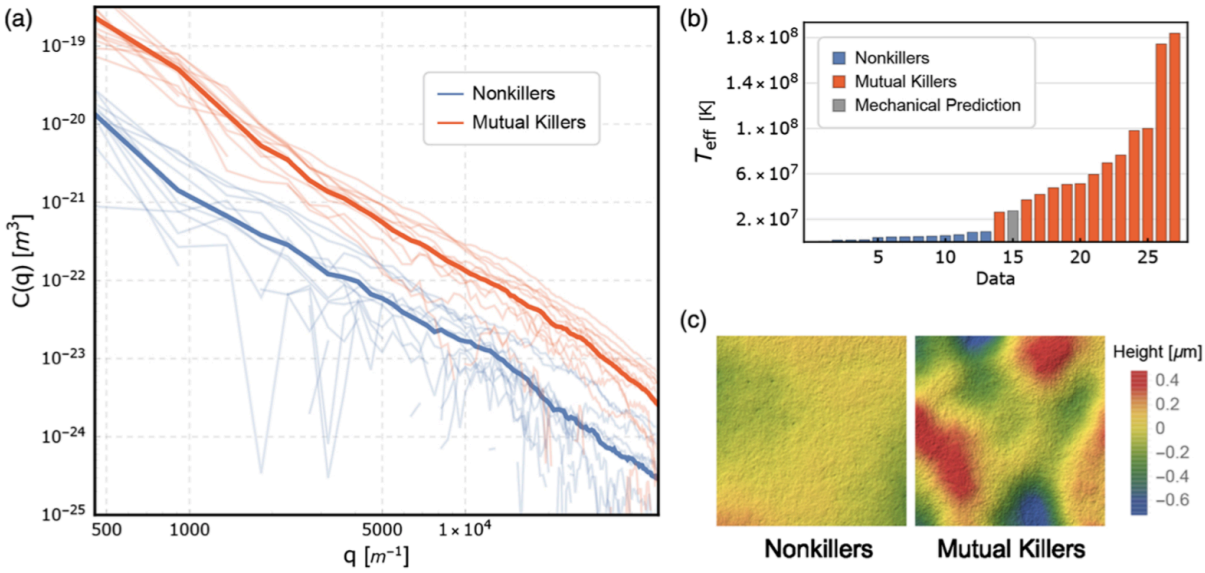

Figure 3.2 a. A log-log plot of the Fourier transformed correlation functions $C(q)$, obtained via interferometry, shown as faint blue (nonkiller) and faint red (mutual killer) lines. Full-opacity lines are averages over 13 nonkiller samples and 13 mutual killer samples. b. A bar plot of all extracted effective temperatures for nonkiller and mutual killer biofilms. Nonkillers and mutual killers are entirely separated from one another. The mechanically-predicted T_{eff} is shown in gray. c. Selected surface relief plots of the homelands of nonkiller biofilms and mutual killer biofilms. The mutual killer biofilm topographies are all "rougher" than their nonkiller counterparts. Each relief plot is 700×700 μm. See Supplemental Material for all relief plots (§3.7.4).

To corroborate our measurements of T_{eff}, we compare to a zero-free-parameter estimate. To leading order, $T_{eff} = \frac{\eta r}{k_B n}$, where k_B is Boltzmann's constant, η is the bulk viscosity, r

is the reproduction rate, and n is the number density [13]. Independent measurements of these parameters (*cf.* §3.7.2) place the predicted T_{eff} in line with the correlation functions extracted by surface metrology for mutual killer biofilms (Fig. 3.2a). While the agreement between this estimate and our data is quite good, that they are of the same order of magnitude suggests that this model [13] has included the most relevant interactions and parameters.

The agreement between these results and the model in [13] is surprising, in part because of differences in the source and distribution of cell death. While *Risler, Peilloux, and Prost* model random death in tissues, here, killing occurs only at interfaces between the two bacterial strains (*cf.* §3.7.5). To understand how contact killing at interfaces affects individual cells, we developed an individual-based model of the biofilm [137] (see §3.7.11 for more details). The model is a physically motivated, biologically minimal framework that focuses on the active matter aspects of biological solids. Member cells interact mechanically as repelling, elastic spheres embedded in a viscous medium as described in [138]. Cells undergo growth, division, and death but are otherwise biologically inert. Death can be induced by interstrain contact killing or can occur naturally. These simulations recapitulate the qualitative and quantitative results of the experiments. Simulating biofilms with high levels of contact killing produces surface topographies that appear qualitatively similar to mutual killer biofilms (see §.3.7.4), while simulating biofilms with very low levels of killing produces surface topographies that appear qualitatively similar to nonkiller biofilms (see §3.7.4). Amplitudes of extracted correlation functions vary with the killing rate, as expected [13] (see §3.7.9).

3.4 Minimal biofilm simulations

We next investigated the dynamics of individual cells via simulations with no death, simulations with random cell death, and simulations of mutual killers with random cell death (Fig. 3.3c). In each case, we measure the mean-squared displacement $\Delta \boldsymbol{r}^2(\Delta t) = \left\langle \sum_i \left[x_{ij}(t) - x_{ij}(t + \Delta t) \right]^2 \right\rangle_{\mathrm{j}}$, where x_{ij} represents the i^{th} coordinate of the j^{th} cell, Δt is the lag time, the sum Σ_i extends over all coordinates i, and $\Delta \boldsymbol{r}^2$ is the mean-squared displacement (Fig. 3.3a). Cells in simulations absent death have flat $\Delta \boldsymbol{r}^2$ curves, indicating that cells remain caged by their neighbors in a long-lived jammed state. Cells in simulations with random cell death have $\Delta \boldsymbol{r}^2$ curves that are initially flat before an upturn to a linear increase in $\Delta \boldsymbol{r}^2$ versus Δt. This indicates that, while cells are caged over short time periods, they eventually break their cages and move diffusively, as suggested in previous theoretical works [14], [16], [18], [46], [124], [125]. "Mutual killer" cells (*i.e.*, cells that experience random death and engage in killing) have $\Delta \boldsymbol{r}^2$ curves that are similar to the random death $\Delta \boldsymbol{r}^2$ curves, suggesting that contact killing fluidizes biofilms in a manner similar to random cell death (Figs. 3.3a and 3.3b) [44].

To investigate how contact killing affects cells that are not at the interface between strains, we simulated biofilms with intercellular killing only (no random death) at a single killing interface and measured $\Delta \boldsymbol{r}^2$ curves for cells at different distances from that interface (Fig. 3.3b). We find that the $\Delta \boldsymbol{r}^2$ grows linearly with Δt for cells at any distance from the interface, though the upturn in the $\Delta \boldsymbol{r}^2$ from caged to diffusive occurs at longer values of Δt for cells farther from the interface. It may initially appear surprising that death localized at an interface can dramatically affect the cell mobility far from the interface. However,

this is consistent with the predictions of Refs. [13], [14], [139]; apoptosis and reproduction are intrinsically local, and yet they can hold mechanical consequences over long distances.

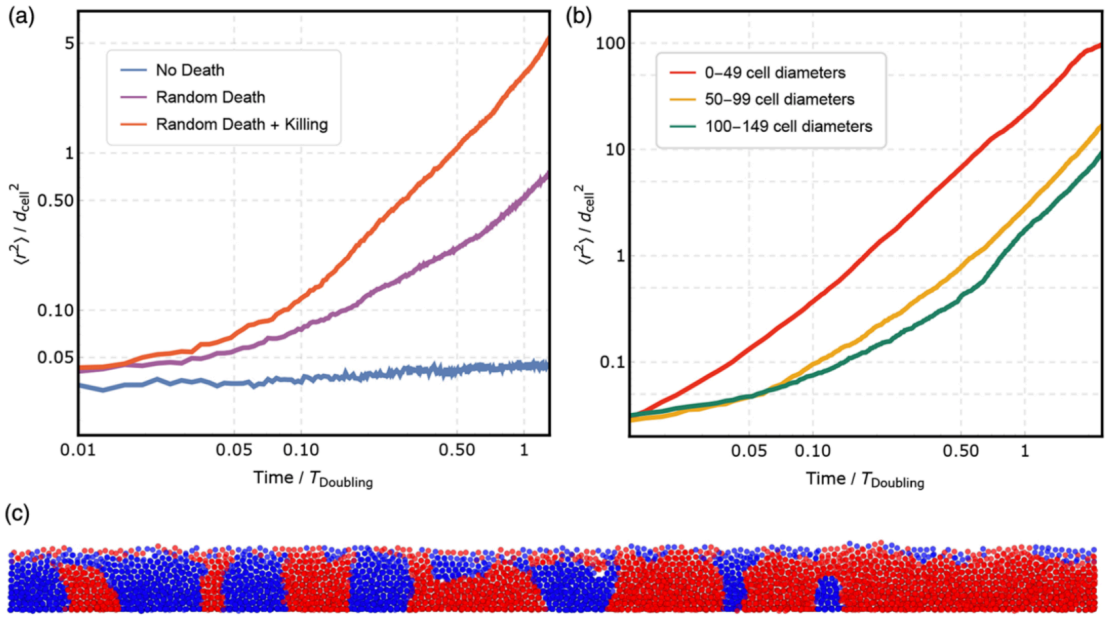

Figure 3.3 a. A log-log plot of the mean-squared displacement (measured in cell diameters^2) of cells in simulated biofilms with no death, with only random death, and with both random death and killing (*cf.* mutual killer biofilms). Nonkiller biofilms have a low level of cell death, but do not exactly correspond to any of the three presented curves. The addition of intercellular killing significantly mobilizes the cells inside the biofilm, fluidizing it. b. A log-log plot of average cellular mean-squared displacements for bins of cells at various distances from killing interfaces. Closer to these interfaces, cells are significantly more mobile. c. A simulated mutual killer biofilm with the two mutual killer strains shown in different colors. See Fig. 3.6 for comparative relief maps of simulated biofilms with low killing and high killing in the style of Fig. 3.2c.

3.5 Tracer beads

Unfortunately, individual cells cannot be directly imaged in our experiments. Thus, to provide an experimentally testable measure of biofilm fluidization from death and reproduction, we simulate biofilms with tracer beads, which do not reproduce, kill, or die. We also allow reproduction to occur only within a distance of 5% of the total biofilm height from the bottom layer of the biofilm [140] (see §3.7.12 for more details). This better replicates the behavior of biofilms grown on agar, where nutrients come from below, permitting us to generate testable qualitative predictions. We observe that simulating contact killing or random death causes tracer beads to move up towards the biofilm's top surface over time and that higher rates of death and reproduction cause the beads to move to the top surface faster. There is no net upward movement of tracer beads in control simulations of nonkillers absent death.

To experimentally test this prediction, we insert 1 μm diameter tracer beads (Bangs Labs) into biofilms and image their locations 13 and 26 h after inoculation (see §3.7.13 for more information). Specifically, we measured the fraction of beads that are in the top third of the biofilm, *i.e.*, the fraction of beads that are within 15 μm of the top biofilm surface. For nonkiller biofilms, the fraction of beads near the surface increased from $0.19 \pm .04$ to $.29 \pm 0.08$. Remarkably, for mutual killer biofilms, the fraction of beads near the surface increased from 0.25 ± 0.05 to 0.91 ± 0.14. The bead distributions are statistically similar at $13\,h$ (two-tailed t-test, $p = 0.327$), whereas at $26\,h$, the bead distributions are significantly different (two-tailed t-test, $p = 0.006$). Thus, the tracer

beads in the mutual killer biofilms are much more mobile than the tracer beads in the nonkiller biofilms (Fig. 3.4).

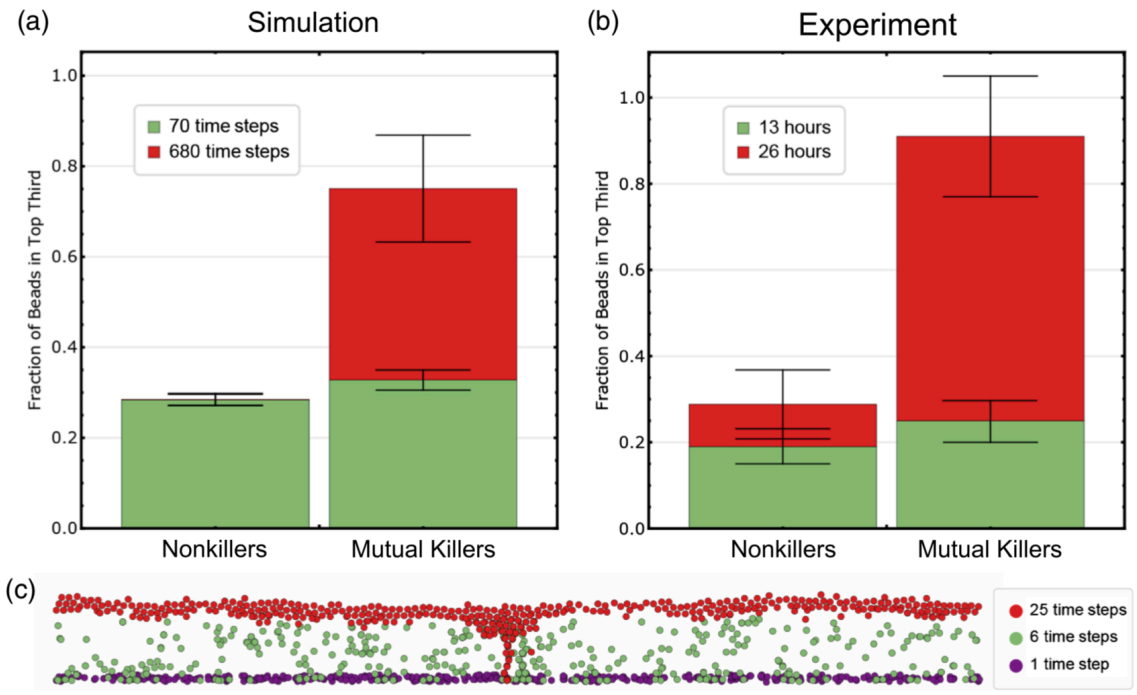

Figure 3.4 a. Simulated biofilms with no death show little change in the tracer bead position over time, but simulated mutual killer biofilms exhibit behavior consistent with that of a convective medium, as seen in cellular aggregates with cell division and death [141], [142]. b. In experiments, tracer beads are convected toward the top third of nonkiller biofilms over time, but mutual killer biofilms are significantly more convective, allowing for nearly all of the tracer beads to move to the top. c. The positions of tracer beads in a simulated mutual killer biofilm are shown at initialization, at an intermediate time, and at a late time. Tracer beads rapidly leave their initial positions and settle at the biofilm top surface.

3.6 Conclusions

The presence of a quantitative relationship between surface topography and cell death opens new avenues for studying both physical and biological properties of biofilms. Just as measuring fluctuations in equilibrium materials permits the calculation of mechanical response functions [42], mechanical and structural measurements of biofilms and tissues can be used to infer death and reproduction rates—quantities that are difficult to measure in densely packed cellular solids. However, further work is necessary to ascertain if the approach employed here would work in biofilms with substantial viscoelastic extracellular matrix secretions [4]. Furthermore, along with other recent results [143]–[145], the observations reported here support the idea that death and reproduction have a fluidizing effect [13], [14], [16], [18], [44], [46], [124], [125] and suggest that a statistical description of biofilms, rooted in the extension of concepts from equilibrium statistical mechanics [32], [146], [147], may yet play a large role in explaining complex microbial communities. Finally, it is surprising that the biofilms studied here exhibit an apparent universality in surface fluctuation spectra with thermal permeable membranes, as well as nonequilibrium tissues [13], despite many differences in these systems.

3.7 Supplemental Materials

3.7.1 Bacterial strains and culture conditions

Both sets of *Vibrio cholerae* strains are derivatives of a streptomycin-resistant El Tor biotype O1 strain (C6706). Bacteria were incubated at 25°C or 30° in lysogeny broth (LB) under constant shaking, or statically on petri plates containing lysogeny broth agar (LB + 1.5% agar). Biofilms were grown on four LB agar plates with nine colonies per plate; two plates were used for nonkillers and two for mutual killers. There was no

significant variance between the data or topographies from the two nonkiller plates or the two mutual killer plates. All plates were simultaneously incubated for 24 hours at 37˚C and measured in alternating order: nonkillers, mutual killers, nonkillers, mutual killers.

Bacterial strains were inoculated from overnight shaking cultures at an initial inoculum volume of 1 μL (~800,000 cells) in stated ratios of two strains. Solid media used are either LB agar in petri dishes or LB agar pads of ~$4mm$ thickness on glass slides.

3.7.2 Independent mechanical measurements

Mechanical measurements were performed on a "Universal Testing Machine" (UTM) manufactured by Zwick Roell. The viscosity, η, membrane tension, γ, and bending rigidity, κ, were measured for use in calculating T_{eff} and the mechanical estimate of T_{eff}.

To measure viscosity, we also had to measure the compressive elastic modulus. To do this, we compressed biofilms between two plates, measuring the stress and strain, and then extracted the slope of a linear fit to stress versus strain. Over 10 replicates we measured an average modulus of $3.1 \pm 1.3\ kPa$.

Viscosity was measured via a stress relaxation measurement. We first applied a force of $\sim 0.02\ N$, and the UTM then measured the force necessary to hold the compression plate at that position over time. The necessary force decreased exponentially over time, with a time constant $0.22 \pm 0.03\ s^{-1}$, measured over 10 replicates. For viscoelastic materials, this time constant is equal to the ratio of the viscosity to the elastic modulus. Using the modulus calculated above, we measured $\eta = 14 \pm 6.2\ kPa\ s$. Using this value of the viscosity, as well as a number density $\rho = 6.25 \times 10^{16}$ and doubling rate

1.67×10^{-3}, we calculate the estimated T_{eff} as $T_{eff} = \frac{\eta k_d}{k_B \rho} = 2.75 \times 10^7$K. Note, this is shear viscosity, not bulk viscosity, as used in [3]. However, based on other measurements of shear and bulk viscosities, we expect these to be of similar orders of magnitude.

The membrane tension, γ, was measured following the method detailed in *Forgacs, et al*. [17]. The experiment was repeated 10 times. While *Forgacs, et al*., compressed a spheroidal cellular aggregate, we compressed a biofilm. The membrane tension in our compressed biofilm acts in analogy to the surface tension in a drop confined between two glass plates. Specifically, following a similar approach to the viscosity measurement, we compress biofilms with a force of 0.02 N and then hold the plate in place. We wait for over 30 seconds for the stress to relax. The biofilm compresses an average of $15.3 \pm 8.7 \mu m$. This allowed us to calculate an average compressed height (the distance between the top compression plate and the agar surface) of $29.7 \pm 11.7 \mu m$. Using the average biofilm radius of $2.0 mm$ and the formula for the Laplace pressure (as done in *Forgacs, et al*.) we obtain $\gamma = 0.023 \pm 0.004\ Nm^{-1}$.

To measure the bending rigidity, we use the classic formula $\kappa = \frac{E\, h^3}{12(1-\nu^2)}$, where h is the mean height of the biofilm and ν is the biofilm Poisson's ratio. We take ν to be 0.5, in range of what has been measured for biofilms [148], [149]. We directly measure the mean height, averaged across entire biofilms, which is $45.0 \pm 7.5\ \mu m$. Combined with the modulus of $E = 3.1 \pm 1.3\ kPa$, this yields $\kappa = 3.4 \pm .45 \times 10^{-11}\ Nm$.

3.7.3 Topographic background subtraction

A *V. cholerae* biofilm very reliably grows such that the region of growth corresponding to the site where the initial inoculum volume was placed—*i.e.*, the "homeland"—takes the shape of a concave ellipsoidal cap. Because we are interested in the fluctuations on this ellipsoidal surface, we calculate the average curvature in two principle directions and subtract the ellipsoidal background defined by those curvatures.

3.7.4 Consistent roughness differences

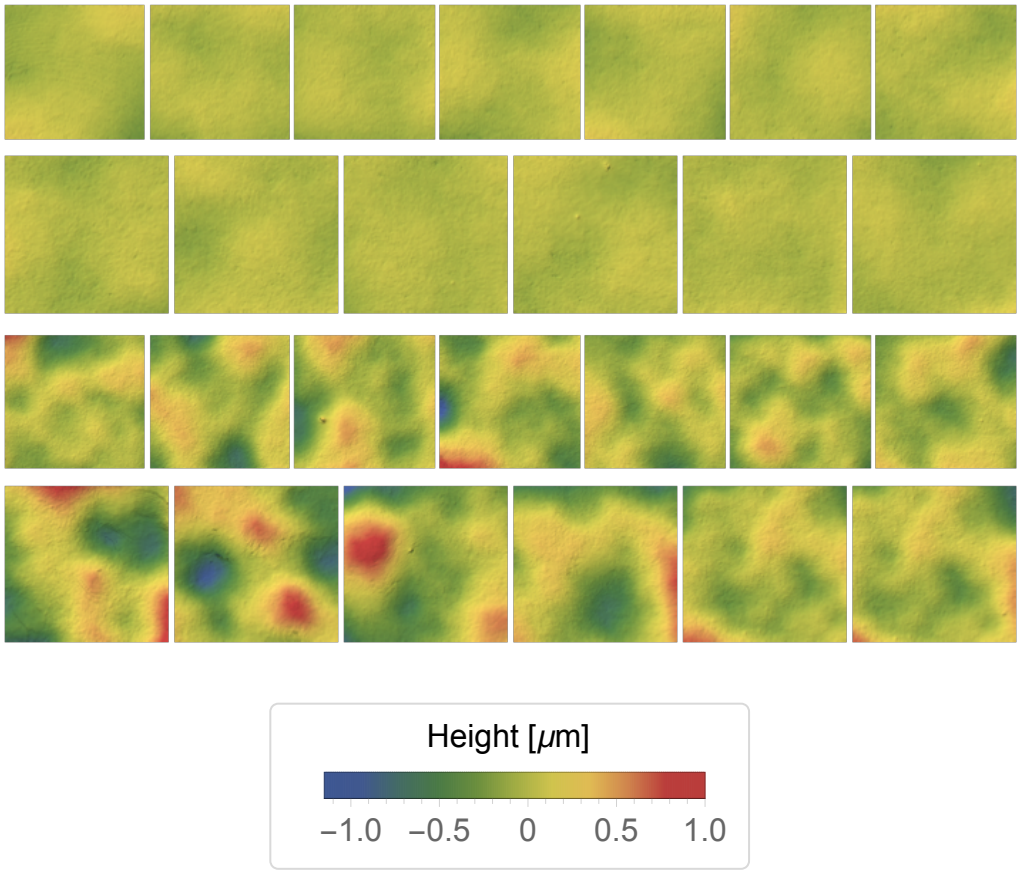

Figure 3.5 Relief plots showing the difference between nonkiller (rows 1-2) and mutual killer (rows 3-4) surface topographies.

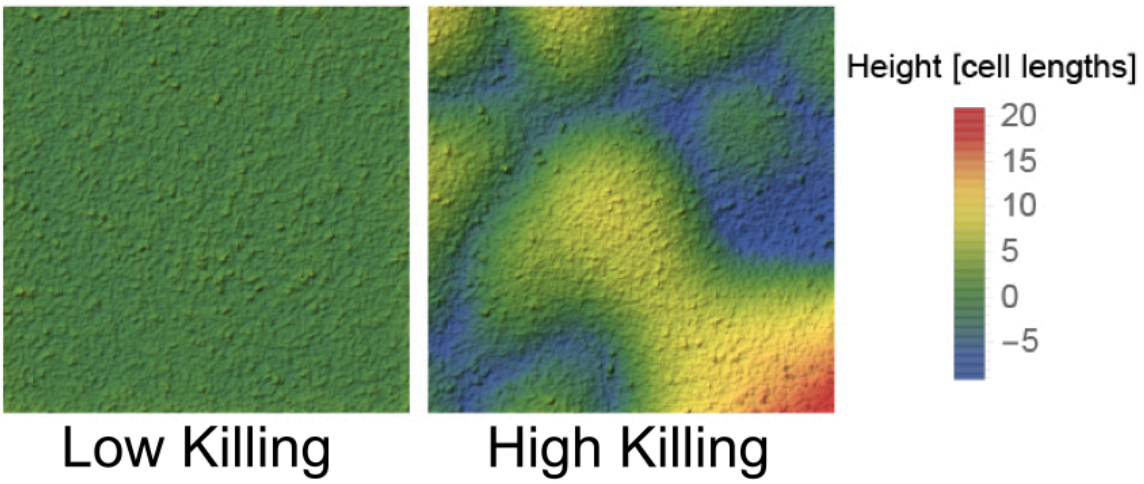

Figure 3.6 Simulated biofilms show a similar disparity. A biofilm with a low amount of killing (*cf.* "Low-Killing Sim" in Fig. 3.11) is shown to the left of a biofilm with 10 times more killing (*cf.* "High-Killing Sim" in Fig. 3.11), revealing fluctuations that are both greater in magnitude and which persist over greater length scales.

3.7.5 Clonal coarsening and surface roughening

Because all mutual killer samples exhibited surface roughening at a larger height scale than their nonkiller counterparts, we also performed patch coarsening measurements [32] using confocal microscopy to see if the coarsening was similarly consistent. Indeed, none of the nonkillers exhibited coarsening clonal patches, but all of the mutual killers did. Nonkillers had mean domain length scale of $45.1 \pm 5.6\ \mu m$, whereas mutual killers had a mean domain length scale of $170 \pm 19.8\ \mu m$. Moreover, coarsening was consistent throughout the layers of a biofilm, as shown below in Figures 3.7 and 3.8.

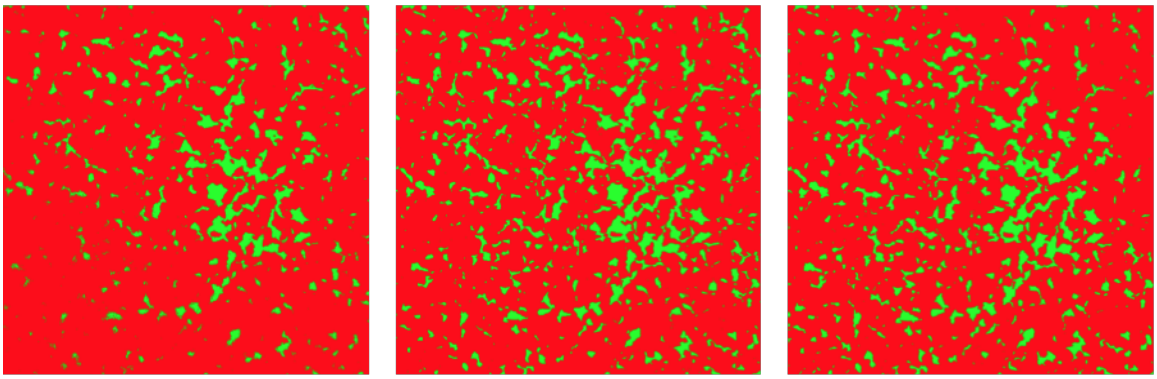

Figure 3.7 Confocal microscopy shows that the bottom, middle, and top of a mutual killer biofilm show similar levels of patch coarsening.

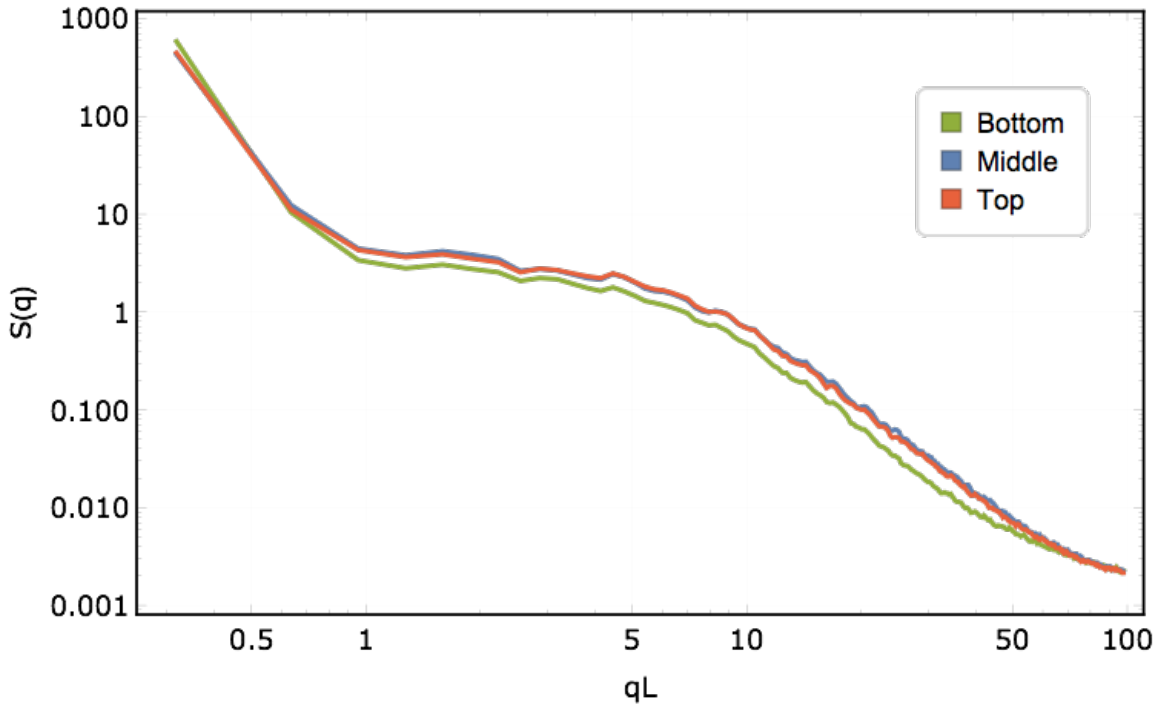

Figure 3.8 Structure factors for the above images are shown, demonstrating very similar coarsening structures throughout the vertical extent of the biofilm.

3.7.6 Internal biofilm structure

The biofilms in this work are homogenous type without large voids; this is validated by confocal measurements (Fig. 3.9). Indeed, these biofilms are primarily dense stacks of cells. Thus, they compare well to the homogeneous tissue model of ref. [13].

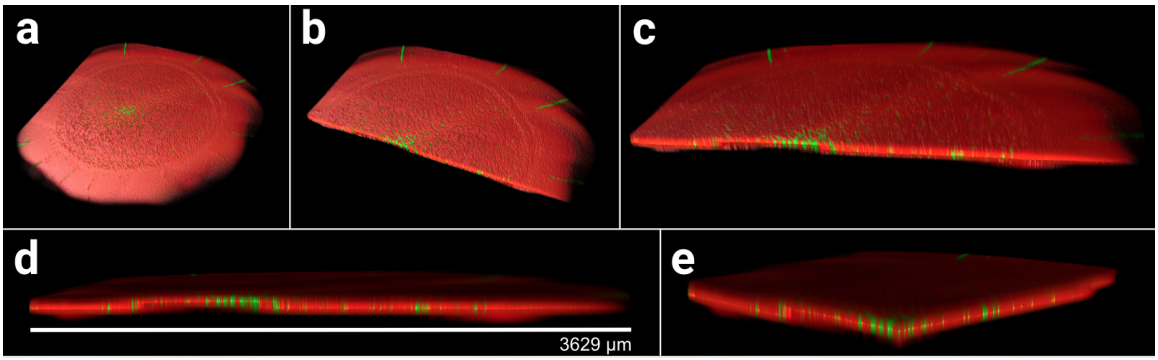

Figure 3.9 Panel a) shows a three-quarters overhead view of a biofilm (one strain is red fluorescent and the other is green), while b) shows this same view, but sliced such that internal structure is visible. Panel c) shows a closer view of the data in panel b). Panel d) shows a profile view of the biofilm, indicating both that there are no voids and that the coarsening is consistent throughout the vertical extent of the biofilm. Panel e) shows the internals of the biofilm on two orthogonal axes to demonstrate that the properties shown in d) are not specific to a particular region of the biofilm.

When allowed to grow freely, cholera cells double every ~20 minutes. While cellular lysis due to killing takes only about 40 seconds, the timescale on which these killing events take place is unclear. However, further high-resolution confocal scans place a size limit on any potential voids or interfacial depletion zones at ~3 microns, as shown in Fig. 3.10.

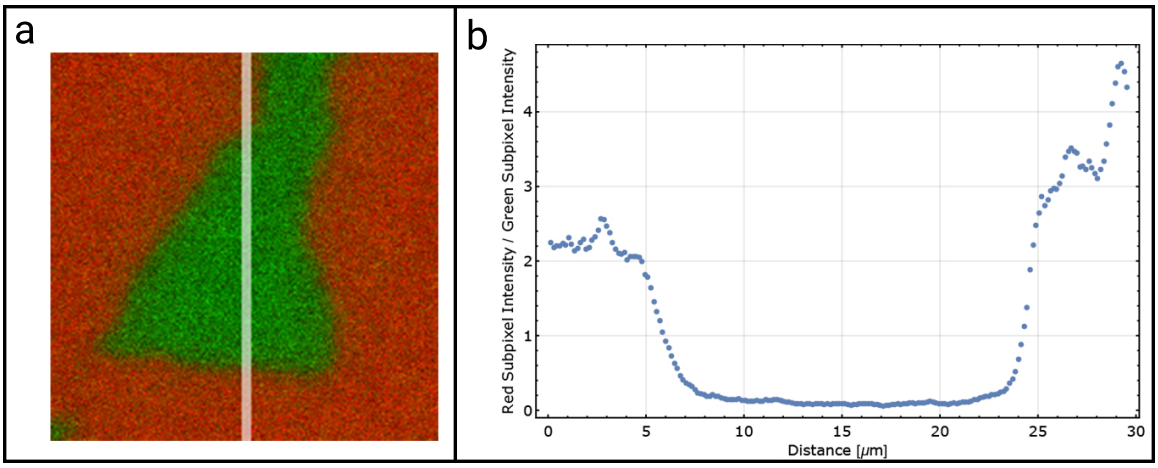

Figure 3.10 Panel a) shows a 30-micron by 30-micron view of green cells surrounded by red cells; the superimposed white line denotes a .75-micron-wide patch used to generate the plot in b). Panel b) shows the mean ratio of red subpixel intensity to green subpixel intensity within the white line. The width between solely red and solely green areas puts an upper limit on the maximum possible void size at ~3 microns.

3.7.7 Criterion for analysis

In the homeostatic limit, the median height should be roughly equidistant from the minimum and maximum heights. In cases where the extrema are far from the median, it is likely that our spherical background subtraction scheme overcorrected due to large fluctuations at the edge of our field of view. To remove these overcorrected samples, we analyzed only samples which satisfy

$$\frac{2}{3} \leq \left| \frac{h_{max}}{h_{min}} \right| \leq \frac{4}{3}.$$

3.7.8 Calculating correlation functions and effective temperatures

Real-space correlation functions were calculated in *Mathematica* as follows:

```
ArrayCorrelator[ar_] :=
 With[{L = Length@ar},
    ParallelTable[.5/(1 - i^2/L^2) *
       Mean@Flatten[ar (PadLeft[ar, {L, L + i}][[All, ;; L]] +
            PadLeft[ar, {L + i, L}][[;; L, All]])], {i, 0, L - 1},
     Method -> "FinestGrained"]]
```

The above code is an implementation of the standard equal-time two-point correlation function,

$$C(\boldsymbol{r}-\boldsymbol{r}') =< \delta H(\boldsymbol{r}, t=0)\delta H(\boldsymbol{r}', t=0) >$$

Once this correlation function was calculated, we took the real part of its Fourier transform. The large majority of the Fourier transformed data points are positive, but close to zero (due to the q^2 and q^4 drop-off). However, some are below zero due to noise, so we subtract the median $C(q)$ value of each curve to ensure that they die off to zero for large q—a non-zero $C(q)$ value for large q would be unphysical. To calculate the effective temperatures, we fit our measured spectra to the leading order expression derived in [13], $C(q) \approx \frac{k_B T_{eff}}{\gamma q^2 + \kappa q^4}$. We used values of $C(q)$ corresponding to q values up to 1.77×10^4.

While the predicted functional form of $C(q)$ is expected to be valid in the limit that $qH \ll 1$ (we have $H = 45.0 \pm 7.5\ \mu m$), we find that it accurately describes the data from our biofilms to larger q values than expected. As a check, we calculated the mean ratio of effective temperatures between mutual and nonkiller biofilms as a function of maximum q value kept in the calculation—*i.e.*, our biofilms were large enough to give us ~350 q values,

so we calculated mean ratio of the effective temperatures, using the lowest 1, 2, … 350 q values. The results are as follows:

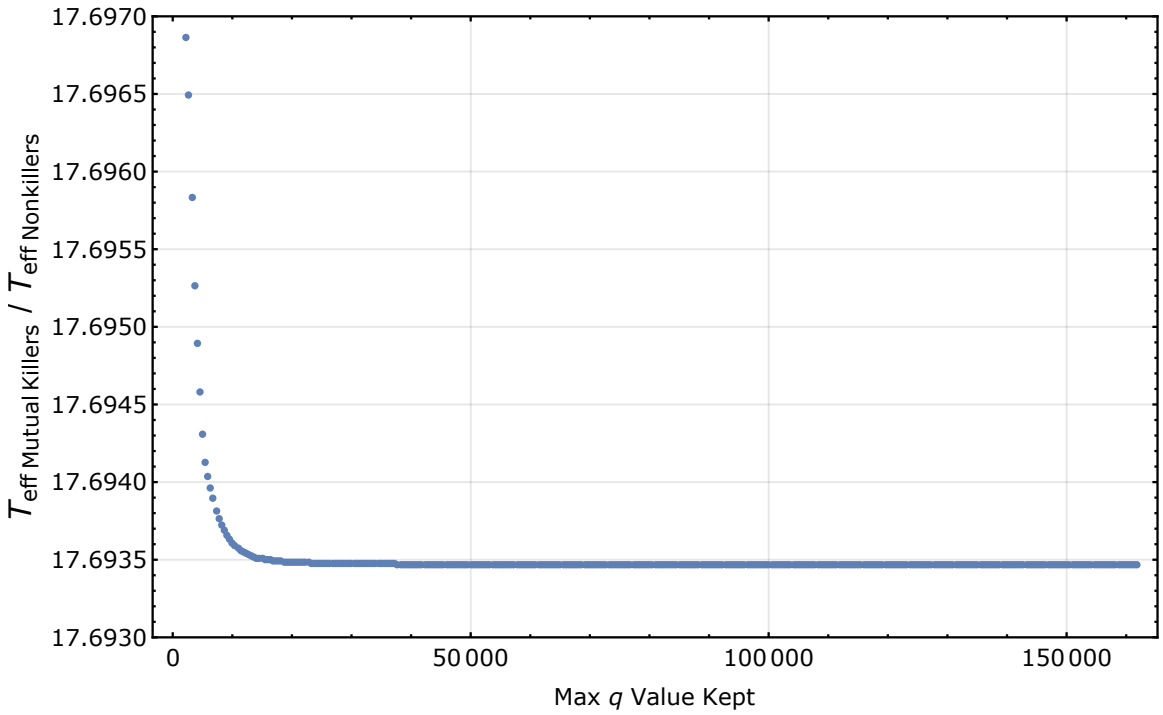

Figure 3.11 Regardless of the number of q values used in the calculation of effective temperatures, mutual killer biofilms always have a higher effective temperature than do nonkillers, and this ratio is stable regardless of how many q values we include. We chose to include 40 values of q—up to $\sim 1.77 \times 10^4$—as we wanted the maximum q value to be as low as possible while still providing stable T_{eff} measurements.

3.7.9 Observation of a potential q^{-4} downturn

The correlation function by *Risler, et al.* is, to leading order and in the $qH \ll 1$ regime, $C(q) = \frac{k_B T_{eff}}{\gamma q^2 + \kappa q^4}$. (For our biofilms, $H = 45.0 \pm 7.5\ \mu m$.) While we lack the necessary resolution to confidently measure the q^4 regime, we do observe a downturn around $q \approx$

$5 \times 10^4\ m^{-1}$ (Fig. 3.12), which is the close to the value of q for which γq^2 and κq^4 are equal ($q \approx 2.6 \times 10^4\ m^{-1}$), despite the fact that this is no longer in the $qH \ll 1$ regime where this functional form is predicted to hold [13]. A simulation with high killing and a simulation with ten times less killing have $C(q)$ functions which roughly line up with the experimental data for mutual killers and nonkillers respectively. Extracted T_{eff} values for these simulations differ by a factor of ~10.6.

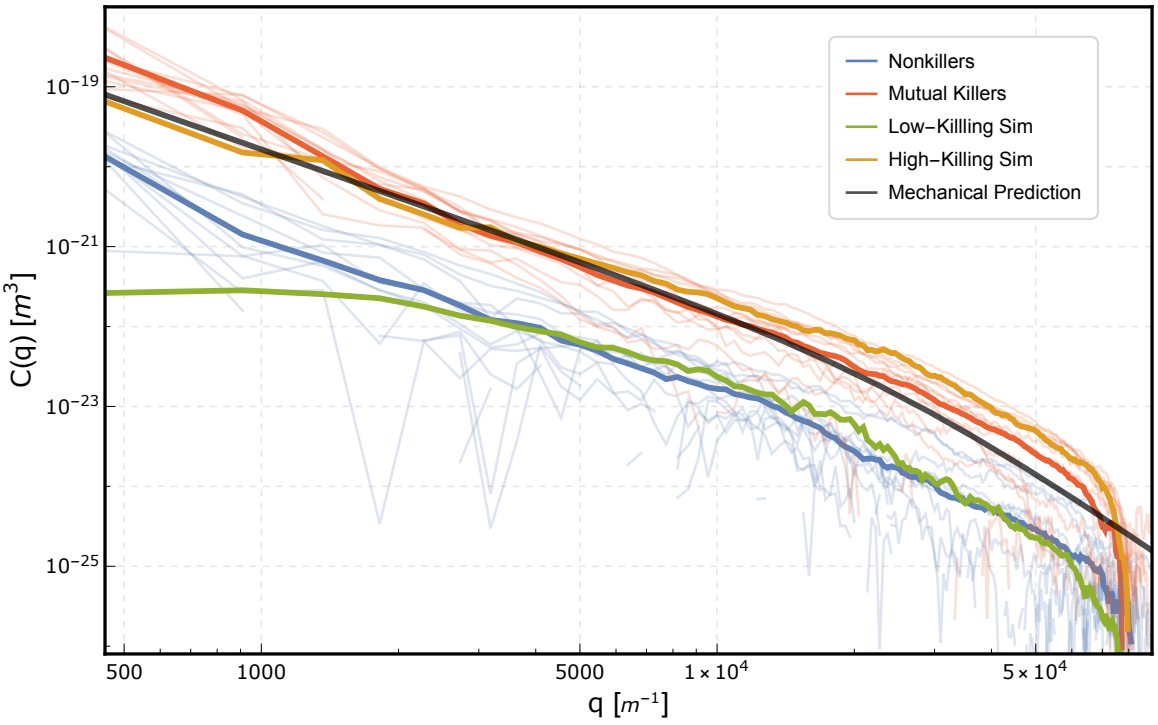

Figure 3.12 *C*(*q*) plotted vs. *q* for experimental data, simulations, and the independent mechanical prediction, including large *q* values.

3.7.10 On the necessity of high resolution

While white light interferometry was used for our measurements, it may be possible to perform similar measurements—at least between samples with large activity differences—with significantly lower out-of-plane resolution.

To explore the effect of decreased measurement resolution on the measured T_{eff}s, we took our raw topographic data (*i.e.*, before finding and subtracting the best ellipsoidal fits), then rounded them to several values, ranging from 1 nanometer to 1 micron. After this rounding was performed, we found and subtracted the new best ellipsoidal fits to arrive at resultant topographies representing what we *would* have obtained with lower experimental resolution. We then used these topographies to calculate T_{eff}s (in the same manner described in §3.7.8) for all colonies at each rounding level.

Surprisingly, the overall distribution is largely unaffected by this rounding, as seen in Fig. 3.13. p-values comparing the unrounded T_{eff} distribution to the various rounded distributions only drop below $.99$ (to $.94$) once data are rounded to $.5\ \mu m$, and even rounding to $1\ \mu m$ results in a p-value of $.35$.

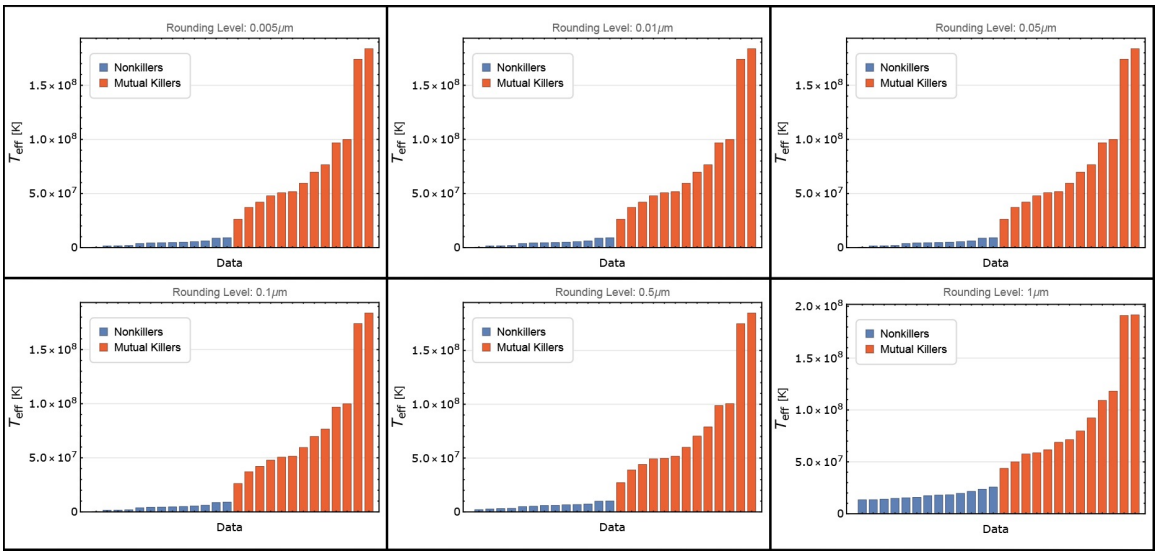

Figure 3.13 A comparison of rounded T_{eff} distributions to unrounded data shows that even rounding the topographic data to 1 micron does not impede the comparison of high activity samples to low activity samples. However, the dynamic range is largely

compressed, and the ability to accurately compare between individual samples is severely compromised.

However, if one looks only at the nonkiller colonies, it is obvious that the dynamic range becomes more and more compressed as a function of rounding level—by the time we round to half a micron, the dynamic range has been compressed by a factor of 4.8, and by 1 micron, 12.2. When the activity rates are not massively different, lower resolution results in a significant loss of comparative power. Indeed, even over all 26 samples, the loss of resolution in the low-T_{eff} samples results in a compression of the dynamic range by a factor of nearly 34.

3.7.11 Simulation setup

We have developed extensive individual-based simulations to support and expand upon our experimental results. These simulations allow us to independently tune experimentally inaccessible parameters, such as killing rate, as well as to directly investigate dynamics at the single-cell level.

Briefly, the biofilm is represented as a collection of bacterial cells distributed in either a three- or two-dimensional continuous domain. The state of the biofilm is fully characterized by the center positions of spheres (circles) that represent bacteria, and which may overlap. The following processes are simulated:

Motion: Overlapping cells are treated as being in contact, and as such experience a repulsive force linear in the extent of overlap. The spring constant used is roughly in agreement with literature values taken from AFM measurements (see [150]) The

overdamped limit is taken when considering a cell's motion: $\gamma \frac{\partial \vec{r_i}}{\partial t} = \vec{F_i}$ for the i^{th} cell, where $\gamma = 6\pi\eta R_i$with $R_i = 1\mu m$ and $\eta = 8.90 \times 10^{-4}\ Pa\ s$ (water). Cell positions are updated using forward Euler integration.

Growth: Cells grow at a constant volume (area) per time. After a reproduction event the mother cell's volume (area) resets to its initial value.

Reproduction: Cells reproduce with a probability that increases linearly in the amount of time elapsed since reaching a radius of $R_i(t) \geq R_i(0)$. A daughter cell's center position is seeded at a random point on the surface (perimeter) of the mother cell. The time scale is set by the expected time to reproduce (about 20 minutes for *V. cholerae*).

T6SS killing and random death: Cells are removed from the biofilm by random death with a probability that is constant in time. To simulate T6SS killing, two different bacterial strains (visualized as having different colors, *cf.* Fig. 3.3c) with different T6SS effectors are introduced. A cell is removed from the biofilm due to T6SS killing with a probability that is linear in the number of "enemy" cells within a $2R_i$ radius neighborhood of itself.

All other cellular processes such as secretion of biofilm are left out of the simulation, so the entire biofilm structure is due to change in constituent number and mechanical interactions of cells. With this biologically minimal framework, we recapitulate the fluidization of biofilms and the behavior of the height correlation predicted by [13], and measured in our biofilms.

All simulations were written and implemented in Processing, a free and open source programming language and integrated development environment built on Java.

3.7.12 Simulation of cellular reproduction

We simulated reproduction through two different strategies. In the first, any cell in the system is free to reproduce once it has grown large enough. This approach was utilized in all simulations reported in the main text, except for the tracer bead simulations. While this approach is not identical to reproduction in biofilms, it was chosen to demonstrate that a minimal model reproduces experimentally observed phenomenon. However, the tracer bead simulations were performed to inform the experiments, and thus needed to better replicate specific biofilm behavior. In the tracer bead simulations, we only allowed reproduction to occur for cells with the 5% smallest z-positions. This replicates the behavior of real biofilms on agar surfaces, for which reproduction occurs more near the agar surface where the nutrient concentration is the highest. This also speeds up the rate at which tracer beads approach the top surface of the biofilm. However, limiting reproduction to the bottom layer does not qualitatively change the other simulation results (e.g., Fig. 3.13).

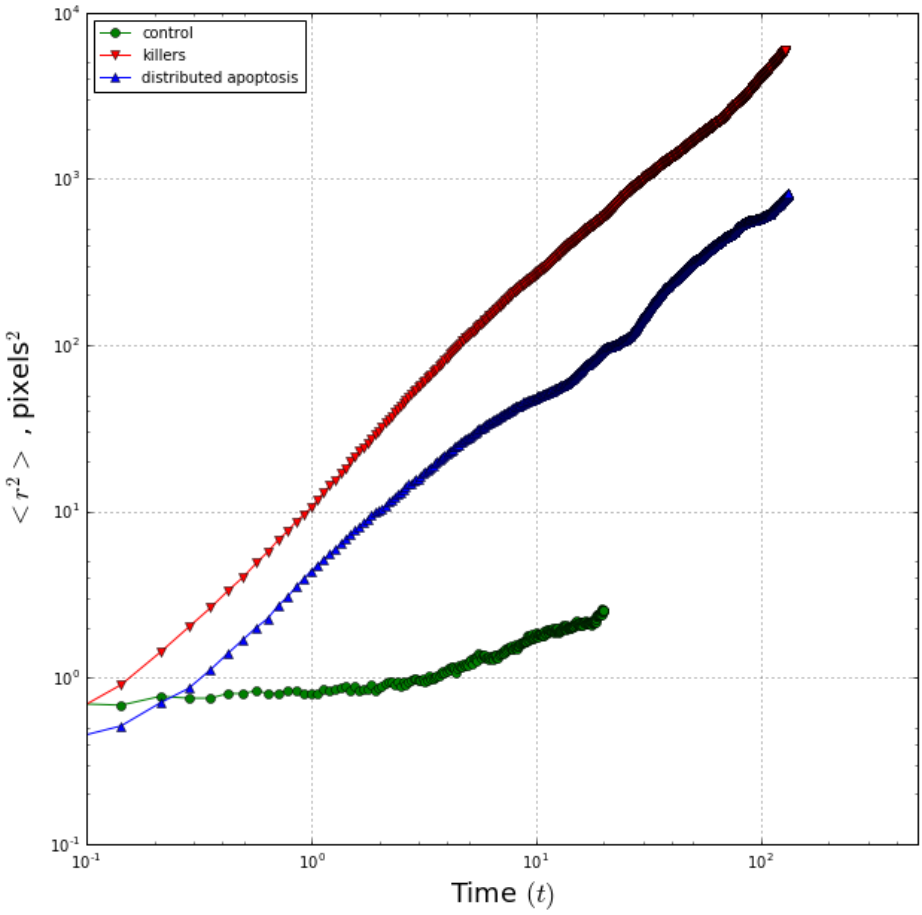

Figure 3.14 A log-log plot of the mean-squared displacement (measured in cell diameters^2) of cells in simulated biofilms wherein reproduction only occurs in cells that have the 5% smallest z-positions. Simulations were performed with no death, with only random death (*cf.* nonkiller biofilms), and with both random death and killing (*cf.* mutual killer biofilms). The addition of intercellular killing significantly fluidizes the biofilm.

3.7.13 Tracer bead tracking

Tracer beads (1 μm diameter, Dragon Green, Bangs Labs) were mixed into the inocula at a ratio of 3: 1 by volume. The initial volume fraction of the suspension of tracer

beads was $\sim 1667\ beads/\mu L$, leading to an average of 1250 beads per biofilm. We then take confocal z-stacks of the top $15\ \mu m$ of the biofilm, with a spacing of $1\ \mu m$ between z-slices. The same layer, $5\ \mu m$ below the surface of the biofilm, is shown in Fig. 3.15 at 13 and 26 hours, showing that beads move upward against gravity in a convective fashion.

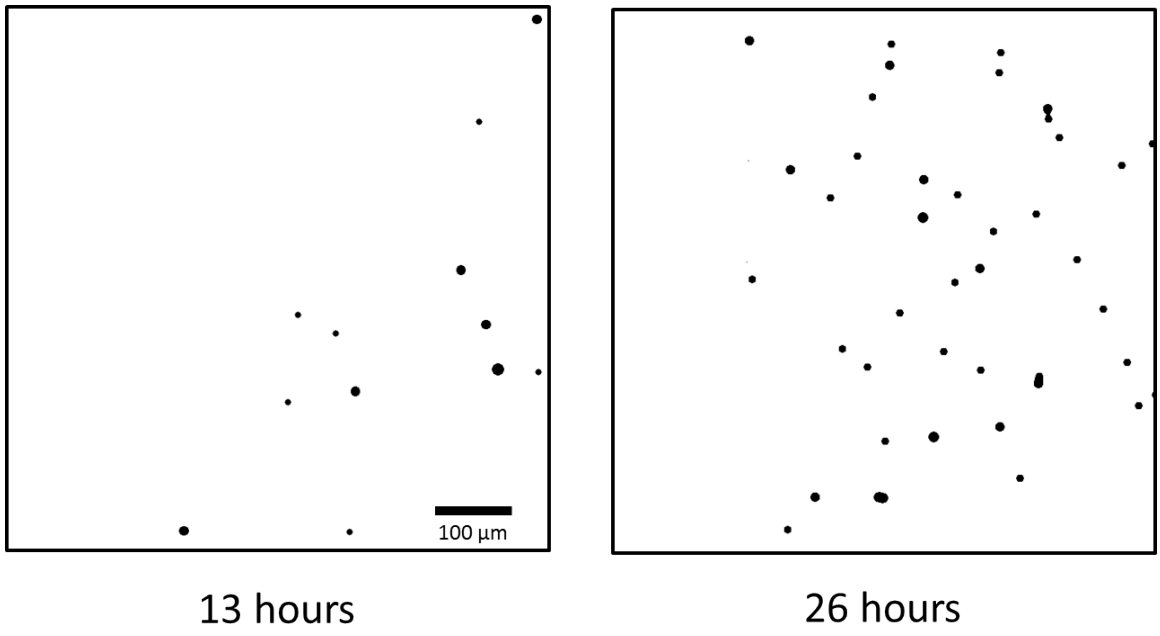

Figure 3.15 The beads observed $5\ \mu m$ beneath the surface of a mutual killer biofilm are shown at 13 hours (left) and 26 hours (right). While our particle counts are measured directly from these images, to display a large field of view, with many particles, a Gaussian blur with a radius of $4\ \mu m$ was applied.

CHAPTER 4. VISCOSITY-INDEPENDENT DIFFUSION MEDIATED BY REPRODUCTION AND DEATH IN BIOFILMS

(This work is under revision with Phys. Rev. Lett. [34])

4.1 Introduction

Bacterial biofilms, surface-attached communities of cells, are in some respects similar to colloidal solids; both are densely packed with non-zero yield stresses. However, unlike non-living materials, bacteria reproduce and die, breaking mechanical equilibrium and inducing collective dynamic responses. We report experiments and theory investigating the motion of immotile *Vibrio cholerae*, which can kill each other and reproduce in biofilms. We vary viscosity by using bacterial variants that secrete different amounts of extracellular matrix polymers, but are otherwise identical. Unlike thermally-driven diffusion, in which diffusivity decreases with increased viscosity, we find that cellular motion mediated by death and reproduction is independent of viscosity over timescales relevant to bacterial reproduction. To understand this surprising result, we use two separate modeling approaches. First, we perform explicitly mechanical simulations of one-dimensional chains of Voigt-Kelvin elements that can die and reproduce. Next, we perform an independent statistical approach, modeling Brownian motion with the classic Langevin equation under an effective temperature that depends on cellular division rate. The diffusion of cells in both approaches agrees quite well, supporting a kinetic interpretation for the effective temperature used here and developed in previous work. As the viscoelastic behavior of biofilms is believed to play a large role in their anomalous

biological properties, such as antibiotic resistance, the independence of cellular diffusive motion — important for biofilm growth and remodeling — on viscoelastic properties likely holds ecological, medical, and industrial relevance.

Bacteria can grow in planktonic suspension or within biofilms [20]. These surface-attached bacterial communities are similar to colloidal solids in many respects [25], [28]. Both are soft solids composed of densely-packed micron-sized objects. Biofilms even exhibit glassy phases, much like their colloidal counterparts [13], [14], [16]. However, unlike particles, bacteria reproduce and die; thus, even immotile bacteria that cannot swim are fundamentally active. Theory and experiments suggest that reproduction and death break mechanical equilibrium, driving fluctuations in cell motion and fluidizing biofilms [13], [14], [16], [19]. This active intra-biofilm diffusion occurs at high density, and within a highly viscoelastic material. The fluidization of biofilms and diffusion of cells via reproduction and death, therefore, is qualitatively unlike that experienced by thermal, non-living particles.

Our understanding of thermal diffusion—and specifically the Stokes-Einstein relation—arises from a physical coincidence: the thermostatic collisions with solvent molecules driving Brownian motion are also responsible for viscous damping [43]. The fluctuation-dissipation relation then tells us that the force spectrum is determined by the friction spectrum; as a result, diffusivity is inversely proportional to viscosity. Conversely, diffusion from death and reproduction in dense biofilms is driven by local strain fields arising from either cellular reproduction or death and lysis, and biofilm viscosity is largely

driven by secreted extracellular matrix-forming polymers [129], [151]–[155]. Viscous and driving forces thus arise from completely separate sources in biofilms; how, then, is diffusion from cellular reproduction and death affected by viscosity?

4.2 Methods

Here, we measure the motion of cells in *Vibrio cholerae* biofilms containing two variants that are genetically identical ("isogenic"), other than the genes responsible for encoding different Type VI Secretion System ("T6SS") toxins. The T6SS is a contact-dependent toxin delivery system which allows these two otherwise-isogenic variants to kill each other when cells are in contact with one another. Genetically, we also vary whether the cells do or do not secrete extracellular matrix-forming polymers ("Matrix+" and "Matrix-", respectively). We find that Matrix+ biofilms have a viscosity three times larger than that of Matrix- biofilms. Surprisingly, we find that despite a large difference in viscosity, Matrix+ and Matrix- biofilms exhibit similar diffusivities.

We approach this problem with three complementary techniques. First, we track the motion of tracer beads embedded in biofilms with high and low viscosities via confocal microscopy. While tracking beads allows us to directly observe biofilm dynamics, beads only follow cellular motion in Matrix- biofilms; in Matrix+ biofilms bead dynamics deviate from cellular dynamics. To gain additional information about the average behavior of all cells, we use a previously validated method to extract this information from biofilm topography and independent mechanical measurements. Briefly, *Risler, et al.*, developed a theory of homeostatic cellular films with reproduction and death, and predicted that an effective fluctuation-response relationship mediated by these opposing activities produces

measurable effects on topography [13]. This prediction was experimentally validated in *Kalziqi, et al.* [33]. Here, we combine topographic measurements with the generalized Stokes-Einstein relation to extract mean diffusivities. Finally, we model death and reproduction in biofilms with a series of Voigt-Kelvin dashpot-spring elements, and show through simulations and theory how viscosity impacts diffusion in such a system.

To explore the effect of the extracellular matrix on the motion and diffusion of cells within biofilms, we inoculated and incubated biofilms as described in [33]. To grow biofilms containing isogenic mutual killers, we mixed (at a ratio of 1:1.4) two derivatives of a constitutive killer of C6706 *V. cholerae* that are each genetically modified to use a different T6SS toxin from *V. cholerae* strain 692-79 [30], [31], [33]. The mutual killing strains were also modified to express two different fluorescent proteins. Matrix- variants were genetically modified to produce no extracellular matrix [156], whereas Matrix+ variants are wild type for extracellular matrix secretion (*i.e.* they produce a "natural" amount of matrix product) [32]. All biofilms were grown by mixing two mutually-killing strains of *V. cholerae* and placing a $1\,\mu L$ inoculum (roughly 8×10^5 cells) onto a lysogeny broth agar plate at 37˚C.

4.3 Experimental results

First, we measured biofilm viscosity in the low-frequency limit via creep tests (see SI for more information) [17], [157], [158]. Matrix+ biofilms had an average viscosity of $43 \pm 5.1\ kPa\,s$ (mean ± standard deviation), just over three times higher than that of Matrix- biofilms ($14 \pm 6.2\ kPa\,s$) (Fig. 4.1a), demonstrating that the presence of an extracellular matrix substantially modifies biofilm viscosity.

As a check on the impact of extracellular matrix secretion on killing dynamics, we sought to measure the amount of killing that occurs in each type of biofilm. To do so, we first determined whether Matrix+/- biofilms have different levels of activity by examining the typical domain size of clonal patches. It was previously demonstrated that mutual killing bacteria undergo 'Model A' coarsening in biofilms [32]; consequently, the size of clonal domains is related to the number of killing events. To measure the size of clonal domains, mutually-killing strains were incubated for 24 hours, and then visualized with fluorescence microscopy. As observed prior [33], well-mixed, Matrix- mutual killers, which do not produce viscous extracellular matrix-forming polymers, separate to create a coarsened structure (Matrix-, Fig. 4.1b and c). Likewise, well-mixed Matrix+ mutual killers, which produce viscous extracellular matrix-forming polymers, exhibited similarly-sized clonal domains (Matrix+, Fig. 4.1b and c). Thus, the amount of killing that occurred was not significantly altered by the presence or absence of matrix material.

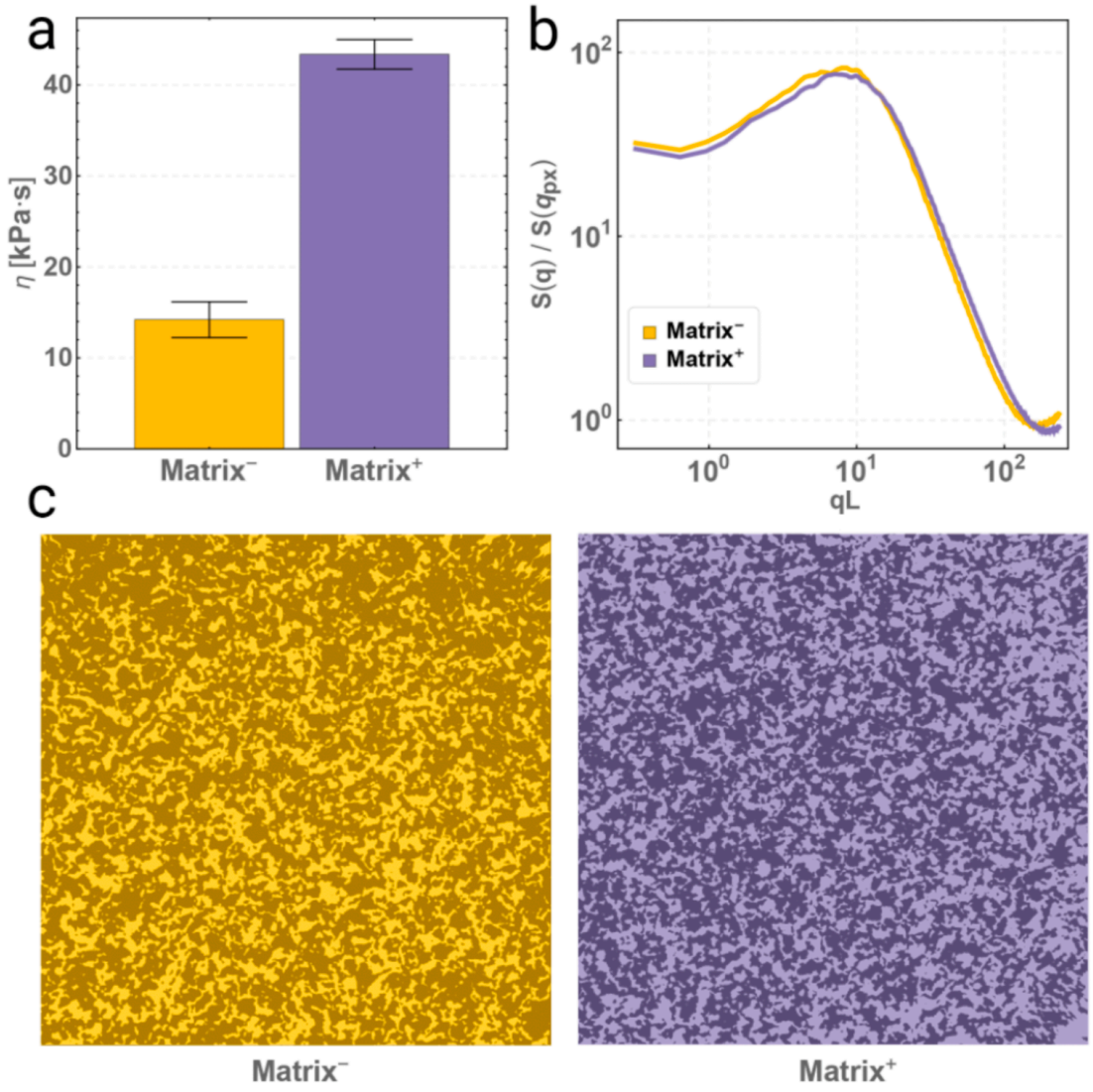

Figure 4.1 **a. Directly measured viscosities for Matrix- and Matrix+ biofilms, shown with standard error. The presence of extracellular matrix products increases the viscosity by roughly a factor of 3. b. Mean structure factors for Matrix- and Matrix+ biofilms show that the clonal size distribution is practically unaffected by the presence of the extracellular matrix, and thus the amount of killing is also unaffected. c. Selected examples showing highly comparable strain-strain coarsening for Matrix- and Matrix+ biofilms.**

We next directly observed the motion of tracer beads in biofilms. 1-micron diameter polystyrene beads (FSFR004 Flash Red, Bangs Labs) were mixed with liquid culture immediately before the biofilm was inoculated. Beads were imaged every 3 minutes during 4.5 hours of growth with a Nikon A1R confocal microscope. It was previously shown that beads convect toward the top of growing biofilms at the agar-air interface [33]; thus, we measured the in-plane mean square displacement (MSD) (*i.e.*, their mean square displacement parallel to the agar surface). In Matrix- biofilms, we found that tracer beads are highly mobile (Fig. 4.2a), exhibiting caged-like dynamics on short lag times, and diffusive-like dynamics over longer lag times. We extract diffusion coefficients from the mean-squared displacement: Matrix- biofilms have a mean diffusivity of $0.63 \pm 0.17 \times 10^{-3}\ \mu m^2 s^{-1}$. However, while they still exhibited diffusive dynamics, we found that beads did not effectively follow cellular dynamics in Matrix+ biofilms, likely due to their interactions with the extracellular matrix itself [153] (see §4.6.2 for additional information). Further, tracer beads are limited in the information they can provide about biofilm dynamics: tracer beads only probe their local neighborhoods, they convect away from the source of nutrients [33], and it is unclear how the beads themselves may impact biofilm mechanics locally. Thus, while the motion of tracer beads strongly implies that immotile cells within a biofilm undergo significant, diffusive displacement due to reproduction and death, their inherent limitations motivate a new approach to measuring diffusivities that can capture the unperturbed dynamics of all cells.

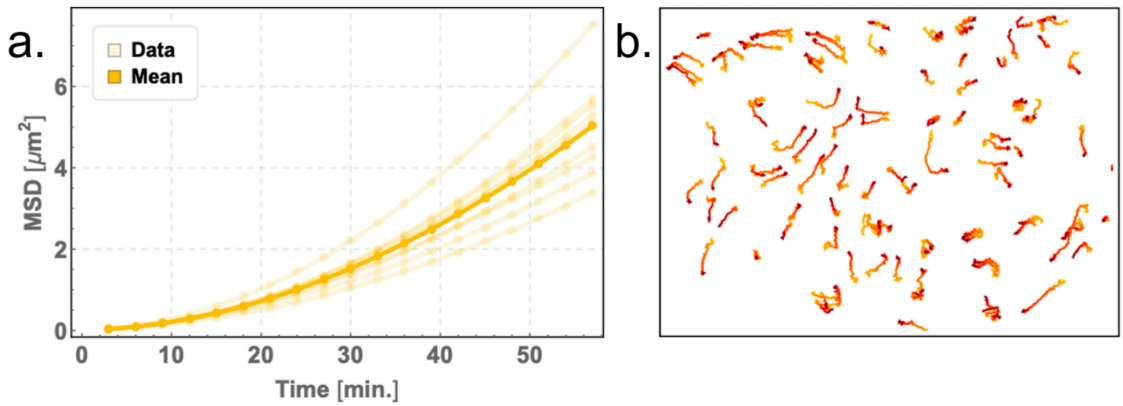

Figure 4.2 a. Measured lateral MSD for tracer beads inside a Matrix- biofilm. Light lines represent data from individual measurements; the dark line represents the average MSD. b. Tracks of individual tracer beads colored by timepoint, demonstrating diffusive behavior.

To do this, we turn to a previously-validated interferometry technique. In a recent paper [33], we demonstrated that information about death and reproduction could be extracted from high resolution measurements of a biofilm topography when coupled with mechanical measurements. That work built on previous theoretical results in which a Maxwell model of a tissue obeys an effective fluctuation-response relationship, permitting the calculation of integrated death and reproduction rates via an effective temperature (T_{eff}) in the low-frequency, long-wavelength limit [13]. This relationship was tested experimentally in [16] using Matrix- *V. cholerae* biofilms; biofilms composed of mutual killing bacteria have T_{eff} that are ~18 times larger than those of biofilms composed of cells that cannot kill ($p = 1.75 \times 10^{-4}$) [33].

After 24 hours of incubation at 37˚C, the surface height profile was measured–with O(nm) precision using a ZYGO NewView 8300 interferometer–for 17 Matrix+ and 13 Matrix- biofilms. All measured biofilms are shaped like spherical caps with a central concave ellipsoidal dimple, often called the "homeland" [158]. Each biofilm topography is a superposition of such an ellipsoidal background and fluctuations due to cell-cell interactions. We fit and subtract an ellipsoidal background to each biofilm to obtain a fluctuation-topography in the vein of Ref. [13], where the topography is determined by internal activity rather than initial and external conditions (Fig. 4.3a). To relate topographies to effective temperatures (as in [13] and [33]), we must measure biofilm membrane tension and bending rigidity, which we did for Matrix+/- phenotypes (see §4.6.1).

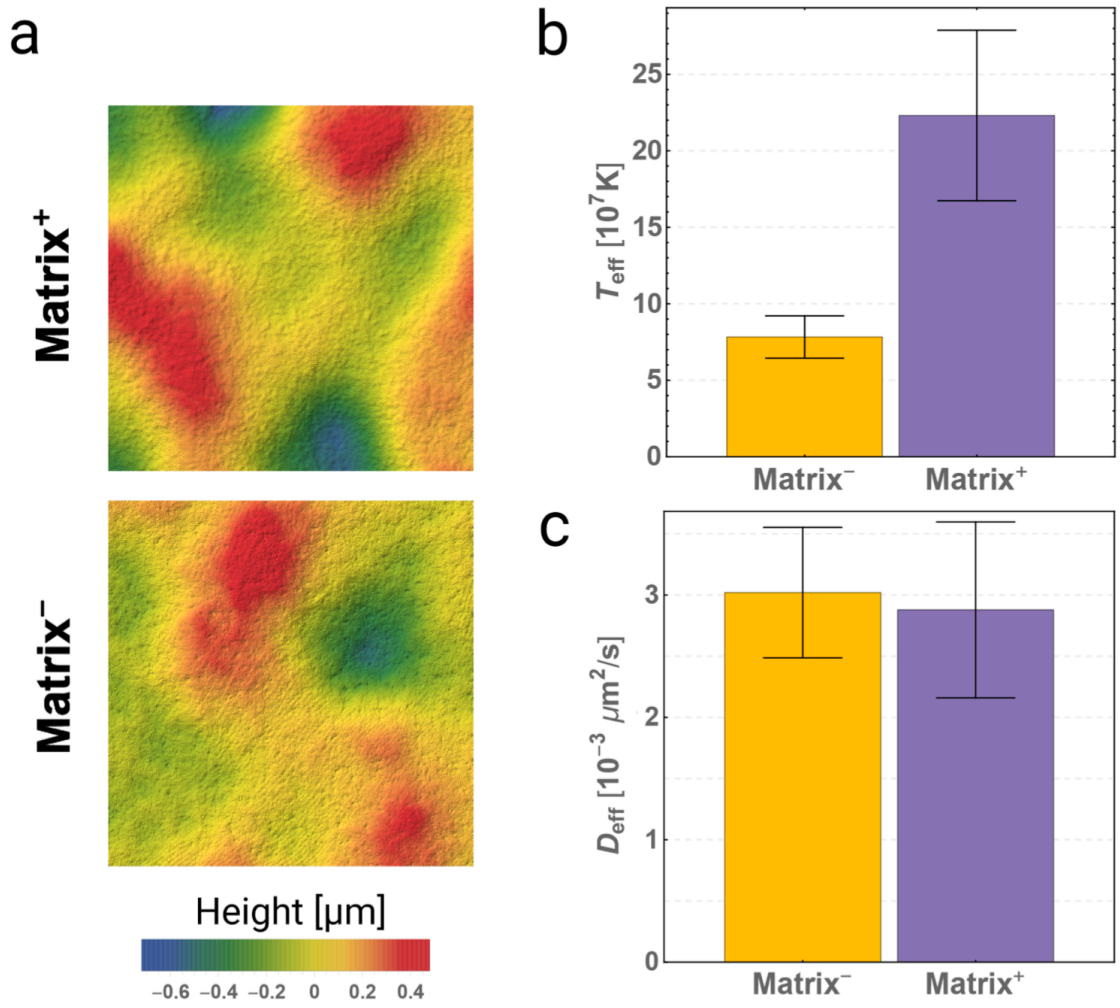

Figure 4.3 a. Demonstrative surface topographies of Matrix- and Matrix+ biofilm homelands measured via interferometry. b. While the topographies appear quite similar by eye, extracted effective temperatures (shown with standard error) are significantly different across many samples. c. However, diffusion constants calculated using the aforementioned effective temperatures and viscosities are nearly identical between Matrix- and Matrix+ samples.

While Matrix+ and Matrix- biofilm topographies look superficially rough (Fig. 4.3a) [159], [160], these measurements reveal that Matrix+ biofilms have significantly larger

effective temperatures than Matrix- biofilms ($p < 0.004$, Fig. 3b). We then convert measured effective temperatures into effective diffusivities, D_{eff}, using the generalized Stokes-Einstein relation in the low-frequency limit (and independently-measured viscosities; see supplemental information for more details) (Fig. 4.3c) [161]. While the effective temperature distributions are different depending on the presence of extracellular matrix, the distributions of effective diffusivities are very nearly identical ($p > 0.5$). The extracted mean is $D_{eff} = 3.0 \pm 1.9 \times 10^{-3}\ \mu m^2 s^{-1}$ and $D_{eff} = 2.9 \pm 3.0 \times 10^{-3}\ \mu m^2 s^{-1}$, for Matrix- and Matrix+ biofilms, respectively, each of which is reasonably close to the mean diffusivity extracted from Matrix- tracer bead experiments $D = 0.63 \pm 0.17 \times 10^{-3}\ \mu m^2 s^{-1}$. This agreement further supports the argument that biofilm topography directly relates to its underlying dynamics and mechanics.

4.4 Simulations and predictions

To test this result, and gain insight into its universality, we perform event-driven, individual-based simulations of mutual killer cells in one-dimension. To capture the viscoelastic character of biofilms, we model them as chains of cells coupled by Voigt-Kelvin elements. Reproduction and death are assumed to be Poisson processes with activity rate λ_{act} (Fig. 4.4a); the time-step between events is chosen from an exponential distribution $dt \sim e^{-\lambda_{act} t}$. Each event corresponds, with equal probability, to the step-strain resultant from reproduction or death of a cell at a random position in the biofilm, and as such imposes a step stress $\pm\sigma_0$ felt instantaneously throughout the biofilm. Finally, after each event the velocities and positions of all the cells are updated according to the current

state of stress in the biofilm and the constitutive equations $\sigma(t) = E\varepsilon(t) + \eta\, d\varepsilon(t)$, using backward-Euler dt integration, where E is the elastic modulus, η is viscosity and ε is strain.

The diffusion of cells in these simulations aligns well with the predictions of a simple modification to the classic Langevin equation model for the Brownian motion of a particle: $m\frac{dv}{dt} = -m\gamma v + R(t)$. Here, γ is the inverse time scale associated with Stokes drag, $R(t)$ is a white noise term with zero mean and strength given by $\langle R(t)R(t+\tau)\rangle = 2m\gamma k_B T_{eff}\delta(\tau)$, with $k_B T_{eff} = U_0\lambda_{act}/\gamma$, where λ_{act} is the driving force activity rate, and U_0 is the energy scale of the driving force. When λ_{act} is identified with the inverse time-scale associated with viscous damping (γ) and the energy scale is set to $U_0 = k_B T$, then the ordinary form of viscosity-dependent Brownian motion is recovered. On the other hand, when γ is set to the viscoelastic relaxation rate (E/η), and the energy scale is associated with cellular motion $U_0 = m\left(d\frac{\sigma_0}{\eta}\right)^2$, where d is the cellular diameter, we find that this Langevin equation agrees numerically with our simulations, and predicts diffusion to be independent of viscosity in the long-time limit (Fig. 4.4c).

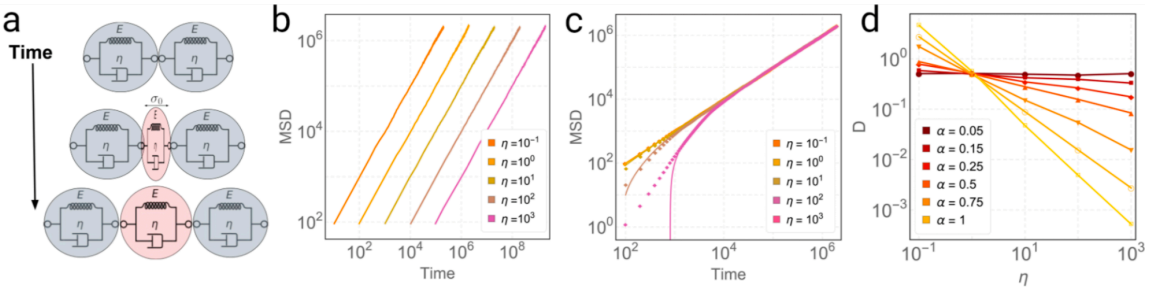

Figure 4.4 a. A visualization of the simulation setup. Cells are separated by Voigt-Kelvin elements and begin reproducing and lysing. Reproduction applies a stress σ_0 to neighboring cells. b. MSDs from simulations where $\alpha = 1$ (standard diffusion). c.

MSDs from simulations where $\alpha = 0$ (free diffusion). The solid black line corresponds to an independent analytical prediction based on a generalized Langevin equation approach. d. Extracted diffusion constants as a function of viscosity from simulations with different values of α.

To further compare the simulations and theory, we set the simulated cellular reproduction and death rate to be a function of E and η: $\lambda_{act} = \lambda_0 \left(\frac{E}{\eta}\right)^{\alpha}$ for a value of α between 0 (λ_{act} is totally independent of viscosity—similar to actual bacterial reproduction rates) and 1 (λ_{act} has the traditional dependence on viscosity). Theory predicts that $D \propto -\alpha$; indeed, this is observed in simulations for several values of α (Fig. 4.4d).

It is worth noting how surprising it is to recover the theoretically expected scaling between D and α in simulations. The simulation is a viscoelastic mechanical model in which the only ingredients are death, reproduction and mechanical properties, and makes no explicit mention of effective temperatures or relaxation rates. Therein, we find that the mechanical properties play no role in how cells move around in the long-time limit, *i.e.* how the diffusion constant scales, unless the rate of division and death is a function of those mechanical properties. And if the rate of division is set to be a function of mechanical properties, then the behavior of the diffusion constant in simulations is exactly as predicted by a theory that makes no explicit mention of viscoelasticity, mechanical properties, cell death, or cell reproduction. These represent two totally different approaches—mechanical and statistical—that yield the same result when translated into each other's language. This observation offers more evidence that the effective temperature is not simply a thermodynamic analogue but actually relates to kinetics and the mechanical energy of

particles, the same way ordinary temperature does [13], [14]. Thus, viscosity independent diffusion appears to be a natural consequence when the driving force and viscous damping arise from separate physical processes with different time scales.

Interestingly, the Langevin equation approach also predicts a diffusion constant of $D = \frac{1}{2}\lambda_{act}\ell^2$. Here λ_{act} is the rate of lysis and reproduction, and ℓ is a characteristic length scale. A typical cell division rate for C6706 *V. cholerae* is ~20 minutes, so in the homeostatic limit the event rate can be roughly approximated as $\frac{1\ event}{10\ minutes}$. A typical cell length is about $1.0\ \mu m$, so putting together a "back of the envelope" prediction we find $D \approx 1.5 \times 10^{-3}\ \mu m^2 s^{-1}$, on the same order of magnitude as effective diffusivities extracted from both colony topographies and from tracer beads in Matrix- biofilms.

4.5 Conclusions

Through experiments, simulations, and theory, we show that diffusion mediated by death and reproduction is independent of viscosity. This surprising result arises from the separation of the origin of viscous relaxation and driving force time scales. Reproduction and death events induce step-strains that, in turn, induce stresses. These stresses relax much more rapidly than the time between step-strain events, making the material essentially a memory-less fluid on long time scales. The accumulated motion that a cell undergoes as a result of these strains amounts to a random walk governed entirely by the active driving force.

The results presented in this manuscript are likely of broad relevance. Biofilms that form in nature are typically polymicrobial, even featuring different taxa and species.

Accordingly, bacteria have evolved many mechanisms for killing their competitors [162], so this class of cellular diffusion is likely to be very common. Further, the mechanical properties of biofilms are critical for many other biological properties [10], [28], [129], [131]; the independence of cellular diffusive motion—important for biofilm growth and remodeling—on biofilm mechanics suggests that biofilm viscoelasticity can vary without incurring a trade-off with regards to cellular diffusion.

4.6 Supplemental materials

4.6.1 Other mechanical measurements

We performed independent mechanical measurements [17], [33], and found that the Young's moduli were $14.8 \pm .8\, kPa$ and $3.1 \pm 1.3\, kPa$ for Matrix+ and Matrix- biofilms respectively. We found that the Matrix+ biofilms had an average surface tension of $0.089 \pm 0.001\, N/m$, as compared to Matrix- biofilms' average of $0.023 \pm 0.004\, N/m$, and bending rigidities of $2.5 \pm 0.20 \times 10^{-9}\, Nm$ (Matrix+) *vs.* $3.4 \pm 0.45 \times 10^{-11} Nm$ (Matrix-).

4.6.2 Tracer beads in Matrix+ biofilms

In addition to Matrix- biofilms, we have extracted diffusion coefficients from tracer beads embedded in Matrix+ biofilms. We observed that the MSD in Matrix+ biofilms also exhibits a caged-like plateau at short times, followed by diffusive-like linear regime at long lag times (Fig. 4.5a). However, the variation in motion from sample-to-sample was higher in Matrix+ biofilms than Matrix- biofilms. We found that the diffusion coefficient was $0.16 \pm 0.11 \times 10^{-3} \mu m^2 s^{-1}$, smaller than that in Matrix- biofilms ($p = 4 \times 10^{-4}$).

To determine if the presence of extracellular matrix prevents tracer beads from accurately mimicking the motion of cells, we need to compare the motion of cells and tracer beads. To measure the motion of individual cells, we analyzed the dynamics at early times during biofilm formation, i.e., these experiments started with 14% of the agar surface covered with cells (and 1% of the surface covered with beads), and continued until a dense bacterial monolayer formed. We measured the average displacement of the beads and the cells over time with time steps of 3 *min*. At very low densities, the beads behave similarly in Matrix+ and Matrix- biofilms (Fig. 4.5b). However, after about 30 min, which corresponds to about 40% of the surface covered with cells, the average displacements start to differ. Beads in Matrix- biofilms move faster, which is consistent with the difference in the diffusion coefficients extracted from tracer bead MSDs. Next, we analyzed the average displacement of cells using particle image velocimetry (PIV) during the same time span. We found that motion of cells in Matrix+ and Matrix- biofilms is not significantly during this time span (Fig. 4.5c). This clearly contrasts with the behavior of beads shown in Fig. 4.5b. In Matrix- biofilms, the displacement of beads and cells is similar at later times (beyond 40 min). We can conclude that the presence of extracellular matrix impacts the motion of tracer beads, as previously demonstrated [153]. Thus, tracer beads do not accurately mimic the motion of cells in Matrix+ biofilms.

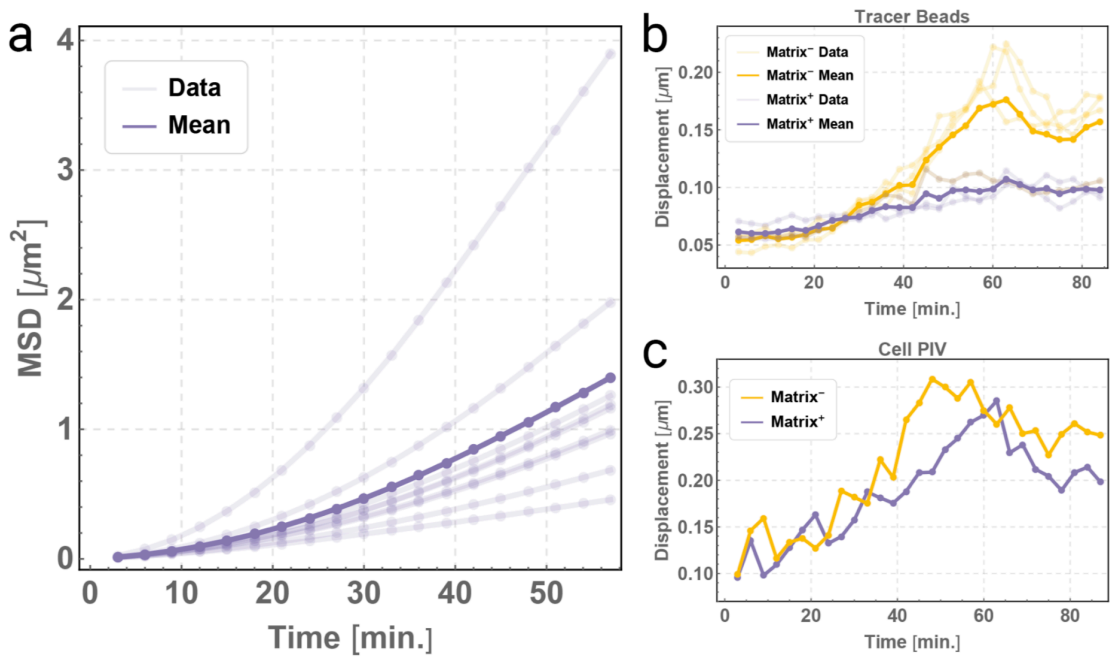

Figure 4.5 a. Measured lateral MSD for tracer beads inside a Matrix+ biofilm. Light lines represent data from individual measurements; the dark line represents the average MSD. b. The displacement of the beads at early times during biofilm formation in Matrix- and Matrix+ biofilms shows that there is a strong divergence in bead motion after about 40 minutes of growth. c. However, using PIV to track individual cells in Matrix- and Matrix+ biofilms shows no such discrepancy, suggesting that the presence of an extracellular matrix prevents tracer beads from accurately tracing cellular motion.

4.6.3 Langevin equation

4.6.3.1 Effective temperature and related work

As discussed in the main text, others have studied cell migratory behavior due to death and reproduction, and have used an effective temperature formulation to recover

fluctuation-dissipation like behavior. In particular, we build on the work of *Ranft, et al.*, [14] and *Risler, et al.*, [13]. We use an effective temperature which agrees with theirs to leading order, but in this section we rewrite it in a different form for convenience. *Ranft, et al.*, report an effective temperature that scales as:

$$k_B T_{eff} \propto \frac{\lambda_{act}\eta}{\rho}, \quad (1)$$

with the cellular activity rate λ_{act}, the effective viscosity η, and the cell number density ρ. Note that to our knowledge, previous work has focused on elastic cells that develop an effective viscosity due to the fluidization effect of activity. Here, we'll be using, as η, the measured viscosity of biofilms. Viscosity is nothing more than a material's energy density multiplied by a timescale associated with structural rearrangements [163]. We can write $\eta = \frac{u}{V}\frac{1}{\gamma}$, for an energy u, a volume of material V, and a relaxation rate γ. Next, we can write the inverse cellular number density as $\frac{1}{\rho} = \frac{V}{N}$ for N cells. Combining these terms in equation (1), we have:

$$k_B T_{eff} = \frac{\lambda_{act}}{\gamma}\frac{u}{N}$$

$$k_B T_{eff} = \langle E_{const} \rangle \frac{\lambda_{act}}{\gamma} \quad (2)$$

Squaring, taking the average over many solutions (*i.e.* for many realizations of the stochastic function ξ), and using the relation $\langle \xi(t)\xi(t+\tau) \rangle = \frac{2\gamma k_B T_{eff}}{m}\delta(\tau)$ yields (after much rearranging):

$$\langle v^2 \rangle = \frac{k_B T_{eff}}{m}(1 - e^{-2\gamma t}) \text{ (3)}$$

$$\langle x^2 \rangle = \frac{k_B T_{eff}}{2m\gamma^2}(2\gamma t - 3 + 4e^{-\gamma t} - 2e^{-2\gamma t}) \text{ (4)}$$

In the long-time limit, this becomes

$$\langle v^2 \rangle = \frac{k_B T_{eff}}{m} [i.e. \text{ Equipartition}] \text{ (5)}$$

$$\langle x^2 \rangle = \frac{k_B T_{eff}}{m\gamma} t [i.e. \text{ Diffusion}] \text{ (6)}$$

4.6.3.2 Conventional diffusion and viscosity-independent diffusion

As discussed above, eq. (2) simplifies to $k_B T$ for a passive fluid at equilibrium; replacing $k_B T_{eff}$ with $k_B T$ in eq. (6) yields the expected result for passive, equilibrium systems. This is because we've set the timescale for damping equal to the timescale associated with thermal kicks—γ appears in the noise strength as well as in the damping term. Also, the energy of each constituent is again set by the strength of thermal kicks, thus ensuring equipartition holds.

On the other hand, when the timescales governing the source of constituent motion and damping of constituent motion are separated, Einstein's classic results no longer necessarily hold. In our case, when considering active, reproducing but immotile, constituents embedded in a viscoelastic medium, it is most natural to set the inverse damping timescale γ to the viscoelastic relaxation rate $\frac{E}{\eta}$. The energy scale, however, is

associated with cellular motions due to *active* kicks (*i.e.* step stresses from reproduction and death), and so we can write $\langle Econst \rangle = m\left(\frac{d\sigma_0}{\eta}\right)^2$, with cellular diameter d.

The reproduction/death rate is identified with the activity rate λ_{const}. We then have

$$\langle x^2 \rangle = \frac{k_B T_{eff}}{m\gamma} t$$

$$\langle x^2 \rangle = \frac{\langle E_{const} \rangle \lambda_{act}}{m\gamma^2} t$$

$$\langle x^2 \rangle = \frac{m\left(\frac{d\sigma_0}{\eta}\right)^2 \lambda_{act}}{m\left(\frac{E}{\eta}\right)^2} t$$

$$\langle x^2 \rangle = \left(\frac{d\sigma_0}{E}\right)^2 \lambda_{act} t$$

$$\langle x^2 \rangle = \ell^2 \lambda_{act} t$$

Here $\ell = d\,\sigma_0$ is the change in length that the spring in the Voigt-Kelvin element of length d would experience instantaneously if subjected to a force σ_0. In other words, we can think of it as the "step-size" in a discrete one-dimensional random walk, where steps are taken at a rate λ_{act}. The above is the long-time result. The equation we use to compare with simulations at all times applies this same process to eq. (4), producing:

$$\langle x(t)^2 \rangle = \frac{\lambda_{act}\ell^2}{2\gamma}(2\gamma t - 3 + 4e^{-\gamma t} - 2e^{-2^{-\gamma t}}). \quad (7)$$

4.6.4 Simulations

Biofilm simulations in which the reproduction and death rate is λact and the viscoelastic relaxation rate is $\gamma = \frac{E}{\eta}$ agree well with the predicted mean squared displacement from eq. (7).

As described in the main text, we performed event-driven, individual-based simulations of mutual killer cells in 1D. To capture the viscoelastic character of the biofilm, we model it as a chain of cells coupled by Voigt-Kelvin elements, with spring stiffness E and dashpot damping η. Reproduction and death are assumed to be Poisson processes with an activity rate λ_{act}; the time-step between events is chosen from an exponential distribution $dt \sim e^{-\lambda_{act} t}$. Each event corresponds, with equal probability, to the step-strain resultant from reproduction or death of a cell at a random position in the biofilm, and as such imposes a step stress σ_0 felt instantaneously throughout the biofilm. Finally, after each event the velocities and positions of all the cells are updated according to the current state of stress in the biofilm and the constitutive equations $\sigma(t) = E\varepsilon(t) + \eta \frac{d}{dt}\varepsilon(t)$, using backward-Euler integration. This leads to the discretization scheme:

$$\epsilon_t = \frac{1}{1 + dt\frac{E}{\eta}}(\epsilon_{t-1} + \frac{dt}{\eta}\sigma_t)$$

In fact, the simulation code is very short, so it is included inline here:

```
import numpy as npfrom matplotlib import pyplot as plt
### define constants (example values)
E = 1; eta = 1
T = 20000 #total number of time steps
lambda.act = 1e-2 #rate of birth/death events
```

```
N = 10000 #length of biofilm

sigma.0 = 10

### positions of events

j = np.random.randint(0,N,size=T)

###nature of events #(birth = 1, death = -1)

s = np.random.choice([-1,1], size=T)

###timing of events

dt = np.random.exponential(scale = 1/lambda act, size = T)

t = np.cumsum(dt)

sigma = np.zeros(shape=(T,N)) epsilon = np.zeros(shape=(T,N))

### run the simulation

for k in range(T):

      sigma[k,:j[k]] +=-sigma.0*s[k]

      sigma[k,j[k]:] += sigma.0*s[k]

      epsilon[k,:] = (1 / (1 + dt[k]*E/eta)) * (

            epsilon[k-1,:] + (dt[k]/eta)*sigma[k,:])

### plot results

plt.plot(t,np.average(epsilon**2,axis=1))
```

4.6.5 Physical explanation of Langevin modification

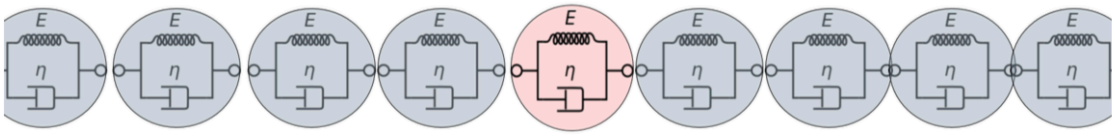

Figure 4.6 A 1D chain of Voigt-Kelvin elements.

The Langevin equation results eq. (4) with $k_B T_{eff}$ given by eq. (2) agree with simulations at all times, but the connection between the simulations and the effective temperature approach remains perhaps un-intuitive. In this section, we attempt to give a more mechanical picture of how the simulations relate to the Langevin equation approach.

Our model of a biofilm is shown in Fig. 4.6. It is a 1D chain of incompressible points separated by Voigt-Kelvin cells. When a new cell is created, its mother shoves everybody aside with all her force, f_{max}. This force will get distributed through the chain as a compressive stress σ_0. When a cell lyses, it will leave behind a tensile stress in its wake. The magnitude of this stress we'll also set, for convenience, to σ_0. We consider only biofilms in the homeostatic limit, so the rate of lysis and division balance.

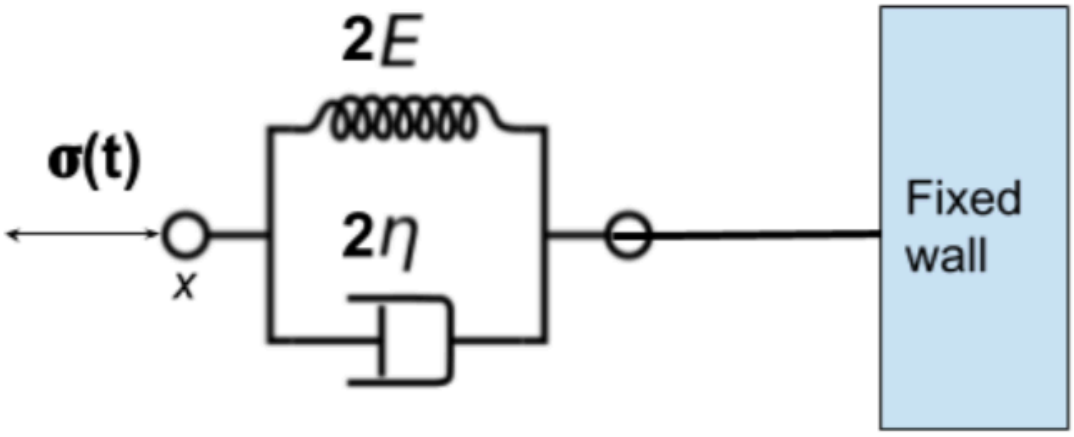

Figure 4.7 Equivalent view to tracking the pink cell.

Consider the motion of a cell somewhere near the center of a vast one-dimensional biofilm (the pink cell in Fig 4.6). This cell is pushed and pulled, back-and-forth, in response

to stresses as cells to its left and right divide and lyse. But how many stresses occur over a time t? If we assume that division and lysis events are Poisson distributed throughout the biofilm, then we can write:

$$\sigma_{total} = \sigma_0(N^{right} - N^{left})$$

where N^{right} and N^{left} are distributed as:

$$p(N) = e^{-\lambda_{act}t}\frac{(\lambda_{act}t)^N}{N!}$$

with λ_{act} the rate of division and lysis in the biofilm. The probability that the cell experiences $\sigma(t)$ at time t will then be a Skellam distribution (which arises from the difference of two Poisson processes):

$$p\left(\frac{\sigma}{\sigma_0}\right) = e^{-2\lambda_{act}t}I_{|N|}(2\lambda_{act}t),$$

where $I\_|N|(2\lambda_{act}t)$ is the modified Bessel function of the first kind. In the limit of large λ_{act}, the distribution converges to a Gaussian with mean 0 and variance $\lambda_{act}t$. This is unsurprising, as it's clear that we can think of the current value of the total stress as undergoing a random walk in one dimension. In other words, we flip a coin at a rate λ_{act} and each time take a step $\pm\sigma_0$ based on whether a birth (lysis) event happened to our left (right). To get a particular trajectory, we can write

$$\dot{\sigma}(t) = \sigma_0\psi(t)$$

$$\sigma(t) = \sigma_0\int_0^t \psi(t')dt',$$

with

$$\langle \psi(t) \rangle = 0$$

$$\langle \psi(t)\psi(t') \rangle = \lambda_{act}\delta(t - t')$$

which will give us the same distribution for $\sigma(t)$ in the end. This gives us a clearer physical picture of the cellular diffusion as well. Tracking a single cell's motion over time is equivalent to tracking the motion of point x in Fig. 4.7. This is nothing more than one much larger Voigt-Kelvin cell subject to a stress that randomly walks in time.

The equation of motion for x is then easy to write down:

$$\sigma(t) = E\varepsilon(t) + \eta\dot{\varepsilon}(t)$$

$$\sigma_0 \int_0^t \psi(t')dt' = E\varepsilon(t) + \eta\dot{\varepsilon}(t)$$

$$E\epsilon_0 \int_0^t \psi(t')dt' = E\varepsilon(t) + \eta\dot{\varepsilon}(t)$$

$$\lambda_\eta \epsilon_0 \int_0^t \psi(t')dt' = \lambda_\eta \varepsilon(t) + \dot{\varepsilon}(t)$$

$$\lambda_\eta \ell \int_0^t \psi(t')dt' = \lambda_\eta x(t) + \dot{x}(t)$$

$$\lambda_\eta \ell\, \psi(t) = \lambda_\eta v(t) + \dot{v}(t)$$

where here, σ_0 is written as $E\epsilon_0$, where ϵ_0 is how much the spring *would* be strained if it were disconnected from the Voigt-Kelvin cell and subjected on its own to an instantaneous

stress σ_0. Then, we divided through by η to present everything in terms of a viscoelastic relaxation rate λ_η. Next, we multiplied by a cell's relaxed length x_0, which turns ε into x and $\dot{\epsilon}$ into $\dot{x}$. Note that $\varepsilon_0 \cdot x_0 = \ell$. Finally, we take a time derivative to get an equation similar to the familiar Langevin equation for Brownian motion. The final line would yield the usual fluctuation-dissipation relation, except that there's a term multiplying the white noise. The root mean squared velocity and position can be solved for; this is the same exercise as above, and yields:

$$\langle x(t)^2 \rangle = \frac{\lambda_{act}\ell^2}{2\lambda_\eta}\left(2\lambda_\eta t - 3 + 4e^{-\lambda_\eta t} - 2e^{-2^{-\lambda_\eta t}}\right),$$

or, in the long-time limit:

$$\langle x(t)^2 \rangle = \lambda_{act}\ell^2 t.$$

CHAPTER 5. CONCLUSIONS AND FUTURE DIRECTIONS

5.1 Conclusions and summary

This dissertation has consisted thus far of one primary theme: the emergent statistical mechanics of bacterial biofilms. Much of this work has been predicated upon the advanced current state of genetic modification, which has allowed for the creation of "customized" cells which can be used for the construction of specific, novel experimental systems. By these means, we have demonstrated that physics plays a unique and important role in biofilm mechanics: it dictates how borders are drawn between strains that make up a colony [32], tells us how to understand and interpret the fluctuations of cells inside a biofilm [33], and gives insight about the diffusion of cells throughout their surface-attached communities [34]. These conclusions were reached over three sets of experiments.

In the first, we mixed two sets of *V. cholerae* strains—nonkiller pairs and mutual killer pairs—together in liquid culture, inoculated them onto agar pads, and incubated them for 24 hours at three different temperatures. Next, we performed confocal microscopy to determine the coarsening structure of the two strains involved. Regardless of incubation temperature, we found that the two strains present in nonkiller biofilms remained well-mixed, and did not coarsen to any significant degree. Contrarily, mutual killer biofilms experienced a temperature-dependent coarsening, reminiscent of the type found in the two-dimensional Ising model of a spin lattice [35], [36]. In three sets of simulations—an individual-based model where cells can kill and reproduce into empty space, an analytical PDE model, and an Ising spin model—we confirmed that the three incubation temperatures served as analogs to timepoints in a Model A coarsening process, as all simulation and

experimental data collapsed onto one master curve when plotting $q_m^2\, S(q)$ *vs.* q_m. Because spatial assortment is one means by which microbes solve their persistent public goods dilemmas [40], [94], this leads to the somewhat counterintuitive hypothesis: that killing allows microbes to become more cooperative. A far-reaching phylogenetic analysis strongly supports this conclusion: after accounting for the phylogenetic variance in secretome size, the number of Type VI secretion systems and effectors explains a whopping 90% of the secretome size. Taken together, this set of experiments showed that T6SS-driven killing generates inter-strain coarsening which proceeds according to the Model A universality class, and which seems to encourage the evolution of cooperation.

The second set of experiments served as a validation and extension of a theory paper by *Risler, et al.* [13] regarding homeostatic fluctuations of a tissue surface. In this work, we again grew two sets of biofilms, each using a pair of two *V. cholerae* strains. These experiments utilized newly-engineered strains which were isogenic to each other modulo their T6SS effectors—briefly, the "weapons" from one of the strains in the previous experiments were swapped into the other strain, resulting in two strains which grow, metabolize, *et c.* identically to each other, but can still kill each other [30], [31]. Isogenic nonkillers were also engineered. Both strain pairs were also modified to produce no EPSes, resulting in more tissue-like biofilms: stacks of cells not bound to each other via extracellular matrix products. After incubation, we measured the topographies of nonkiller and mutual killer biofilms, and found that the latter biofilms were significantly rougher at all length scales. By calculating height-height correlation functions for each biofilm and fitting to a predicted functional form (which depended on the biofilms' mechanical properties) [13], we extracted an effective temperature for each biofilm. These effective

temperatures were predicted to scale linearly with the amount of cellular activity within the biofilm; we found that mutual killer biofilms had effective temperatures roughly 18 times higher than their mutual killer counterparts. Moreover, the correlation functions from which these temperatures were extracted fit the functional form predicted by *Risler, et al.*, and were of the same order of magnitude as a "back-of-the-envelope" prediction offered by the authors. As a check, we performed minimal model, off-lattice simulations wherein spherical cells could reproduce and kill each other on contact. These simulations, which included no other cellular details, recapitulated the activity-dependent surface-roughening behavior predicted by theory and observed in experiments. These simulations also supported the suggested means by which these surface fluctuations appear: each stochastic reproduction or death event results in a long-reaching force on neighboring cells [14], [16], [19], [44], playing the analog of random thermal perturbations. In a general sense, these experiments suggest that genetically engineered biofilms—which are fairly easy to grow—can function as an experimental model for tissues. Specifically, they show that cellular death and reproduction have a fluidizing effect on biofilms, and that—as in equilibrium atomic solids—the internal activity rate of constituents can be extracted via bulk mechanical and structural measurements. As we were surprised above to find that inter-strain coarsening was described the Model A universality class of order-disorder transitions, here it is surprising that these biofilms seem to exhibit a universality in surface fluctuation spectra with thermal permeable membranes [13].

In the third and final set of experiments, we again measured surface topographies of mutual killer biofilms, this time including variants of the above strains which were still isogenic, but now produced extracellular matrix products. Because our previous work used

a somewhat unnatural set of biofilms—the vast majority of biofilms in the wild are composed of cells which secrete matrix products [5], [10], [20], [28], [49], [71], [164]—we wanted to investigate whether the effective temperature model still held in the presence of an extracellular matrix, which could ostensibly damp out the previously-reported cellular fluctuations from reproduction and death. Here, we measured viscosity of Matrix- and Matrix+ mutual killer biofilms, and found that the inclusion of the extracellular matrix increased biofilm viscosity by roughly a factor of three. We then measured surface topographies for these biofilms, and found that while they superficially appeared similar, Matrix+ biofilms had an effective temperature roughly three times higher than that of their Matrix- counterparts. Prompted by an excellent question from Prof. Joshua Weitz, we wondered what this effective temperature implied in terms of the amount of motion experienced by the biofilms' cellular constituents, and to that end used the generalized Stokes-Einstein relationship to calculate an effective *diffusion* rate for each biofilm. To our surprise, we found that the increase in effective temperature and viscosity canceled, yielding net cellular diffusivities which were independent of viscosity. While at first this was surprising, it's actually quite reasonable: in standard thermal diffusion, described by the Stokes-Einstein relation, diffusion and viscosity are related by a fluctuation-dissipation relationship, which arises because both quantities share a physical origin [42], [43]. In our biofilms, however, viscosity is primarily a product of interactions with the extracellular matrix, whereas diffusivity comes solely from the reproduction and death of cells. The two terms do *not* share a physical origin, and thus no fluctuation-dissipation relationship constrains their proportionality as it does in the case of typical thermal diffusion. To test this intuition, we developed a simulation wherein cells were modeled as Voigt-Kelvin

elements, and cellular death and reproduction induced instantaneous step-stresses across the biofilm. When the timescales for relaxation and reproduction are set to experimental values, we find that diffusivity is effectively independent of viscosity. Lastly, we compared to analytic predictions from a modified Langevin equation for Brownian motion, which had an added white noise term which was identified with the driving forces from reproduction. This approach also suggested, in the biologically-relevant limit, that diffusion should be independent from viscosity. Diffusivity values extracted via surface topography (*i.e.* converted from effective temperatures) and theory lined up well, and also lined up with preliminary experimental data calculated from the motion of tracer beads embedded within biofilms (all are within half an order of magnitude). These experiments, simulations, and analytic results together suggest that the effective temperature calculated in the above work has a physical, kinetic interpretation, and that the associated cellular diffusion is independent of the viscosity of the biofilms in which these cells make their home.

This concludes the published (and in the case of the last work, under review) work. What follows is a discussion of future work which relies on the use of white-light interferometry as a novel tool for studying—and more specifically, *measuring* or *testing*—bacterial biofilms.

5.2 Future directions

A spectre is haunting this thesis—the spectre of interferometry. Observing fluctuations in a tissue or biofilm surface due individual reproduction and death events is

difficult—it requires extremely high out-of-plane resolution on reasonably short timescales. White-light interferometry, then, is almost a natural solution to the problem of the experimental realization of the theory proposed in Risler, *et al.* [13], but why should it be limited simply to the validation of a single theory?

The above fluctuation-response experiments demonstrate that with one simple surface scan, we can extract information that previously would have required comparatively complex biological experiments or which we simply would not have been able to access. At its heart, the value to this approach is that we can quickly and easily measure with extreme precision the amount of growth—or lack thereof—in a biofilm. The specifics of the biofilm are not important: it doesn't matter whether the biofilm consists of *V. cholerae, E. coli*, or *P. aeruginosa;* it doesn't even matter whether its bacterial or fungal, what the shapes of the constituent cells are, or what they tend to secrete. Regardless of these details, we have a means by which we can measure effectively differential changes in growth rate. Taking a step back from our original usage of this type of measurement, we note that the rapid procurement of extremely high-resolution data lends itself to several novel phenotypic identification techniques, including but not limited to state of the art-crushing antibiotic resistance tests.

5.2.1 Machine learning for antibiotic resistance classification

While there are many different types of antibiotic treatment, they can generally be classified into two camps: bacteriostatic treatments, which prevent the reproduction of bacteria but do not kill them, and bactericidal treatments, which kill bacteria by various means (destruction of the cell wall, interruption of DNA replication, induction of protein

misfolding, *et c.*) [165]. By inoculating bacterial cells onto an agar plate infused with either of these classes of antibiotics, we get one of two results: either a biofilm begins to grow from the initial coffee ring, indicating resistance, or it does not, indicating susceptibility. Moreover, as cells grow (or don't grow), the relative height differences between neighboring cells take on characteristic values and correlations which depend on that growth rate. *I.e.,* topographies diverge as a function of growth rate, but so do spatial derivatives of those topographies—and because our resolution is uniquely high, those spatial derivatives (hereafter "curvature maps") are of uniquely high *quality*.

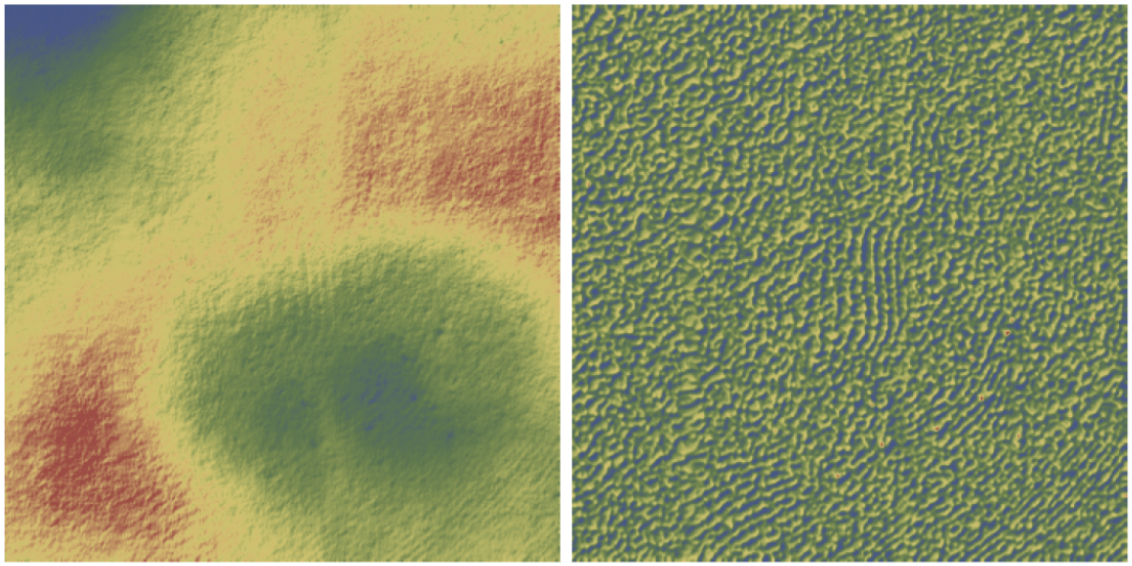

Figure 5.1 An example of the topography-curvature pairings which are used to train classifiers; this pairing, *e.g.*, would be given as singular unit with the label "Mutual Killer". (In practice, the arrays used for classification are visualized in greyscale.)

The fact that we have such high-quality, high-resolution data (each topography is $O(10^6)$ datapoints) that can be taken with some rapidity (each topography takes only ~1

minute to capture) practically begs us to use machine learning in some capacity. Indeed, by inoculating strains of E. coli which were isogenic modulo their susceptibility to an antibiotic mixed into the agar pad on which they were grown, classifiers trained via standard "leave-one-out" cross-validation achieved a 100% success rate (with near-100% confidence for every sample) at determining susceptibility/resistance of a given nascent biofilm after incubation for only a single hour—enough time for two doublings, at most. The classifiers were trained using both the biofilm topographies and their curvature maps: we observed a significant performance decrease when leaving out either of the two, suggesting that they both contain important and unique information. Using this technique, we can determine susceptibility/resistance in more than an order of magnitude less time than traditional tests.

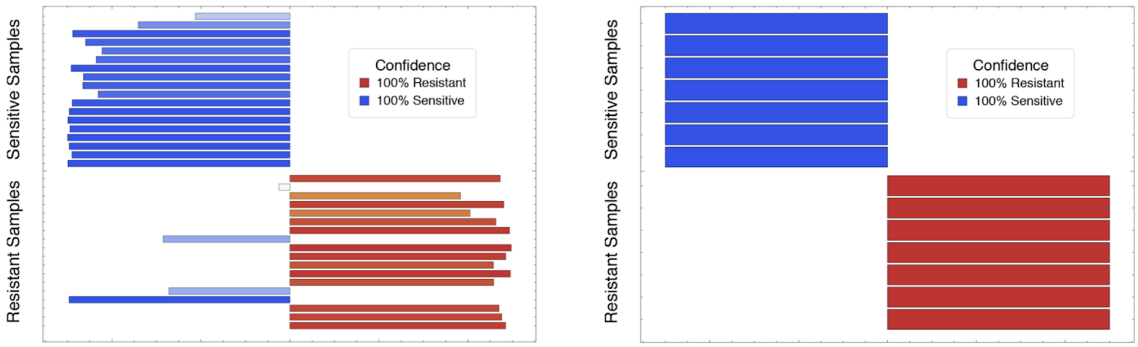

Figure 5.2 a. After only 30 minutes of incubation, we can get a fairly accurate identification rate. b. With an hour of incubation time, however, we achieve a 100% success rate with ~100% confidence in each classification.

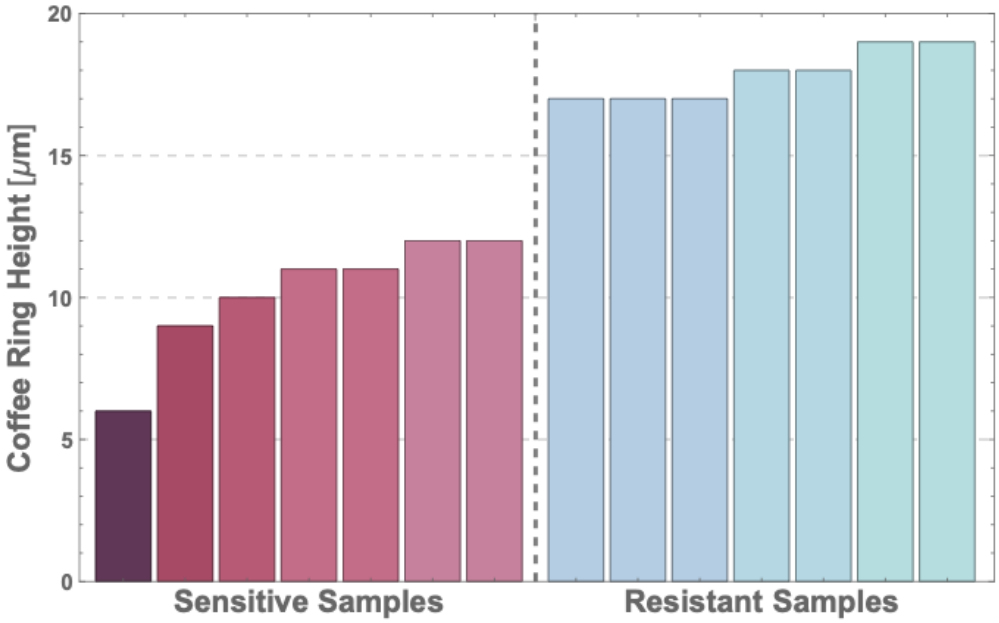

Figure 5.3 After an hour of incubation, preliminary results suggest that even a simple measurement of the coffee ring height is sufficient to delineate sensitive strains from resistant ones. While the delineation is fairly clear, it is—unlike the machine learning results—not binary, so those results are preferred where possible.

5.2.2 Extremely high resolution for "one in a million" heteroresistance detection

Bacteria are not always completely susceptible or resistant to a given antibiotic treatment, however: sometimes, a certain proportion of the population will be resistant, and when that proportion survives and reproduces, their offspring will share that resistance proportion. In these cases, the proportion might vary from as high as one in ten down to as low as one in a million. While heteroresistance is a fairly new area of interest, it holds great importance in medical contexts [166]: in many cases (*e.g.* cystic fibrosis), a traditional test would classify a cultured bacterial strain where one in ten-thousand cells survive an antibiotic treatment as "susceptible", yet using that treatment on the patient would fail to

eradicate the infection [167], [168]. Heteroresistance provides an explanation for why this happens, and with high-precision interferometry, we can not only detect the difference between heteroresistant strains and susceptible ones, but we can measure differing levels of heteroresistance, all the way down from susceptible up to resistant: and for this, we don't even need machine learning (though it does work).

Consider the case where only one cell reproduces among thousands. Numerically, this is not so different from no reproduction at all, at least on the timescale of a few doublings. From a topographical perspective, on the other hand—especially in light of the previous discussions of long-range cellular diffusion caused by reproduction—this tiny difference in number can result in quite a difference! In practice, this works even better than we could have hoped: for example, we measured topographies of susceptible and resistant *P. aeruginosa* strains, as well as those with .01% and 1% resistance rates after only 90 minutes of incubation on an antibiotic-infused agar pad. By merely looking at the distributions of measured heights, we were able to tell the strains apart by eye:

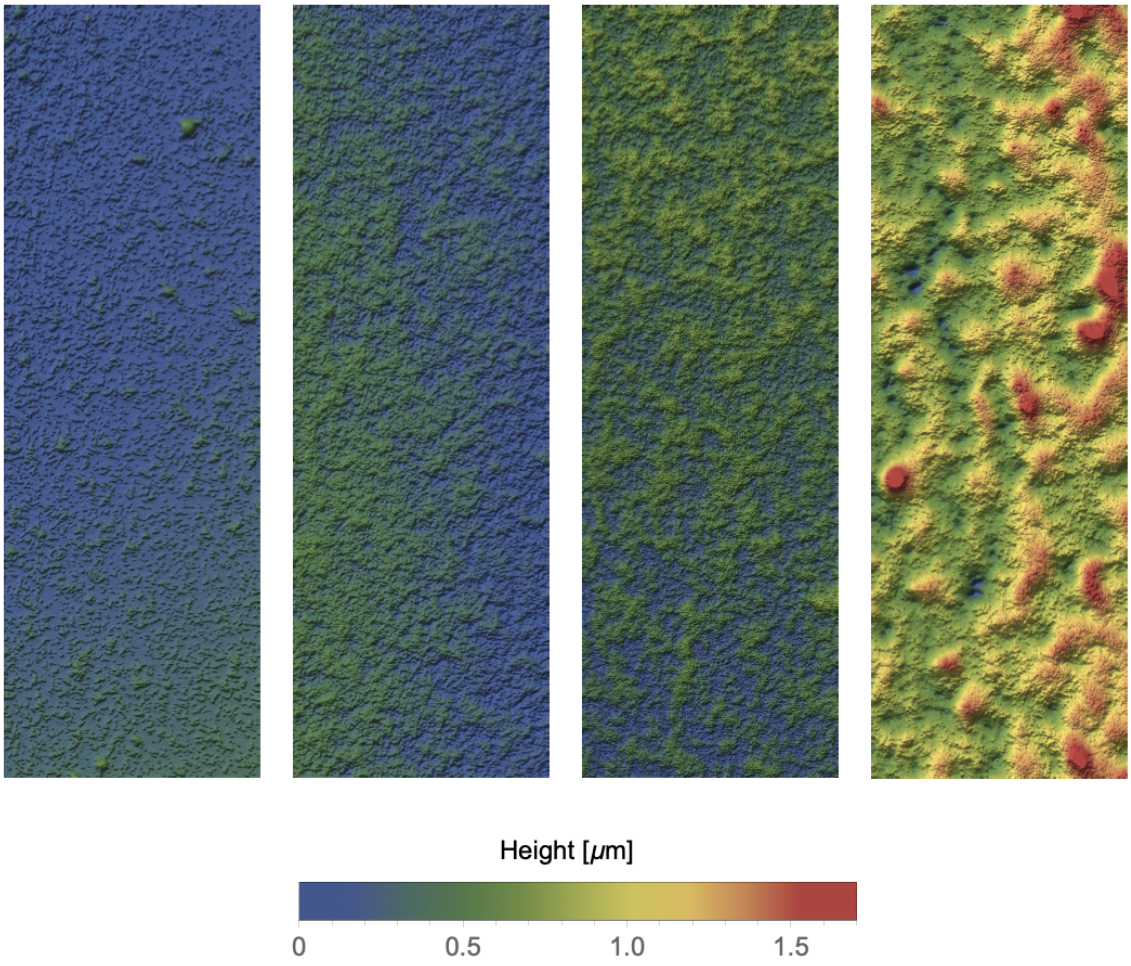

Figure 5.4 Nascent biofilm homelands of *P. aeruginosa* after 90 minutes of incubation at 37˚C on an antibiotic-infused agar pad. The strains used were completely susceptible, .01% resistant, 1% resistant, and 100% resistant, respectively.

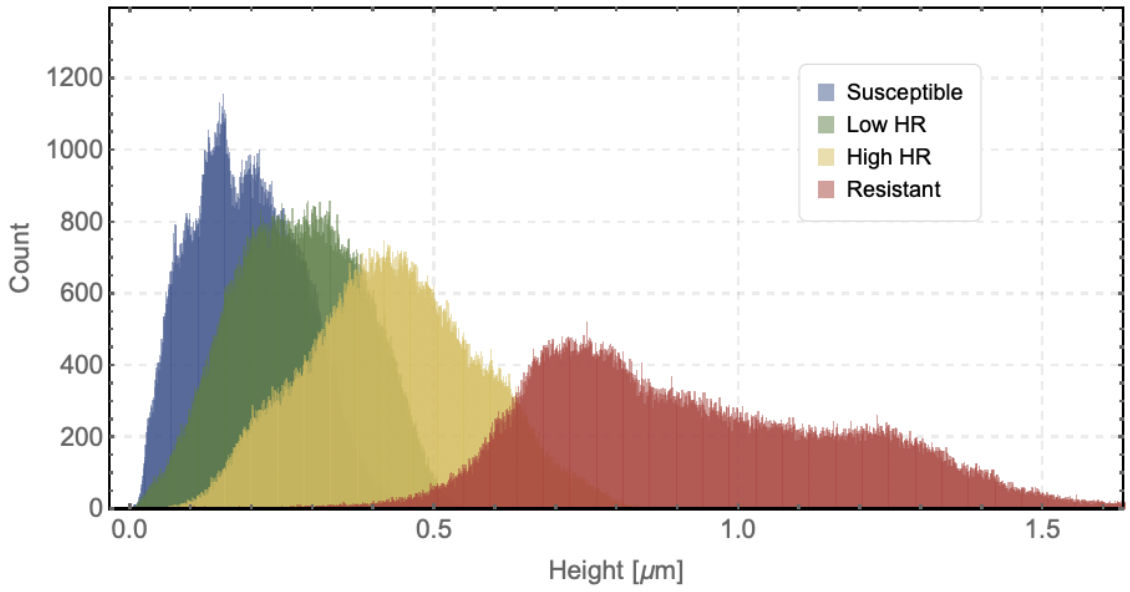

Figure 5.5 Histograms of the topographies measured above show clear, distinct separation as a function of heteroresistance level.

Several other metrics were successful: a simple comparison of the mean heights, histograms of curvature, classifiers trained on pairs of topographies and their corresponding curvature maps, and even the effective temperature calculation mentioned above (and shown below) all served to differentiate between the different heteroresistance levels, indicating that interferometry is not only a novel tool for the measurement of particular, tissue-like biofilms, but has more general uses in previously-unexpected fields.

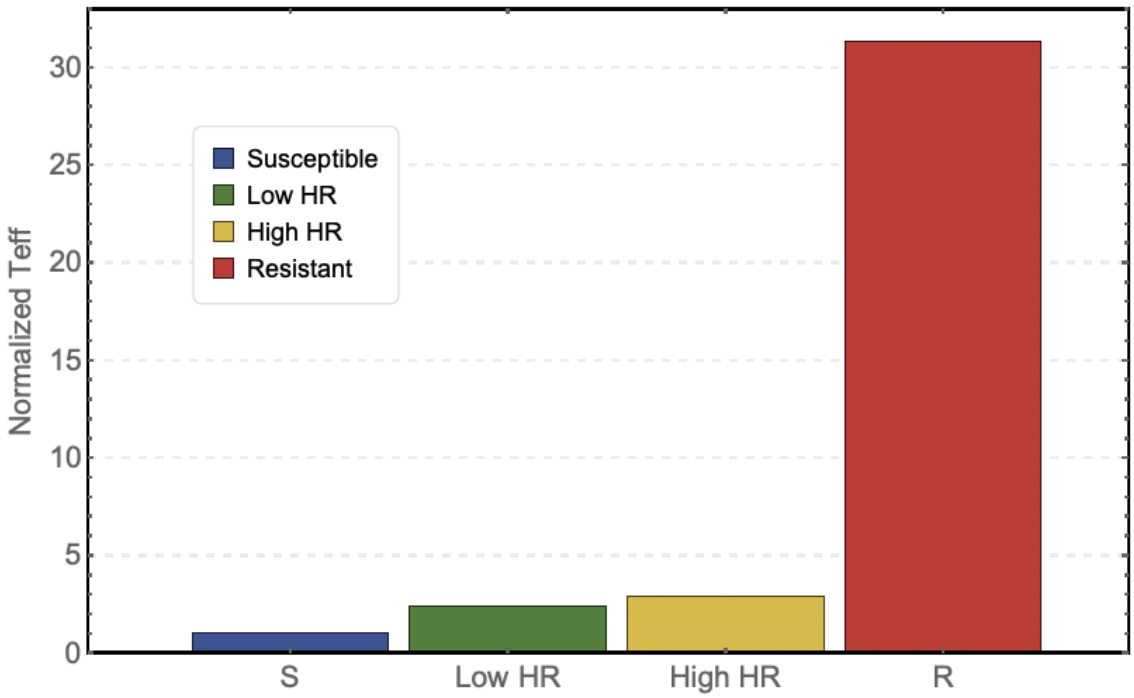

Figure 5.6 The effective temperatures developed in Chapter 2 can also distinguish between different heteroresistance levels. The labels correspond to "susceptible" ($< 10^{-6}$ survival rate), "low heteroresistant" (.01%), "high heteroresistant" (1%), and "Resistant" (100%).

5.2.3 Machine learning with Matrix+ biofilms

This realization also led us to revisit some of our previous work. For example, in the case of the Matrix- mutants used in the "effective temperature" section of this thesis, nonkiller and mutual killer biofilms were uniquely distinguished by their effective temperatures: the highest temperature amongst the nonkiller biofilms was lower than the lowest found amongst the mutual killer biofilms. From a calculational perspective, this is simply because every nonkiller biofilm was much flatter and smoother than every mutual killer biofilm. Contrarily, when we performed these measurements for Matrix+ strains, we

found that the topographic differences between nonkiller and mutual killer biofilms was much less pronounced—and thus, the effective temperature distribution was no longer cleaved down the middle (though the mean effective temperature was still significantly higher in mutual killer biofilms).

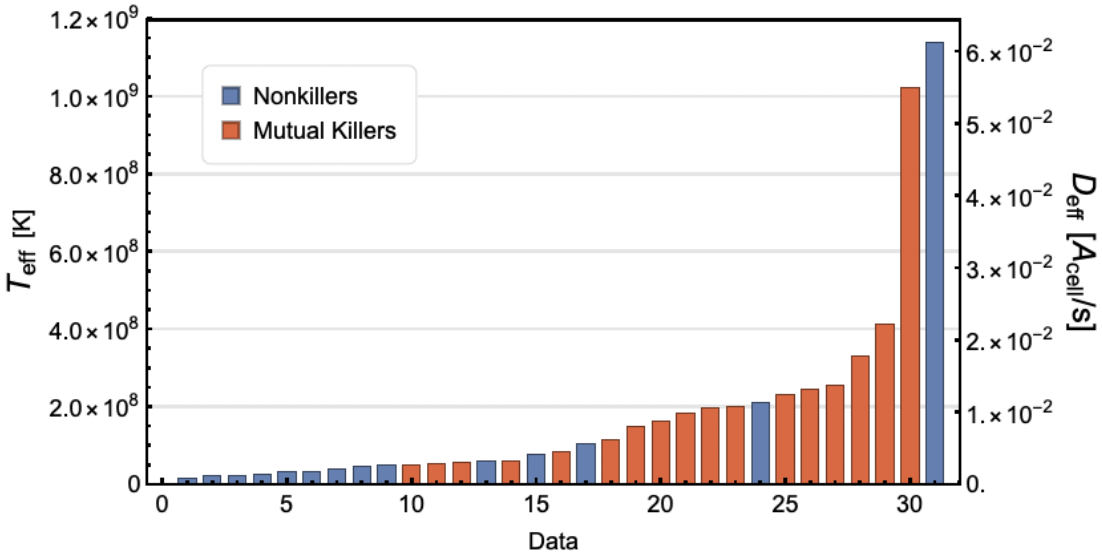

Figure 5.7 Calculated effective temperatures for nonkiller and mutual killer Matrix+ biofilms were not as cleanly separated as for the Matrix- mutants (Fig. 1.4).

How well would the machine learning approach developed above work, as compared to the much more specialized effective temperature approach? For the Matrix- mutants, the topography + curvature classifiers achieved a 100% success rate. And indeed, even for the Matrix+ strains, classifiers were able to distinguish nonkiller biofilms from mutual killer biofilms 100% of the time, and with high confidence.

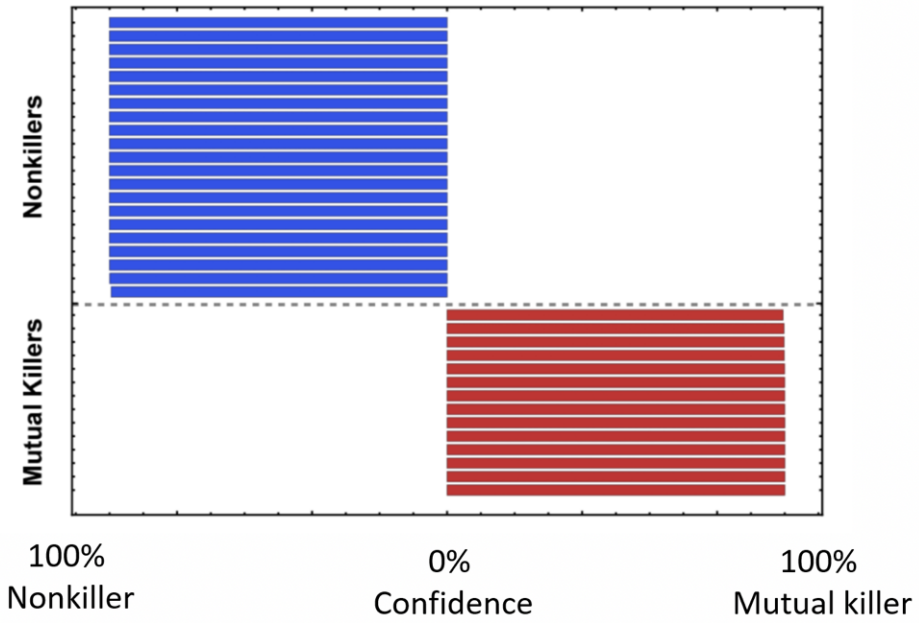

Figure 5.8 Contrary to classification by effective temperature, classifiers trained on topography and curvature maps correctly identified nonkiller and mutual killers with 100% accuracy and next to 100% confidence.

I also trained classifiers on "wild type" strains, which were isolated from clinical and environmental strains and not further modified (save to change killing from "on under certain circumstances" to "always on" or "always off" [30], [31]). These strains are generally less well-behaved, as the competing strains are not isogenic and can have different behaviors based on subtle environmental cues (*e.g.* different growth and activity rates as a function of and humidity temperature). The effective temperature calculation does work to distinguish these biofilms, but again, only on average—the distribution of effective temperatures is fairly well-mixed. Again, classifiers were able to distinguish nonkiller from mutual killer biofilms 100% of the time and with extremely high confidence.

While this may seem strange at first—as if something has gone wrong, or something is too good to be true—in actuality, it's not altogether unreasonable. A typical analysis of this sort uses about 25-35 samples, which doesn't seem like a very high number. Each of these samples, however, is a pairing of two ~700x700 matrices, resulting in a total of nearly 3 million data points per sample. As we saw in the height histograms shown above, the quantity and quality of this data is so high that even the human eye can distinguish between samples as long as the data is presented in the correct way; adding machine learning to the mix only improves our ability to tease out information hidden in the surface. Whether we're determining discrete binary antibiotic resistance, a continuous spectrum of heteroresistance, or determining a specific phenotypic difference between two sets of biofilms, interferometry is a novel and highly valuable experimental tool.

REFERENCES

[1] P. Watnick and Kolter, R., "Biofilm, city of microbes.," *J. Bacteriol.*, vol. 182, no. 10, pp. 2675–2679., May 2000.

[2] M. G. Mazza, "The physics of biofilms---an introduction," *J Phys D Appl Phys*, vol. 49, 2016.

[3] R. Dirzo and P. H. Raven, "The ecological significance of biofilm formation by plant-associated bacteria," *Annu. Rev. Environ. Resour.*, vol. 28, no. 1, pp. 137–167, Sep. 2003.

[4] H. C. Flemming and J. Wingender, "The biofilm matrix," *Nat. Rev. Microbiol.*, vol. 8, no. 623, 2010.

[5] C. D. Nadell, K. Drescher, and K. R. Foster, "Spatial structure, cooperation and competition in biofilms," *Nat. Rev. Microbiol.*, vol. 14, no. 9, pp. 589–600, 2016.

[6] C. J. A. Warner *et al.*, "Living in the matrix: assembly and control of Vibrio cholerae biofilms," *Nat. Rev. Microbiol.*, vol. 13, no. 5, pp. 255–268, 2015.

[7] J. L. Balcázar, J. Subirats, and C. M. Borrego, "The role of biofilms as environmental reservoirs of antibiotic resistance.: Discovery Service for West Virginia Wesleyan College," *Front. Microbiol.*, vol. 6, p. 1216, 2015.

[8] J. B. Xavier and K. R. Foster, "Cooperation and conflict in microbial biofilms," *Proc. Natl. Acad. Sci.*, vol. 104, no. 3, pp. 876–881, Nov. 2007.

[9] J. Quintiliani, J and P. Courvalin, “Mechanisms of resistance to antimicrobial agents,” *Man. Clin. Microbiol. 6th ed*, vol. 9, no. 1, pp. 1308–1326, Jan. 1995.

[10] P. B.W. *et al.*, “Viscoelasticity of biofilms and their recalcitrance to mechanical and chemical challenges,” *FEMS Microbiol. Rev.*, vol. 39, no. 2, pp. 234–245, 2015.

[11] J. E. Strassmann, O. M. Gilbert, and D. C. Queller, “Kin Discrimination and Cooperation in Microbes,” *Annu. Rev. Microbiol.*, vol. 65, no. 1, pp. 349–367, 2010.

[12] G. M. Dunny, T. J. Brickman, and M. Dworkin, “Multicellular behavior in bacteria: Communication, cooperation, competition and cheating,” *BioEssays*, vol. 30, no. 4, pp. 296–298, Mar. 2008.

[13] T. Risler, A. Peilloux, and J. Prost, “Homeostatic Fluctuations of a Tissue Surface,” *Phys. Rev. Lett.*, vol. 115, no. 25, p. 258104, 2015.

[14] J. Ranft, M. Basan, J. Elgeti, J.-F. Joanny, J. Prost, and F. Julicher, “Fluidization of tissues by cell division and apoptosis,” *Proc. Natl. Acad. Sci.*, vol. 107, no. 49, pp. 20863–20868, Dec. 2010.

[15] S. Ornes, “Core Concept: How nonequilibrium thermodynamics speaks to the mystery of life,” *Proc. Natl. Acad. Sci.*, vol. 114, no. 3, pp. 423–424, 2017.

[16] D. A. Matoz-Fernandez, K. Martens, R. Sknepnek, J. L. Barrat, and S. Henkes, “Cell division and death inhibit glassy behaviour of confluent tissues,” *Soft Matter*, vol. 13, no. 17, pp. 3205–3212, Apr. 2017.

[17] G. Forgacs, R. A. Foty, Y. Shafrir, and M. S. Steinberg, “Viscoelastic properties of

living embryonic tissues: A quantitative study," *Biophys. J.*, vol. 74, no. 5, pp. 2227–2234, 1998.

[18] D. Bi, J. H. Lopez, J. M. Schwarz, and M. L. Manning, "A density-independent glass transition in biological tissues," *Nat. Phys.*, vol. 11, no. 1, p. 5, Aug. 2014.

[19] X. Li, S. Sinha, D. Thirumalai, A. N. Malmi-Kakkada, and H. S. Samanta, "Cell Growth Rate Dictates the Onset of Glass to Fluidlike Transition and Long Time Superdiffusion in an Evolving Cell Colony," *Phys. Rev. X*, vol. 8, no. 2, p. 021025, 2018.

[20] H.-S. L., C. J.W., and S. P., "Bacterial biofilms: From the natural environment to infectious diseases," *Nat. Rev. Microbiol.*, vol. 2, no. 2, pp. 95–108, 2004.

[21] E. S. Antonova and B. K. Hammer, "Quorum-sensing autoinducer molecules produced by members of a multispecies biofilm promote horizontal gene transfer to Vibrio cholerae," *FEMS Microbiol. Lett.*, vol. 322, no. 1, pp. 68–76, 2011.

[22] D. van der Kooij, H. R. Veenendaal, and W. J. H. Scheffer, "Biofilm formation and multiplication of Legionella in a model warm water system with pipes of copper, stainless steel and cross-linked polyethylene," *Water Res.*, vol. 39, no. 13, pp. 2789–2798, 2005.

[23] M. J. Lehtola *et al.*, "Microbiology, chemistry and biofilm development in a pilot drinking water distribution system with copper and plastic pipes," *Water Res.*, vol. 38, no. 17, pp. 3769–3779, 2004.

[24] R. Kümmerli, A. S. Griffin, S. A. West, A. Buckling, and F. Harrison, "Viscous medium promotes cooperation in the pathogenic bacterium Pseudomonas aeruginosa," *Proc. R. Soc. B Biol. Sci.*, vol. 276, no. 1672, pp. 3531–3538, 2009.

[25] M. Davis-Fields *et al.*, "Evolutionary adaptations of biofilms infecting cystic fibrosis lungs promote mechanical toughness by adjusting polysaccharide production," *npj Biofilms Microbiomes*, vol. 3, no. 1, pp. 0–1, 2017.

[26] P. K. Singh, A. L. Schaefer, M. R. Parsek, T. O. Moninger, M. J. Welsh, and E. P. Greenberg, "Quorum-sensing signals indicate that cystic fibrosis lungs are infected with bacterial biofilms," *Nature*, vol. 407, no. 6805, pp. 762–764, 2000.

[27] T. Bjarnsholt *et al.*, "Pseudomonas aeruginosa biofilms in the respiratory tract of cystic fibrosis patients," *Pediatr. Pulmonol.*, vol. 44, no. 6, pp. 547–558, 2009.

[28] T. E. Angelini, M. P. Brenner, D. a. Weitz, J. N. Wilking, and A. Seminara, "Biofilms as complex fluids," *MRS Bull.*, vol. 36, no. 05, pp. 385–391, May 2011.

[29] B. K. Hammer and B. L. Bassler, "Quorum sensing controls biofilm formation in Vibrio cholerae - Hammer - 2003 - Molecular Microbiology - Wiley Online Library," *Mol. Microbiol.*, vol. 51, no. 1, p. 1521, Aug. 2003.

[30] S. S. Watve, J. Thomas, and B. K. Hammer, "CytR is a global positive regulator of competence, type VI secretion, and chitinases in Vibrio cholerae," *PLoS One*, vol. 10, no. 9, p. 24, Sep. 2015.

[31] J. Thomas, S. S. Watve, W. C. Ratcliff, and B. K. Hammer, "Horizontal Gene

Transfer of Functional Type VI Killing Genes by Natural Transformation," *MBio*, vol. 8, no. 4, Jul. 2017.

[32] L. McNally *et al.*, "Killing by Type VI secretion drives genetic phase separation and correlates with increased cooperation," *Nat. Commun.*, vol. 8, p. 14371, 2017.

[33] J. Thomas *et al.*, "Immotile Active Matter: Activity from Death and Reproduction," *Phys. Rev. Lett.*, vol. 120, no. 1, p. 18101, 2018.

[34] A. Kalziqi, S. L. Ng, D. Yanni, G. Steinbach, B. K. Hammer, and P. J. Yunker, "Viscosity independent diffusion mediated by death and reproduction in biofilms." 2019.

[35] R. Wittkowski, A. Tiribocchi, J. Stenhammar, R. J. Allen, D. Marenduzzo, and M. E. Cates, "Scalar φ 4 field theory for active-particle phase separation," *Nat. Commun.*, vol. 5, p. 4351, 2014.

[36] G. Brown, P. A. Rikvold, and M. Grant, "Universality and scaling for the structure factor in dynamic order-disorder transitions," *Phys. Rev. E - Stat. Physics, Plasmas, Fluids, Relat. Interdiscip. Top.*, vol. 58, no. 5, pp. 5501–5507, 1998.

[37] L. Onsager, "Crystal Statistics. I. A Two-Dimensional Model with an Order-Disorder Transition," *Phys. Rev.*, vol. 65, no. 3–4, pp. 117–149, Feb. 1944.

[38] E. E. Bernardy, M. A. Turnsek, S. K. Wilson, C. L. Tarr, and B. K. Hammer, "Diversity of Clinical and Environmental Isolates of Vibrio cholerae in Natural Transformation and Contact-Dependent Bacterial Killing Indicative of Type VI

Secretion System Activity," *Appl. Environ. Microbiol.*, vol. 82, no. 9, pp. 2833–2842, 2016.

[39] J. D. Van Dyken, M. J. I. Müller, K. M. L. MacK, and M. M. Desai, "Spatial population expansion promotes the evolution of cooperation in an experimental prisoner's dilemma," *Curr. Biol.*, vol. 23, no. 10, pp. 919–923, 2013.

[40] N. S. Wingreen, B. L. Bassler, K. Drescher, H. A. Stone, and C. D. Nadell, "Solutions to the Public Goods Dilemma in Bacterial Biofilms," *Curr. Biol.*, vol. 24, no. 1, pp. 50–55, 2013.

[41] L. Demuyser, M. A. Jabra-Rizk, and P. Van Dijck, "Microbial cell surface proteins and secreted metabolites involved in multispecies biofilms," *Pathog. Dis.*, vol. 70, no. 3, pp. 219–230, 2014.

[42] Y. L. Klimontovich, "Fluctuation - Dissipation Relation," in *Turbulent Motion and the Structure of Chaos: A New Approach to the Statistical Theory of Open Systems, vol*, vol. 42, Dordrecht, Springer: Springer, Dordrecht, 1991, p. 135.

[43] R. Kubo, "The fluctuation-dissipation theorem," *Reports Prog. Phys.*, vol. 29, no. 1, pp. 255–284, Jan. 1966.

[44] M. Basan, J. Prost, J. F. Joanny, and J. Elgeti, "Dissipative particle dynamics simulations for biological tissues: Rheology and competition," *Phys. Biol.*, vol. 8, no. 2, p. 1, Apr. 2011.

[45] M. Spellings *et al.*, "Shape control and compartmentalization in active colloidal

cells," *Proc. Natl. Acad. Sci.*, vol. 112, no. 34, pp. E4642–E4650, 2015.

[46] M. C. Marchetti *et al.*, "Soft Active Matter," *Rev. Mod. Phys.*, vol. 85, p. 3, 2012.

[47] A. Einstein, "Über die von der molekularkinetischen Theorie der Wärme geforderte Bewegung von in ruhenden Flüssigkeiten suspendierten Teilchen," *Ann. Phys.*, vol. 322, no. 8, pp. 549–560, 1905.

[48] I. Klapper, C. J. Rupp, R. Cargo, B. Purvedorj, and P. Stoodley, "Viscoelastic fluid description of bacterial biofilm material properties," *Biotechnol. Bioeng.*, vol. 80, no. 3, pp. 289–296, 2002.

[49] N. G. Cogan and J. P. Keener, "The role of the biofilm matrix in structural development," *Math. Med. Biol. A J. IMA*, vol. 21, no. 2, pp. 147–166, 2004.

[50] M.-F. D.A., A. E., B. J.-L., B. E., and M. K., "Nonlinear Rheology in a Model Biological Tissue," *Phys. Rev. Lett.*, vol. 118, no. 15, p. 158105, Apr. 2017.

[51] F. Abbas *et al.*, "Oral Biofilm Architecture on Natural Teeth," *PLoS One*, vol. 5, no. 2, p. e9321, Feb. 2010.

[52] R. L. Townsin, "The Ship Hull Fouling Penalty," *Biofouling*, vol. 19, no. sup1, pp. 9–15, 2003.

[53] S. D. Stowe, J. J. Richards, A. T. Tucker, R. Thompson, C. Melander, and J. Cavanagh, "Anti-Biofilm Compounds Derived from Marine Sponges," *Mar. Drugs*, vol. 9, no. 10, pp. 2010–2035, 2011.

[54] S. A. West, A. S. Griffin, and et al, "Social evolution theory for microbes," *Nat.*

Rev. Microbiol., vol. In press, pp. 597–607, 2006.

[55] N. M. Oliveira, R. Niehus, and K. R. Foster, "Evolutionary limits to cooperation in microbial communities," *Proc. Natl. Acad. Sci.*, vol. 111, no. 50, pp. 17941–17946, 2014.

[56] M. E. Hibbing, C. Fuqua, M. R. Parsek, and S. B. Peterson, "Bacterial competition: surviving and thriving in the microbial jungle.," *Nat. Rev. Microbiol.*, vol. 8, no. 1, pp. 15–25, 2010.

[57] S. P. Diggle, A. S. Griffin, G. S. Campbell, and S. A. West, "SUPPLEMENTARY MATERIAL to Cooperation and conflict in quorum-sensing bacterial populations.," *Nature*, vol. 450, no. 7168, pp. 411–4, 2007.

[58] A. Buckling *et al.*, "Siderophore-mediated cooperation and virulence in Pseudomonas aeruginosa," *FEMS Microbiol. Ecol.*, vol. 62, no. 2, pp. 135–141, 2007.

[59] K. Hammerschmidt, C. J. Rose, B. Kerr, and P. B. Rainey, "Life cycles, fitness decoupling and the evolution of multicellularity: Supplementary Information," *Nature*, vol. 515, no. 7525, pp. 75–79, 2014.

[60] A. Sanchez and J. Gore, "Feedback between Population and Evolutionary Dynamics Determines the Fate o...: GCU Library Resources - Sciences," *P Lo S Biol.*, vol. 11, p. e1001547, 2008.

[61] M. Travisano and G. J. Velicer, "Strategies of microbial cheater control," *Trends*

Microbiol., vol. 12, no. 2, pp. 72–78, 2004.

[62] J. A. Damore and J. Gore, "Understanding microbial cooperation: supplemental information," *J. Theor. Biol.*, vol. 299, no. 1, pp. 31–41, 2012.

[63] J. A. Fletcher and M. Doebeli, "A simple and general explanation for the evolution of altruism," *Proc. R. Soc. B Biol. Sci.*, vol. 276, no. 1654, pp. 13–19, 2009.

[64] M. Vos and G. J. Velicer, "Isolation by Distance in the Spore-Forming Soil Bacterium Myxococcus xanthus," *Curr. Biol.*, vol. 18, no. 5, pp. 386–391, 2008.

[65] J. Smith, J. E. Strassmann, and D. C. Queller, "Fine-scale spatial ecology drives kin selection relatedness among cooperating amoebae," *Evolution (N. Y).*, vol. 70, no. 4, pp. 848–859, 2016.

[66] B. Momeni, A. J. Waite, and W. Shou, "Spatial self-organization favors heterotypic cooperation over cheating," *Elife*, vol. 2013, no. 2, p. e00960, 2013.

[67] S. Estrela and S. P. Brown, "Metabolic and Demographic Feedbacks Shape the Emergent Spatial Structure and Function of Microbial Communities," *PLoS Comput. Biol.*, vol. 9, no. 12, p. e1003398, 2013.

[68] F. D. C. Farrell, J. Tailleur, D. Marenduzzo, and M. C. Marchetti, "Pattern formation in particles with density-dependent motility: Supplementary information," *Phys. Rev. Lett.*, vol. 108, pp. 3–5, 2012.

[69] M. J. Q. Wong *et al.*, "Microbial Herd Protection Mediated by Antagonistic Interaction in Polymicrobial Communities," *Appl. Environ. Microbiol.*, vol. 82, no.

23, pp. 6881–6888, 2016.

[70] D. E. Rozen, “The Ecology and Evolution of Microbial Chemical Warfare,” *Trends Microbiol.*, vol. 24, pp. 1–9, 2016.

[71] L. Chao and B. R. Levin, “Structured habitats and the evolution of anticompetitor toxins in bacteria.,” *Proc. Natl. Acad. Sci. U. S. A.*, vol. 78, no. 10, pp. 6324–8, 1981.

[72] O. Rendueles, M. Amherd, and G. J. Velicer, “Positively Frequency-Dependent Interference Competition Maintains Diversity and Pervades a Natural Population of Cooperative Microbes,” *Curr. Biol.*, vol. 25, no. 13, pp. 1673–1681, 2015.

[73] B. T. Ho, T. G. Dong, and J. J. Mekalanos, “Cell Host & Microbe Review A View to a Kill: The Bacterial Type VI Secretion System,” *Cell Host Microbe*, vol. 15, pp. 9–21, 2014.

[74] A. B. Russell, S. B. Peterson, and J. D. Mougous, “Type VI secretion system effectors: poisons with a purpose - Russell2014_T6SS_Review.pdf,” *Nat. Rev. Microbiol.*, vol. 12, pp. 137–148, 2014.

[75] S. Pukatzki *et al.*, “Identification of a conserved bacterial protein secretion system in Vibrio cholerae using the Dictyostelium host model system.,” *Proc. Natl. Acad. Sci. U. S. A.*, vol. 103, no. 5, pp. 1528–33, 2006.

[76] D. L. MacIntyre, S. T. Miyata, M. Kitaoka, and S. Pukatzki, “The Vibrio cholerae type VI secretion system displays antimicrobial properties,” *Proc. Natl. Acad. Sci.*, vol. 107, no. 45, pp. 19520–19524, 2010.

[77] D. Unterweger *et al.*, "Constitutive Type VI Secretion System Expression Gives Vibrio cholerae Intra- and Interspecific Competitive Advantages," *PLoS One*, vol. 7, no. 10, p. e48320, 2012.

[78] T. M. Brooks, D. Unterweger, V. Bachmann, B. Kostiuk, and S. Pukatzki, "Lytic activity of the Vibrio cholerae type VI secretion toxin VgrG-3 is inhibited by the antitoxin TsaB," *J. Biol. Chem.*, vol. 288, no. 11, pp. 7618–7625, 2013.

[79] T. G. Dong, B. T. Ho, D. R. Yoder-Himes, and J. J. Mekalanos, "Identification of T6SS-dependent effector and immunity proteins by Tn-seq in Vibrio cholerae," *Proc. Natl. Acad. Sci.*, vol. 110, no. 7, pp. 2623–2628, 2013.

[80] D. Unterweger *et al.*, "The vibrio cholerae type VI secretion system employs diverse effector modules for intraspecific competition," *Nat. Commun.*, vol. 5, p. 3549, 2014.

[81] D. B. Borenstein, P. Ringel, M. Basler, and N. S. Wingreen, "Established Microbial Colonies Can Survive Type VI Secretion Assault," *PLoS Comput. Biol.*, vol. 11, no. 10, p. e1004520, 2015.

[82] W. D. Hamilton, "Geometry for the selfish herd," *J. Theor. Biol.*, vol. 31, no. 2, pp. 295–311, 1971.

[83] D. Heerman and K. Binder, *Monte Carlo Simulation In Statistical Physics*. 2010.

[84] L. Townsley, M. P. Sison Mangus, S. Mehic, and F. H. Yildiz, "Response of Vibrio cholerae to Low-Temperature Shifts: CspV Regulation of Type VI Secretion,

Biofilm Formation, and Association with Zooplankton," *Appl. Environ. Microbiol.*, vol. 82, no. 14, pp. 4441–4452, 2016.

[85] F. Sciortino, A. B. Schofield, F. Ciulla, E. Zaccarelli, D. A. Weitz, and P. J. Lu, "Gelation of particles with short-range attraction," *Nature*, vol. 453, no. 7194, pp. 499–503, 2008.

[86] M. Karttunen, A. Lukkarinen, and I. Vattulainen, *Novel Methods In Soft Matter Simulations*. 2004.

[87] S. M. Allen, "Ground state structures in ordered binary neighbor interactions*," *Acta Metall.*, vol. 20, no. 1, p. 423, 1972.

[88] D. C. Queller and K. F. Goodnight, "Estimation of genetic relatedness using allozyme data," *Evolution (N. Y).*, vol. 43, pp. 258–275, 1989.

[89] N. J. Buttery *et al.*, "Structured growth and genetic drift raise relatedness in the social amoeba Dictyostelium discoideum," *Biol. Lett.*, vol. 8, no. 5, pp. 794–797, 2012.

[90] B. J. Heinrich, S. O. Neill, and N. Goldman, "Cutting through the complexity of compliance," *Proc. R. Soc. Lond. B Biol. Sci.*, vol. 280, p. 20122770, 2013.

[91] A. S. Griffin, S. A. West, and A. Buckling, "Cooperation and competition in pathogenic bacteria; Casamino Acid (CAA)," *Nature*, vol. 430, pp. 1024–1027, 2004.

[92] C. Majerczyk, E. Schneider, and E. P. Greenberg, "Quorum sensing control of Type

VI secretion factors restricts the proliferation of quorum-sensing mutants," *Elife*, vol. 5, p. e14712, 2016.

[93] H. Celiker and J. Gore, "Cellular cooperation: Insights from microbes," *Trends Cell Biol.*, vol. 23, no. 1, pp. 9–15, 2013.

[94] W. W. Driscoll and J. W. Pepper, "Theory for the evolution of diffusible external goods," *Evolution (N. Y).*, vol. 64, no. 9, pp. 2682–2687, 2010.

[95] S. Borgeaud, L. C. Metzger, T. Scrignari, and M. Blokesch, "The type VI secretion system of Vibrio cholerae fosters horizontal gene transfer," *Science (80-.).*, vol. 347, no. 6217, pp. 63–67, 2015.

[96] T. Nogueira, D. J. Rankin, and M. Touchon, "Article Horizontal Gene Transfer of the Secretome Drives the Evolution of Bacterial Cooperation and Virulence," *Cu*, vol. 19, no. 20, pp. 1683–1691, 2009.

[97] Q.-X. Liu *et al.*, "Phase separation explains a new class of self-organized spatial patterns in ecological systems," *Proc. Natl. Acad. Sci.*, vol. 110, no. 29, pp. 11905–11910, 2013.

[98] Q. X. Liu, M. Rietkerk, P. M. J. Herman, T. Piersma, J. M. Fryxell, and J. van de Koppel, "Phase separation driven by density-dependent movement: A novel mechanism for ecological patterns," *Phys. Life Rev.*, vol. 19, pp. 107–121, 2016.

[99] A. M. Turing, "The chemical basis of morphogenesis," *Philos. Trans. R. Soc. Lond. B Bio. Sci.*, vol. 237, pp. 37–72, 1952.

[100] S. Kondo and T. Miura, “Reaction-diffusion model as a framework for understanding biological pattern formation,” *Science (80-.).*, vol. 329, no. 5999, pp. 1616–1620, 2010.

[101] J. W. Cahn and J. E. Hilliard, “ Free Energy of a Nonuniform System. I. Interfacial Free Energy and Free Energy of a Nonuniform System. III. Nucleation in a Two-Component Incompressible Fluid ,” *Sel. Work. John W. Cahn*, vol. 28, pp. 25–28, 2013.

[102] Y. Fily and M. C. Marchetti, “Athermal phase separation of self-propelled particles with no alignment,” *Phys. Rev. Lett.*, vol. 108, no. 23, p. 235702, 2012.

[103] H. P. Bais, R. Vepachedu, S. Gilroy, R. M. Callaway, and J. M. Vivanco, “Allelopathy and Exotic Plant Invasion: From Molecules and,” *Science (80-.).*, vol. 1377, no. 2003, pp. 1377–1380, 2008.

[104] J. B. C. Jackson and L. Buss, “Alleopathy and spatial competition among coral reef invertebrates,” *Proc. Natl. Acad. Sci.*, vol. 72, no. 12, pp. 5160–5163, 2006.

[105] M. E. Cates, D. Marenduzzo, I. Pagonabarraga, and J. Tailleur, “Arrested phase separation in reproducing bacteria creates a generic route to pattern formation,” *Proc. Natl. Acad. Sci.*, vol. 107, no. 26, pp. 11715–11720, 2010.

[106] S. Henkes, Y. Fily, and M. C. Marchetti, “Active jamming: Self-propelled soft particles at high density,” *Phys. Rev. E - Stat. Nonlinear, Soft Matter Phys.*, vol. 84, no. 4, p. 40301, 2011.

[107] F. Kümmel, T. Speck, J. Bialké, C. Bechinger, H. Löwen, and I. Buttinoni, "Dynamical Clustering and Phase Separation in Suspensions of Self-Propelled Colloidal Particles," *Phys. Rev. Lett.*, vol. 110, no. 23, pp. 1–5, 2013.

[108] V. Narayan, S. Ramaswamy, and N. Menon, "Long-lived Giant Number Fluctuations in a Swarming Granular Nematic Supporting Online Material -- Supplemental Material," *Science (80-.).*, vol. 317, no. 5834, pp. 105–8, 2007.

[109] T. Sanchez, D. T. N. Chen, S. J. Decamp, M. Heymann, and Z. Dogic, "Spontaneous motion in hierarchically assembled active matter," *Nature*, vol. 491, no. 7424, pp. 431–434, 2012.

[110] T. Sanchez, "Cilia-Like Beating of Active," *Science (80-.).*, vol. 456, no. 2011, pp. 456–459, 2013.

[111] F. Boyer, G. Fichant, J. Berthod, Y. Vandenbrouck, and I. Attree, "Dissecting the bacterial type VI secretion system by a genome wide in silico analysis: What can be learned from available microbial genomic resources?," *BMC Genomics*, vol. 10, p. 104, 2009.

[112] C. D. Nadell and B. L. Bassler, "A fitness trade-off between local competition and dispersal in Vibrio cholerae biofilms," *Proc. Natl. Acad. Sci.*, vol. 108, no. 34, pp. 14181–14185, 2011.

[113] K. Skorupski and R. K. Taylor, "Positive selection vectors for allelic exchange," *Gene*, vol. 169, no. 1, pp. 47–52, 1996.

[114] R. A. Edwards, L. H. Keller, and D. M. Schifferli, “Improved allelic exchange vectors and their use to analyze 987P fimbria gene expression,” *Gene*, vol. 207, no. 2, pp. 149–157, 1998.

[115] J. Li *et al.*, “SecReT6: A web-based resource for type VI secretion systems found in bacteria,” *Environ. Microbiol.*, vol. 17, no. 7, pp. 2196–2202, 2015.

[116] M. A. Peabody, M. R. Laird, C. Vlasschaert, R. Lo, and F. S. L. Brinkman, “PSORTdb: Expanding the bacteria and archaea protein subcellular localization database to better reflect diversity in cell envelope structures,” *Nucleic Acids Res.*, vol. 44, no. D1, pp. D663–D668, 2016.

[117] D. Wilson, “SUPERFAMILY—sophisticated comparative genomics, data mining, visualization and phylogeny,” *Nucleic Acids Res.*, vol. 37, pp. D380–D386, 2009.

[118] E. Paradis and J. Claude, “APE: analyses of phylogenetics and evolution in R language. R package version 3.0-11,” *Bioinformatics*, vol. 20, pp. 289–290, 2004.

[119] J. D. Hadfield, “ MCMC Methods for Multi-Response Generalized Linear Mixed Models: The MCMCglmm R Package ,” *J. Stat. Softw.*, vol. 33, no. 2, pp. 1–22, 2015.

[120] A. Gelman and D. B. Rubin, “Inference from Iterative Simulation Using Multiple Sequences,” *Stat. Sci.*, vol. 7, no. 4, pp. 457–472, 2007.

[121] M. Plummer, N. Best, K. Cowles, and K. Vines, “CODA: Convergence Diagnosis and Output Analysis for MCMC,” *R News*, vol. 6, no. 1, pp. 7-- 11, 2006.

[122] S. Nakagawa, “A general and simple method for obtaining,” *Methods Ecol. Evol*, vol. 4, no. 2, pp. 133–142, 2013.

[123] M. E. J. Newman and G. T. Barkema, *Monte Carlo Methods in Statistical Physics*. Oxford University Press, 1999.

[124] A. Tiribocchi, R. Wittkowski, D. Marenduzzo, and M. E. Cates, “Active Model H: Scalar Active Matter in a Momentum-Conserving Fluid,” *Phys. Rev. Lett.*, vol. 115, no. 18, p. 18, Oct. 2015.

[125] C. A. Weber, C. Bock, and E. Frey, “Supplemental Material : Defect-Mediated Phase Transitions in Active Soft Matter,” *Phys. Rev. Lett.*, vol. 1, pp. 1–7, Apr. 2014.

[126] C. Peng, T. Turiv, Y. Guo, Q. H. Wei, and O. D. Lavrentovich, “Command of active matter by topological defects and patterns,” *Science (80-.).*, vol. 354, no. 6314, pp. 882–885, 2016.

[127] J. L. Silverberg, M. Bierbaum, J. P. Sethna, and I. Cohen, “Collective Motion of Moshers at Heavy Metal Concerts,” *Phys. Rev. Lett.*, vol. 110, p. 22, May 2013.

[128] M. E. Cates and J. Tailleur, “Motility-induced phase separation,” *Annu. Rev*, vol. 6, no. 1, pp. 219–244, 2015.

[129] C. A. Rodesney *et al.*, “Correction for Rodesney et al., Mechanosensing of shear by Pseudomonas aeruginosa leads to increased levels of the cyclic-di-GMP signal initiating biofilm development.,” *Proc. Natl. Acad. Sci. U. S. A.*, vol. 114, no. 28, p. E5760, Jun. 2017.

[130] M. S. and D. J.F., “Microbial biofilms in the human gastrointestinal tract,” *J. Appl. Microbiol.*, vol. 102, no. 5, pp. 1187–1196, Feb. 2007.

[131] T. F. C. Mah and G. A. O’Toole, “Mechanisms of biofilm resistance to antimicrobial agents,” *Trends Microbiol.*, vol. 9, no. 34, 2001.

[132] C. J.W., M. L., and A. C.R., “Biofilm in implant infections: Its production and regulation,” *Int. J. Artif. Organs*, vol. 28, no. 11, pp. 1062–1068, 2005.

[133] M. Ledin, “The environmental impact of mine wastes -- Roles of microorganisms and their significance in treatment of mine wastes,” *Earth-Science Rev.*, vol. 41, no. 1–2, pp. 67–108, Oct. 2002.

[134] C. Säwström, P. Mumford, W. Marshall, A. Hodson, and J. Laybourn-Parry, “The microbial communities and primary productivity of cryoconite holes in an Arctic glacier (Svalbard 79 N),” *Polar Biol.*, vol. 25, no. 8, pp. 591–596, Aug. 2002.

[135] C. Matz, D. McDougald, A. M. Moreno, P. Y. Yung, F. H. Yildiz, and S. Kjelleberg, “Biofilm formation and phenotypic variation enhance predation-driven persistence of Vibrio cholerae,” *Proc. Natl. Acad. Sci.*, vol. 102, no. 46, pp. 16819–16824, Nov. 2005.

[136] A. Persat *et al.*, “Leading Edge The Mechanical World of Bacteria,” *Cell*, vol. 161, no. 5, pp. 988–997, May 2015.

[137] G. W. Jones and S. J. Chapman, “Modeling Growth in Biological Materials,” *SIAM Rev.*, vol. 54, no. 1, pp. 52–118, Nov. 2012.

[138] J. U. Kreft, C. Picioreanu, J. W. T. Wimpenny, and M. C. M. Van Loosdrecht, "Individual-based modelling of biofilms," *Microbiology*, vol. 147, no. 11, pp. 2897–2912, 2001.

[139] M. Delarue *et al.*, "Mechanical control of cell flow in multicellular spheroids," *Phys. Rev. Lett.*, vol. 110, no. 13, p. 13810, Mar. 2013.

[140] X. Zhang, X. Wang, K. Nie, M. Li, and Q. Sun, "Simulation of Bacillus subtilis biofilm growth on agar plate by diffusion-reaction based continuum model," *Phys. Biol.*, vol. 13, no. 4, p. 18, Jul. 2016.

[141] M. J. Dorie, R. F. Kallman, and M. A. Coyne, "Effect of cytochalasin B, nocodazole and irradiation on migration and internalization of cells and microspheres in tumor cell spheroids," *Exp. Cell Res.*, vol. 166, no. 2, pp. 370–378, Sep. 1986.

[142] M. J. Dorie, R. F. Kallman, V. A. Repacchietta, and Y. R. Huang, "Migration and internalization of cells and polystyrene microspheres in tumor cell spheroids," *Exp. Cell Res.*, vol. 141, no. 201, 1982.

[143] E. Hernández-Lemus, "Nonequilibrium Thermodynamics of Cell Signaling," *J. Thermodyn.*, vol. 2012, pp. 1–10, Jun. 2012.

[144] N. Fakhri *et al.*, "High-resolution mapping of intracellular fluctuations using carbon nanotubes," *Science (80-.).*, vol. 344, no. 6187, pp. 1031–1035, May 2014.

[145] R. Adams, S. Koehler, S. Sciences, L. Angeles, L. Alamos, and L. Alamos, "Broken detailed balance at mesoscopic scales in active biological systems," *Science (80-.).*,

vol. 352, no. 6285, pp. 1–4, Apr. 2016.

[146] L. M. Chen and L. H. Chai, "A theoretical analysis on self-organized formation of microbial biofilms," *Phys. A Stat. Mech. its Appl.*, vol. 370, no. 2, pp. 793–807, 2006.

[147] G. M. Suel *et al.*, "Metabolic co-dependence gives rise to collective oscillations within biofilms.," *Nature*, vol. 523, no. 7562, pp. 550–554, 2015.

[148] C. Douarche, J. M. Allain, and E. Raspaud, "Bacillus subtilis Bacteria Generate an Internal Mechanical Force within a Biofilm," *Biophys. J.*, vol. 109, no. 10, pp. 2195–2202, 2015.

[149] C. Picioreanu, M. C. M. Van Loosdrecht, and J. J. Heijnen, "Two-dimensional model of biofilm detachment caused by internal stress from liquid flow," *Biotechnol. Bioeng.*, vol. 72, no. 2, 2001.

[150] C. B. Volle, M. A. Ferguson, K. E. Aidala, E. M. Spain, and M. E. Nunez, "Spring constants and adhesive properties of native bacterial biofilm cells measured by atomic force microscopy," *Colloids Surfaces B Biointerfaces*, 2008.

[151] J. K. Teschler *et al.*, "Living in the matrix: assembly and control of Vibrio cholerae biofilms," *Nat. Rev. Microbiol.*, vol. 13, p. 255, 2015.

[152] J. Yan, C. D. Nadell, H. A. Stone, N. S. Wingreen, and B. L. Bassler, "Extracellular-matrix-mediated osmotic pressure drives Vibrio cholerae biofilm expansion and cheater exclusion," *Nat Commun*, vol. 8, p. 327, 2017.

[153] A. Birjiniuk, N. Billings, E. Nance, J. Hanes, K. Ribbeck, and P. S. Doyle, "Single particle tracking reveals spatial and dynamic organization of the Escherichia coli biofilm matrix," 2014.

[154] A. Seminara *et al.*, "Osmotic spreading of Bacillus subtilis biofilms driven by an extracellular matrix," *Proc. Natl. Acad. Sci.*, vol. 109, no. 4, pp. 1116–1121, 2012.

[155] J. T. Pentz, P. Márquez-Zacarías, P. J. Yunker, E. Libby, and W. C. Ratcliff, "Ecological advantages and evolutionary limitations of aggregative multicellular development," *bioRxiv*, vol. 10, p. 255307, 2019.

[156] B. K. Hammer and B. L. Bassler, "Quorum sensing controls biofilm formation in Vibrio cholerae," *Mol. Microbiol.*, vol. 51, p. 1521, 2004.

[157] H. Boudarel, J. D. Mathias, B. Blaysat, and M. Grédiac, "Towards standardized mechanical characterization of microbial biofilms: analysis and critical review," *npj Biofilms Microbiomes*, vol. 4, no. 1, p. 17, 2018.

[158] M. P. Vigers and J. N. Wilking, "Characterizing Biofilm Extracellular Matrices with Mechanical Measurement Techniques," *Biophys. J.*, vol. 110, no. 3, p. 172a, 2016.

[159] C. Falcón García *et al.*, "Topographical alterations render bacterial biofilms susceptible to chemical and mechanical stress," *Biomater. Sci.*, vol. 7, no. 1, pp. 220–232, 2019.

[160] J. J. Williamson and G. Salbreux, "Stability and Roughness of Interfaces in Mechanically Regulated Tissues," *Phys. Rev. Lett.*, vol. 121, no. 23, p. 238102,

2018.

[161] D. A. Weitz and T. G. Mason, “Optical Measurements of Frequency Dependent Linear Viscoelastic Moduli of Complex Fluids,” *Phys. Rev. Lett.*, vol. 74, no. 7, pp. 1250–1253, 1995.

[162] L. García-Bayona and L. E. Comstock, “Bacterial antagonism in host-associated microbial communities,” *Science (80-.).*, vol. 361, no. 6408, p. eaat2456, 2018.

[163] T. A. Witten, L. Leibler, and P. A. Pincus, “Stress Relaxation in the Lamellar Copolymer Mesophase,” *Macromolecules*, vol. 23, no. 3, pp. 824–829, 1990.

[164] P. Taylor and D. G. Allison, “The Biofilm Matrix,” *October*, vol. 8, no. November 2011, pp. 37–41, Sep. 2010.

[165] G. A. Pankey and L. D. Sabath, “Clinical Relevance of Bacteriostatic versus Bactericidal Mechanisms of Action in the Treatment of Gram-Positive Bacterial Infections,” *Clin. Infect. Dis.*, vol. 38, no. 6, pp. 864–870, 2004.

[166] M. E. Falagas, G. C. Makris, G. Dimopoulos, and D. K. Matthaiou, “Heteroresistance: a concern of increasing clinical significance?,” *Clin. Microbiol. Infect.*, vol. 14, no. 2, pp. 101–104, 2008.

[167] V. I. Band and D. S. Weiss, “Mechanisms of Antimicrobial Peptide Resistance in Gram-Negative Bacteria,” *Antibiotics*, vol. 4, no. 1, pp. 18–41, 2015.

[168] V. I. Band *et al.*, “Antibiotic failure mediated by a resistant subpopulation in Enterobacter cloacae,” *Nat. Microbiol.*, vol. 1, p. 16053, May 2016.